HEINRICH HEINE
UNIVERSITÄT DÜSSELDORF

Classical electron magnetotransport in controlled potential landscapes

Inaugural-Dissertation

zur Erlangung des Doktorgrades der
Mathematisch-Naturwissenschaftlichen Fakultät der
Heinrich-Heine-Universität Düsseldorf

vorgelegt von

Jakob Schluck

geboren am 4. Mai 1988 in Leverkusen

Düsseldorf, März 2018

aus dem Institut für Experimentelle Physik der kondensierten Materie
der Heinrich-Heine-Universität Düsseldorf

Gedruckt mit der Genehmigung der
Mathematisch-Naturwissenschaftlichen Fakultät der
Heinrich-Heine-Universität Düsseldorf

Berichterstatter

1. Prof. Dr. Thomas HEINZEL

2. Prof. Dr. Jürgen HORBACH

3. Prof. Dr. Klaus ENSSLIN

Tag der mündlichen Prüfung: 14. Juni 2018

Zusammenfassung

Diese Arbeit beschäftigt sich mit klassischem zweidimensionalem Elektronentransport in künstlichen Potentiallandschaften. Ausgangsmaterial ist das hochbewegliche zweidimensionale Elektronengas in modulationsdotierten GaAs/Al$_x$Ga$_{1-x}$As Heterostrukturen.

Zunächst wurden sogenannte magnetische Barrieren untersucht. Hierbei handelt es sich um auf einer sub-Mikrometerskala lokalisierte Magnetfelder, die durch ferromagnetische Schichten erzeugt werden können. Wir konnten zeigen, dass eine Vermessung der Magnetisierung der Schicht mittels Hall-Magnetometrie durch einen ballistischen Effekt erschwert wird. Mit Hilfe von numerischen Simulationen konnte das korrekte Magnetisierungsverhalten bestimmt werden.

Durch das Hinzufügen eines homogenen Hintergrundmagnetfeldes, das dem Barrierenfeld entgegengesetzt ist, konnten wir experimentell Widerstandsoszillationen nachweisen. Quantenmechanische Computersimulationen wiesen deren Ursprung in kommensurablen Schlangenbahnen nach.

Der zweite Teil der Arbeit beschäftigt sich mit Aspekten des Elektronentransports in lateralen Übergittern. So nennt man periodische Modulationen des elektrostatischen oder magnetischen Potentials. Wir untersuchten so genannte Antidotgitter, eine zweidimensionale Anordnung von kreisförmigen Verarmungszonen, in einem Regime, in dem Quantenoszillationen den klassischen Kommensurabilitäten überlagert sind. Wir beobachteten erstmalig die Koexistenz von Quantensignaturen sowohl des Band- als auch des Hüpftransports in der selben Resistivitätskomponente.

Weiterhin wurde ein neuartiges magneto-elektrisches Hybridgitter, bestehend aus einem quadratischen Antidotgitter kombiniert mit einem eindimensionalem magnetischen Übergitter bestehend aus magnetischen Barrieren wechselnden Vorzeichens, untersucht. Durch Variieren der Magnetisierung fanden wir Widerstandsoszillationen, deren Minima an das Auftreten klassischer Schlangenbahnen koppeln, die mit dem Antidotgitter kommensurabel sind.

Im letzten Teil der Arbeit werden sogennante klassische Lorentzgase betrachtet. Dieses Modell beschreibt die Streuung von Elektronen in Festkörpern auf Basis zufällig verteilter kurzreichweitiger Streuer. Auf Grund der hohen Beweglichkeiten unserer Heterostruktur, konnten wir solche Streuer im klassischen Regime künstlich in das Material einbringen und deren Auswirkungen studieren. Wir konnten erstmals eindeutig die Existenz eines Maximums in der Magnetoleitfähigkeit nachweisen und dessen Ursprung diskutieren. Weiterhin beschäftigten wir uns mit der Abhängigkeit des Magnetowiderstands von der Form der Streuer im Bereich kleiner Felder.

Abstract

This thesis deals with classical two-dimensional electron transport in artificial potential landscapes. The starting point is the two-dimensional electron gas in modulation doped high-mobility GaAs/Al$_x$Ga$_{1-x}$As heterostructures.

First we studied magnetic fields localized on a sub-micron scale, so-called magnetic barriers. We could demonstrate how a measurement of the magnetization via conventional Hall magnetometry of such a structure can be hampered by a ballistic effect. With the help of numerical simulations, the correct magnetization trace could be recovered.

By adding a homogeneous background magnetic field with anti-parallel orientation to the barrier, we could experimentally observe resistance oscillations. Their origin is traced back to commensurate snake trajectories by quantum mechanical simulations.

The second part of the thesis treats aspects of electron transport in periodically modulated potentials, so-called lateral superlattices. We studied antidot lattices, two-dimensional arrangements of circular depletion zones, in a regime where quantum oscillations are superimposed to the classical commensurabilities. For the first time, we find the coexistence of quantum signatures of band- and hopping transport in the same resistivity component.

Furthermore, a novel magneto-electric hybrid lattice, a combination of a square antidot lattice with a one-dimensional magnetic superlattice comprised of magnetic barriers with alternating direction, was studied. By tuning the magnetization, we find resistance oscillations, whose minima are linked to the existence of classical snake trajectories that are commensurate with the antidot lattice.

In the last part we consider so-called classical Lorentzgases. This model describes the scattering of electrons in solids on the basis of randomly placed short-ranged scatterers. Due to the high mobility of our heterostructure, we could artificially introduce such scatterers in the classical regime into the material and study their effect on transport. For the first time we could unambiguously demonstrate the existence of a maximum in magnetoconductivity and discuss its origin. Finally we deal with the dependence of the magnetoresistivity on the shape of the scatterers for the regime of low magnetic fields.

Contents

Introduction

An ever increasing understanding of electronic transport in solids is at the heart of the tremendous change brought upon us by the digital revolution. Without knowledge of the properties of electrons in semiconductors, Bardeen and Brattain [1] could not have designed the first functional transistor in 1948. From that point on, huge technological progress has been made, leading to the ongoing miniaturization of electronics affecting our everyday life so profoundly.

Also from the viewpoint of a fundamental scientist, important breakthroughs were achieved. The integer- and the fractional quantum Hall effect [2, 3] and the conductance quantization in one-dimensional channels [4, 5] were discovered, while Coulomb blockade oscillations demonstrated the possibility of transport through tailored zero-dimensional systems [6, 7], to name just a few of the most prominent developments. Many more are covered in dedicated textbooks, see e.g. Refs. [8–10]. Although in recent years a lot of attention has been paid to novel material types like graphene [11, 12] or topological insulators [13–16], the two-dimensional electron gas formed at the interface between gallium arsenide and aluminum gallium arsenide still offers rich research opportunities. The huge mobilities and corresponding mean free paths routinely reached within this material system [17], make it an ideal candidate to study the scattering of electrons in a controlled environment. It allows us to operate in a regime, where the extension of artificially introduced scattering potentials is large compared to the Fermi wavelength of the electrons, but small compared to their mean free path. This is the so called classical ballistic regime. With this at hand, we can test fundamental transport theories in a controlled way. A magnetic field applied perpendicular to the plane of the electron gas is an invaluable tool for doing so. In classical terms, it leads to a deformation of electron trajectories into circles with a cyclotron radius inversely proportional to the magnetic field strength. This tunes the electron's sensitivity to the exact details of the potential landscape and allows for its characterization. For instance, in disordered systems, a negative magnetoresistance is predicted for the case of randomly placed short range scatterers [18], whereas it should be positive for correlated soft potentials [19]. In the case of mixed disorder, the outcome depends sensitively on the respective potential strengths [20, 21]. These theoretical predictions are always made under limiting assumptions and it is therefore of high fundamental interest, to experimentally verify their range of validity.

Regular arrangements of scattering centers have also attracted a lot of attention since their first realizations [22–31]. Here, the electron cyclotron radius and the lattice constant of the scattering centers can become *commensurate*, leading to periodic resistance oscillations. These systems have mostly been used to test, which

aspects of electronic transport can be understood in classical terms and at what point, a quantum mechanical description becomes necessary.

Not only the case of homogeneous magnetic fields, but also strongly localized ones have been considered. The simplest one is probably the magnetic barrier [32–36], which is highly localized in one direction, but translationally invariant in the other. Depending on the strength of the field, electrons may be able to pass the barrier or will get reflected. It can be utilized as a building block for more complex structures [37–40], where, of course, the effect of a single barrier needs to be well-understood.

This thesis is devoted to a study of magnetotransport of all three aforementioned cases, namely single magnetic barriers and ordered as well as disordered systems. The availability of high-mobility heterostructures enables us to explore the so-called classical ballistic regime in artificially created potential landscapes. Here, we can test the validity of a description of electronic transport in terms of trajectories under controlled conditions. The thesis is structured as follows.

In chapter 1, the fundamental concepts necessary for an understanding of advanced studies are introduced. First, we discuss the formation of a two-dimensional electron gas in a semiconductor heterostructure, which lies at the foundation of all experiments in this thesis. We argue how the high mobilities are obtained and what limits them in state of the art heterostructures. Next we give a brief introduction to the semiconductor processing technologies, which are used within the course of sample preparation. In section 1.3 a brief overview on the main results of the Drude-Boltzmann theory for electronic transport in magnetic fields is given. The effect of Landau quantization and the resulting quantum Hall effect as well as the Shubnikov-de Haas oscillations are also introduced. The experimental setup, including the cryogenics as well as the electronics, is described in section 1.4. Finally, the numerical schemes employed for the planning of the experiments as well as their interpretation are presented in section 1.5.

The second chapter consists of a detailed introduction to the state of research concerning the topics covered in this thesis.

We begin with a discussion of the effect of the highly localized magnetic field profiles called magnetic barriers. Their experimental realization is presented and the current state of the literature is reviewed. These preparations lead over to the first two papers in chapter 3, where we first demonstrate how a ballistic effect impedes Hall magnetometry of a magnetic barrier structure and show how it can be overcome with the help of classical simulations. Secondly, we study the influence of a homogeneous background magnetic field on the transmission properties of a magnetic barrier. The experimentally observed resistance oscillations are interpreted as caused by commensurate snake trajectories with the help of quantum simulations.

In section 2.2, the topic of lateral superlattices is introduced. A superlattice denotes a regular modulation of the potential landscape, be it via electric or magnetic fields. One-dimensional as well as two-dimensional superlattices are discussed. Emphasis is put on the nature of transport within these structures, which is

usually classified as being classical, semi-classical or purely quantum mechanical. Lateral superlattices are an ideal playground to test the validity of the related transport models. Within this thesis, we studied magnetotransport in a so-called antidot lattice, a two-dimensional regular pattern of depletion zones, and found quantum signatures of different transport mechanisms that could be related to classical trajectories. In a secondary paper, we combined an antidot lattice with a regular arrangement of magnetic barrier structures. We found classical resistance oscillations coinciding with the appearance of classical snake trajectories. These results are summarized in papers three and four in chapter 3.

Finally, section 2.3 deals with the transport properties of classical Lorentz gases. In such systems, static hard-wall obstacles are placed randomly within the plane and function as the only source of scattering for the electronic movement. The related phase diagram is discussed and theoretical as well as experimental studies are reviewed. Within this thesis, two papers comprising Lorentz gas systems were published, which can be found as the final two papers in chapter 3. In the first, we experimentally observe a numerically predicted [41] maximum in the magnetoconductivity of dense Lorentz gases. An explanation is given in terms of a qualitative change of the nature of electronic transport. Secondly, we studied the influence of the shape of the obstacles on the low-field magnetoresistance. Previously, mostly circular obstacles were considered and to the best of our knowledge we were the first to produce disordered arrays of scatterers of square and retroreflective shape.

The thesis ends with some conclusive remarks towards potential future research opportunities in chapter 4.

1 Fundamental concepts

1.1 The two-dimensional electron gas in GaAs/Al$_x$Ga$_{1-x}$As

The two-dimensional electron gas (2DEG) formed at the interface between the two III-V semiconductors GaAs and Al$_x$Ga$_{1-x}$As is the foundation of all experiments discussed in this thesis. To generate such heterostructures, the technology of molecular beam epitaxy is used [42, 43]. Materials are slowly deposited upon a heated substrate by evaporating them in an ultra-high vacuum chamber. When done correctly, atomically sharp layers can be grown. In the following, we will briefly discuss the physics leading to 2DEG formation as well as its merits in comparison to similar systems. A review of the early developments of the electronic properties of two-dimensional systems is given in Ref. [44]. For more details on the recent state of the art of 2DEG formation, the reader is referred to Refs. [45, 46] and references therein.

The band gap E_b of GaAs lies completely within the band gap of Al$_x$Ga$_{1-x}$As, as is visualized in Fig. 1.1a). Tuning the parameter x allows one to vary the gap in Al$_x$Ga$_{1-x}$As ranging from the value for pure GaAs ($x = 0$), $E_b = 1.42$ eV to the one for pure AlAs ($x = 1$), where $E_b = 2.16$ eV [47]. When the two semiconductors are grown upon each other, and n-dopants are placed within the Al$_x$Ga$_{1-x}$As, the Fermi level will equilibrate along the crystal. This results in a rearrangement of the doping-electrons, where they can reduce their energy by occupying the states in the conduction band of the GaAs. When this process is treated in a self-consistent way, one can find parameters for the doping density, where the bottom of the conduction band lies below the Fermi energy only in a very small interval near the interface of the two semiconductors. This can be engineered to be of a size, which is comparable to the Fermi-wavelength of the electrons. In this case, size quantization sets in in the direction of growth. The resulting situation is schematically shown in Fig. 1.1b). Typically, the level spacing is of the order of $\Delta E \approx 10$ meV. If one wants to create a true 2DEG, only the lowermost state in this direction with energy E_0 must be occupied. Therefore, all experiments on 2DEGs in this thesis were performed at cryogenic temperatures (see chapter 1.4), where the thermal energy is well below the level spacing. In a real structure, an additional capping layer of GaAs is grown on top again, to prevent oxidation of the aluminum.

The movement of the electrons is tightly confined in one direction, while it is well described by the Hamiltonian of a free electron gas within the effective mass
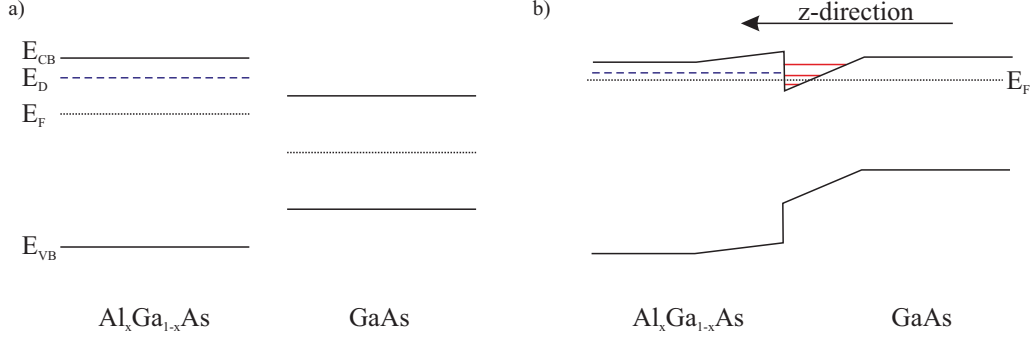
Figure 1.1: Sketch of the band structure of a GaAs/Al$_x$Ga$_{1-x}$As heterostructure.
a) shows the band diagrams of a doped Al$_x$Ga$_{1-x}$As and a GaAs semi-conductor without contact. E_{CB}, E_D, E_F, E_{VB} denote the conduction band bottom, the doping levels, the Fermi energy and the valence band top respectively. In b) the equilibrated band structure is sketched, when both materials are grown on top of each other. The space charges induce a band bending, which leads to the formation of bound states in growth-direction at the interface (red lines) lying beneath the Fermi energy.

approximation in the other two directions. One has

$$H = \frac{\hbar^2 \left(k_x^2 + k_y^2 \right)}{2m^*} + E_0, \tag{1.1}$$

where the z-direction is taken as the growth direction and $m^* = 0.067 m_e$ is the effective mass of electrons in GaAs, with m_e the electron rest mass.

For the experiments conducted within this thesis, additional potentials enter the Schroedinger equation. While electrostatic potentials are straightforward to include, for magnetostatic fields the so called Peierls substitution is used [48]. The resulting Hamiltonian then reads:

$$H = \frac{\left(\vec{p} + e\vec{A} \right)^2}{2m^*} + \phi(x, y) + E_0, \tag{1.2}$$

where ϕ is the electrostatic potential and $\vec{A}$ the magnetic vector potential. This Hamiltonian is not only valid for this specific type of heterostructure, but also for other material combinations as well as the inversion channels in silicon MOSFETs. However, the GaAs/Al$_x$Ga$_{1-x}$As heterostructure has the advantage of AlAs and GaAs having almost the same lattice constant, which leads to negligible strain at the interface [47]. This results in an increased mobility μ of the charge carriers, since scattering at lattice imperfections is reduced. A further improvement was made by inventing the technique of modulation doping [49], where an additional spacer layer, with thickness d, of undoped Al$_x$Ga$_{1-x}$As is grown on top of the

GaAs before the doped one. The resulting band rearrangement stays qualitatively unchanged, but now one has a spatial separation of the ionized donor atoms and the 2DEG. Combined with the screening present in conductive systems (see e.g. [8]), this reduces the scattering of electrons from the charged donor ions. The remaining scattering events are typically of small-angle type, but are still one of the dominant mobility limiting processes [45, 50]. The silicon atoms, conventionally used as n-type dopants, can either take the form of a shallow or a deep donor state. The deep state is called a DX center and at low temperatures is usually negatively charged, therefore trapping two electrons [45]. When briefly exposing the sample to infrared radiation, the charge is transferred to the the 2DEG and the donor is now positively charged. The number of charged impurities has not changed, but since in modern high-mobility heterostructures it holds $\mu_{CI} \propto d^3 n_e^{3/2} N_{CI}^{-1}$, where n_e is the 2DEG electron density, μ_{CI} is the mobility due to charged impurities and N_{CI} is their density, this leads to an increase in the overall mobility [45]. The spacer width d cannot be increased at will to enhance the mobility, since the electron density is inversely proportional to it. Another source of scattering are unintentionally introduced background impurities (BIs), which originate from the growth process. Since they can be found also in the plane of the 2DEG, their screening is not as efficient and also large-angle scattering is possible [50]. The mobility due to them scales as $\mu_{BI} = n_e^\delta N_{BI}$, where μ_{BI} and N_{BI} are the BI induced mobility and their density respectively. The exponent δ is of the order of one, with the exact value still under debate [45]. Other mobility limiting factors, like interface roughness and alloy scattering, only play a minor role in modern high-mobility heterostructures, where currently the BIs are the limiting factor [45]. Increasing the material purity and optimizing the growth design, modern 2DEGs in GaAs/Al$_x$Ga$_{1-x}$As heterostructures can reach electron mobilities, which are equivalent to transport mean free paths of about 300 µm [51–53].

In recent years, quite a variety of novel two-dimensional systems emerged. For example, the Dirac type fermions in graphene monolayers [11, 12, 54] or van der Waals heterostructures [55], topological insulators [13–16] or the interfaces of oxide structures [56–58]. Although these material systems all have fascinating properties and rightfully attracted tremendous interest within the last years, for experiments on basic ballistic transport properties, they are still inferior to high-mobility GaAs/Al$_x$Ga$_{1-x}$As heterostructures.

All heterostructures used within this thesis were grown by Klaus Pierz at PTB Braunschweig within the group of H.W. Schumacher. A model calculation of the band structure based on realistic assumptions [59] for the heterostructure *H012* is shown in Fig. 1.2. Here the Schrödinger-Poisson solver by Gregory Snyder [60] was used.
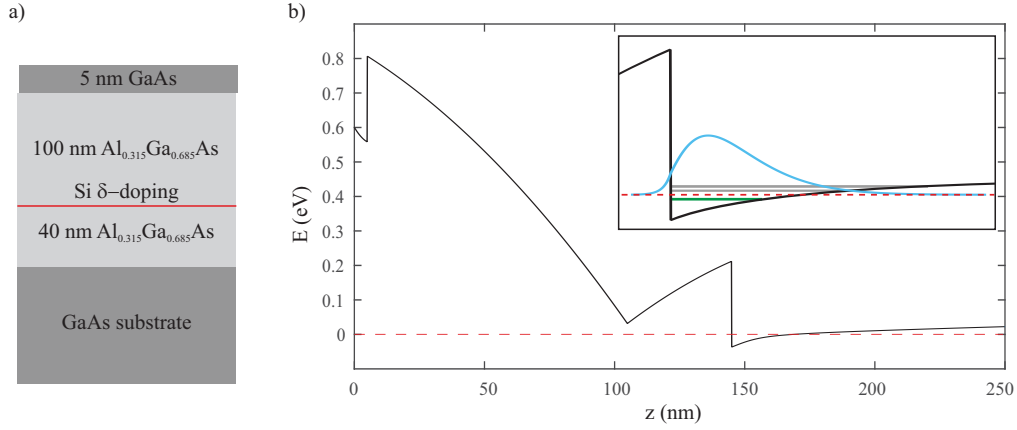
Figure 1.2: Calculated conduction band bottom in the direction of growth of heterostructure *H012*. The red dashed line indicates the Fermi energy. The inset is a zoom-in of the interface between $Al_{0.315}Ga_{0.685}As$ and GaAs. The green line is the only electron state below the Fermi level, whereas the gray lines indicate the two first states above the Fermi energy. The teal line is the square of the electron wave function in growth direction.

1.2 Semiconductor processing techniques

In this section some commonly used semiconductor processing techniques are discussed. Starting from the host material featuring a 2DEG, as introduced in the previous section, multiple patterning steps are required on the way to a working sample (cf. Fig. 1.3). We will briefly introduce the two most common lithographic techniques, which were extensively used for all the samples produced within this thesis. Furthermore, some etching and metallization schemes are presented. The techniques used here are well established in semiconductor processing and their presentation will necessarily be brief. For a more comprehensive picture of the current state of the art, the reader is referred to the specialized literature [61–63]. The exact parameters used to produce the samples we conducted experiments on within this thesis can be found in Ref [64].

1.2.1 Lithographic techniques

Once the growth of the semiconductor crystal as described in the previous section is finished, one usually wants to pattern it laterally. This is conventionally done by so called lithographic techniques. The semiconductor is covered with a thin film of a resist, which consists of a polymer in an organic solvent. Spinning the sample on a vacuum chuck at several thousand rounds per minute assures a uniform coverage. The solvent is removed by heating the sample, which leaves it with a hardened resist layer. When exposed to radiation, the polymer chains in the resist break and
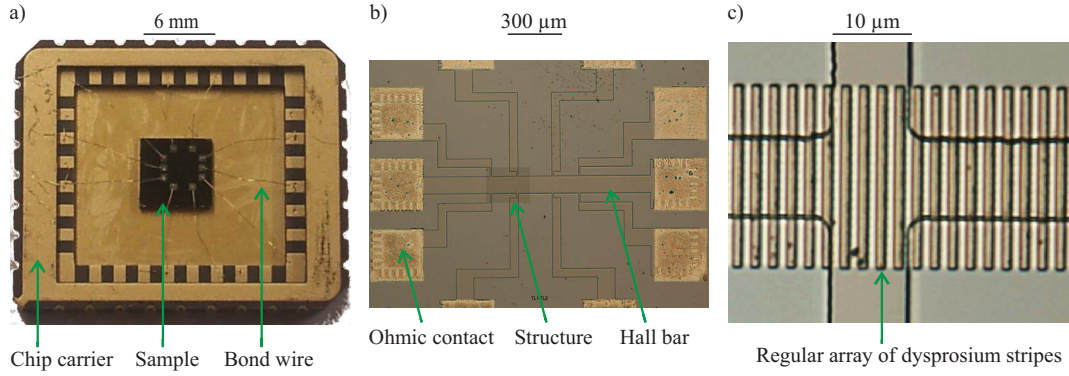
a)   6 mm   b)   300 μm   c)   10 μm

Ohmic contact   Structure   Hall bar

Regular array of dysprosium stripes

Chip carrier   Sample   Bond wire

Figure 1.3: a) Finished sample, glued to a chip carrier and wire bonded. b) Optical micrograph of a Hall bar structure. c) Optical micrograph of a single structure under study consisting of a regular array of dysprosium stripes.

are consequently more susceptible to certain solvents, which are called developers in this context. Two types of lithography were used to produce the samples under study within this thesis. The first is the so called optical lithography utilizing visible light as radiation. Since light sources with large output powers are readily available, it is possible to expose a sample as a whole to the light at once. The structural information, which one wants to transfer to the resist, is carried by a so called mask. This is a glass disk, where certain areas are made optically opaque by deposition of a chromium layer. The areas hidden behind these structures are protected from the radiation and therefore remain chemically inert to the developer. This allows for good reproducibility and high speed processing of samples, but lacks flexibility. Also the resolution is limited by the diffraction, which sets the minimal structure size d to $d \approx \lambda$, where λ is the wavelength of the light. For these reasons, optical lithography is most often used to produce coarse structures on the sample, like the Hall bar and Ohmic contacts. Schematically, the process is shown in Fig. 1.4 a)-c) as well as d)-f). In the latter case, a so called image reversal is employed. After breaking the polymer chains in the resist, the sample is heated. This induces a cross-linking of said polymer remains. Exposing the whole sample to light again, the areas featuring cross-linked polymers are now more resistant to the radiation and subsequently also the developer. The resulting edge profile of the resist remaining after developing, is advantageous for the deposition of thicker films. When one needs to transfer small patterns or a very high overlay accuracy is desired, a second lithographic technique is frequently used. In electron beam lithography (EBL), electrons take the role of the radiation. The samples are introduced to a scanning electron microscope equipped with a controllable beam. With the help of a software interface, patterns created by computer aided design systems can directly be transferred to the resist. This allows for high flexibility. Furthermore, the achievable resolution is no longer diffraction limited, since the de-Broglie wavelength of the electrons is smaller than the polymers used for the
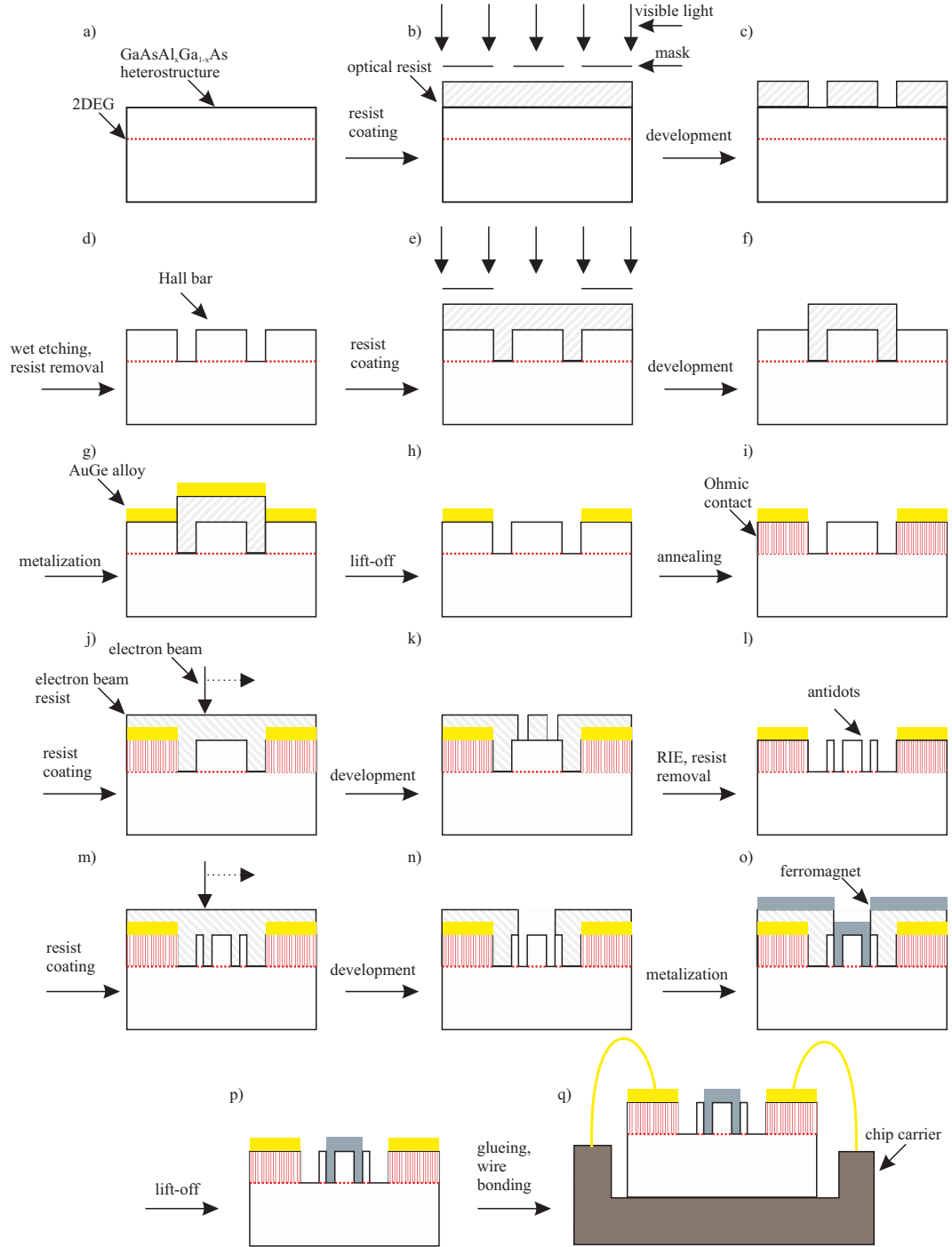
Figure 1.4: Illustration of sample processing starting from a GaAs/Al$_x$Ga$_{1-x}$As heterostructure. A Hall bar is defined via positive optical lithography and wet chemical etching. Ohmic contacts are produced by negative optical lithography followed by deposition of a AuGe layer and subsequent annealing. In the next step, antidots are introduced via electron beam lithography and reactive ion etching. A ferromagnetic film is selectively deposited on the surface by electron beam lithography and subsequent metalization. Finally the sample is glued to a chip carrier and bonded by gold wires. More detailed descriptions of each step can be found in the main text.

resist, but rather depends on the quality of the electron microscope optics. With modern systems, a resolution below 100 nm is routinely achieved. In Fig. 1.4j)-l) and m)-p), processes making use of EBL are sketched. If a high overlay accuracy is required, one makes use of so called marker structures. Mostly these are metal structures, which are placed outside of the actual area of interest on the sample. The electron microscope can then read in their positions and all following exposures are made relative to these.

1.2.2 Etching techniques

Within the context of this thesis, etching techniques were employed to deplete the 2DEG spatially selectively. In the so called mesa etching process, the Hall bar structure is defined (cf. section 1.4), while subsequent etching steps were used to induce artificial scattering centers. Based on the discussion in section 1.1, it is easy to see that a physical destruction of the semiconductor crystal up to the layer of the 2DEG leads to its depletion. Aiming for this, one usually creates a pattern within a resist using a lithographic technique. One possibility to etch away from the sample surface is to immerse it in a etching solution. The chemicals attack the semiconductor material, whereas the resist is inert to them. For the GaAs/Al_xGa_{1-x}As material under study here, one usually combines an oxidizing agent with an acid in the etching solution. The oxide forming at the surface is removed by the acid, which leads to a steady removal of material. Wet chemical etching (WCE) processes are often isotropic, leading to rather ill defined depletion zones around the edges of the resist films. When this is of critical relevance, one often prefers to rely on so called dry etching processes. Here the sample is introduced to a vacuum chamber, in which a low-density plasma is ignited. Linking the sample to the cathode leads to an acceleration of the plasma ions towards it. The etching effect can now be achieved either by the pure physical bombardment, or, by selecting a proper gas, combining it with a chemical reaction. In the latter case one speaks of reactive ion etching (RIE). This kind of process allows for a highly anisotropic etching, but the requirements are harder to meet than in WCE. Not only does one need the RIE apparatus, but also the selection of the lithographic resist is way more critical. Furthermore, the involved energies of the accelerated ions can lead to sample damage, if not handled carefully. In the sample production process, schematically shown in Fig. 1.4, WCE is used to define the Hall bar structure, while the antidots are introduced by RIE.

1.2.3 Metalization

There are many reasons, why one would want to put a metal layer on top of a semiconductor. Three of them play a role for work presented here and are therefore discussed in the following. Let us note first that a metal film put on top of a GaAs forms a Schottky barrier. The 2DEG and the metal are only capacitively coupled within a certain range of voltage applied between them. This is made use of in so

called top gate structures. Certain areas of the semiconductor are covered with a metallic layer, usually gold. By applying a voltage to this top gate with respect to the 2DEG, one has the possibility to tune the electron density externally. This is frequently used to test the density dependence of physical effects. An example can be seen in chapter 2.1. In other cases the formation of Schottky barriers is highly undesirable. To probe the properties of the 2DEG, one needs to directly contact it. This can be done by depositing materials selectively on the sample surface, which are made to diffuse into the semiconductor. They act as dopants and thus create a local Ohmic connection between the 2DEG and the sample surface, allowing for the performance of electronic measurements. In all samples under study in this thesis, an eutectic alloy of gold and germanium was used as contact material. After deposition, the sample is heated, which leads the germanium atoms to diffuse into it. Being a group IV semiconductor, they act as n-dopands in the III-V semiconductor $Al_xGa_{1-x}As$. The last use of metal structures on top of the semiconductor of relevance here, is the deposition of ferromagnetic materials. They posses a non-vanishing internal magnetization, which goes along with a corresponding local magnetic field. By tailoring the geometric properties of the ferromagnetic film, one can study the influence of inhomogeneous magnetic fields on electronic transport. This is discussed in more detail in chapter 2.1.

Since one usually does not want to cover the whole sample surface, the desired structure is first transferred to a resist pattern via a lithographic technique. The metal deposition process itself is realized by introducing the sample into a vacuum chamber and exposing it to a low pressure gas flow of the intended material. The necessary evaporation of the metal can be realized either by bombarding it with an electron beam, which is accelerated onto it via a high voltage, or by Ohmic heating by letting a current pass through it. While in principle the former is preferable, since it creates a more well defined gas flow and allows for the evaporation of materials with a higher boiling temperature, the high energy electrons can be back scattered by certain materials and create severe sample damage. This is why the ferromagnetic structures within this thesis were produced using Ohmic heating. Once the metalization is done, the remaining resist with the surplus metal parts on top are cleaned off in a so-called lift-off process. The whole procedure necessary for metalization can be found schematically in Fig. 1.4e)-i) and m)-p).

1.3 Magnetotransport

1.3.1 The Boltzmann model

The Boltzmann equation describes the phase-space evolution of a thermodynamic system due to collisions. In its full generality it is a multidimensional, non linear, integro-differential equation, which is hard to treat analytically and even numerically. Nevertheless, using suitable approximations, electron transport in solids was treated within this framework first by P. Drude [65] and later by H.A.
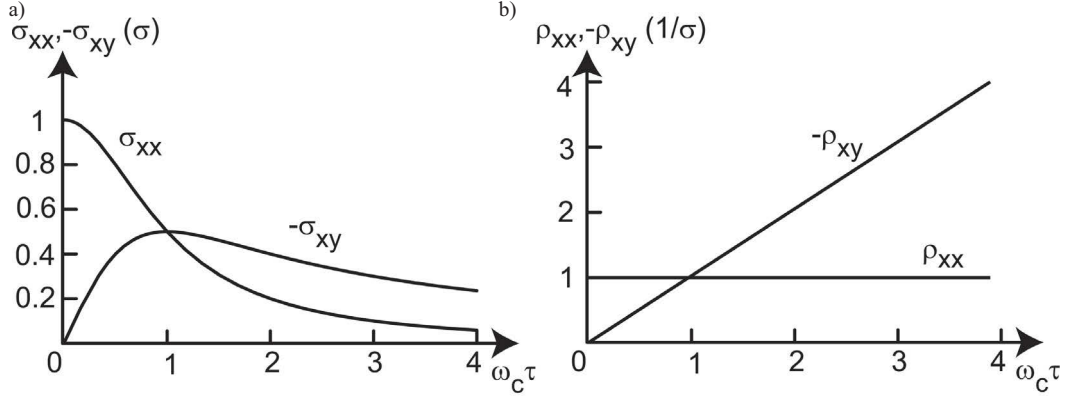
Figure 1.5: Left: Magnetic field dependence of the normalized conductivities as predicted by the simplified Boltzmann equation. Right: Resulting normalized magnetoresistivities. An explanation is given in the text. (Figure taken from [9]).

Lorentz [66]. Their results were necessarily wrong, since quantum theory was not yet formulated and they could not use the correct electron statistics to derive them. However, the concepts introduced by those for the first time made a connection between the microscopic structure of a solid and the measurable quantities of conductance and heat capacitance. Their ideas were later on refined with the concepts of quantum theory by A. Sommerfeld [67] to give the results, which we want to briefly review in this section.

A central ingredient leading to the Boltzmann equation is the so called *Stoßzahl-ansatz*, or molecular chaos, which implies the lack of correlation between particle collisions. It is the justification for describing a system of N-particles with a single particle distribution function. In later chapters we will discuss the consequences, when this assumption fails. By limiting oneself to the case of small perturbations from thermal equilibrium, one can linearize the equation, making it way more treatable. The relaxation time approximation finally summarizes all types of collisions as an effective friction force. The picture here is that, if a given system is brought out of equilibrium by, say, a small electric field, it will relax within a typical time scale τ, called the Drude scattering time. Applied to the system of a 2DEG, this means that all scattering the electrons undergo, like with phonons or impurities, is summarized within the Drude scattering time. It is connected to the mean free path ℓ_f via the electron velocity v, such that $\ell_f = v\tau$. If one further incorporates a magnetic field into the equation, the magnetoconductivity tensor $\underline{\sigma}$ can be calculated. By this tensor, the response of a system to an external electric field is quantified. It holds:

$$\vec{j} = \underline{\sigma}\vec{E}, \tag{1.3}$$

$$\underline{\sigma} = \begin{pmatrix} \sigma_{xx} & \sigma_{xy} & \sigma_{xz} \\ \sigma_{yx} & \sigma_{yy} & \sigma_{yz} \\ \sigma_{zx} & \sigma_{zy} & \sigma_{zz} \end{pmatrix}. \tag{1.4}$$

Since we are dealing with two-dimensional systems in this thesis, we can omit the entries regarding the z-direction. Furthermore we can also restrict our considerations to a magnetic field perpendicular to the plane of the 2DEG, because, to a first approximation, parallel magnetic field components will not affect it. Doing the calculation (cf. e.g. in Ref. [9]) leads to:

$$\sigma_{xx} = \sigma_{yy} = \frac{\sigma_0}{1 + \omega_c^2 \tau^2}, \tag{1.5}$$

$$\sigma_{yx} = -\sigma_{xy} = \frac{\sigma_0 \omega_c \tau}{1 + \omega_c^2 \tau^2}, \tag{1.6}$$

where $\sigma_0 = ne^2\tau/m^*$ and $\omega_c = eB/m^*$ is the cyclotron frequency, and e, m^*, n and B denote the electron charge, its effective mass, the electron density and the perpendicular magnetic field strength, respectively. Via tensor inversion, one can obtain the corresponding resistivities as

$$\rho_{xx} = \rho_{yy} = \frac{1}{\sigma_0} \tag{1.7}$$

$$\rho_{yx} = -\rho_{xy} = \frac{B}{ne}. \tag{1.8}$$

A plot can be found in Fig. 1.5. Notably, the diagonal resistivity is predicted to be independent of an applied magnetic field, although the conductivity drops monotonically. This is a result of the tensorial nature of resistivity and conductivity. The off-diagonal resistivity gives the classical Hall effect.

1.3.2 Quantizing magnetic fields

It was first noticed by L. Landau that a magnetic field applied to a free electron gas, leads to a quantization of the electron motion in the plane perpendicular to it [68], which is in turn called Landau quantization. In two-dimensional systems, one can imagine the self interference of an electron undergoing cyclotron motion to result in a discrete energy spectrum. At a given magnetic field, only certain energies correspond to cyclotron circumferences, where an integer multitude of Fermi wavelengths can be placed upon. This mechanism leads to a transition of the otherwise constant density of states (DOS) to a discrete spectrum. In ideal two-dimensional systems the DOS would consist of a series of δ-functions, while the always present disorder causes a broadening of those. The situation is depicted in Fig. 1.6a), where also the lifting of the spin degeneracy is taken into account.

In our semiclassical picture above, the quantization can only play a major role, when a significant number of electrons can complete their cyclotron motion before they experience scattering. This implies that for $\omega_c \tau > 1$ significant changes to
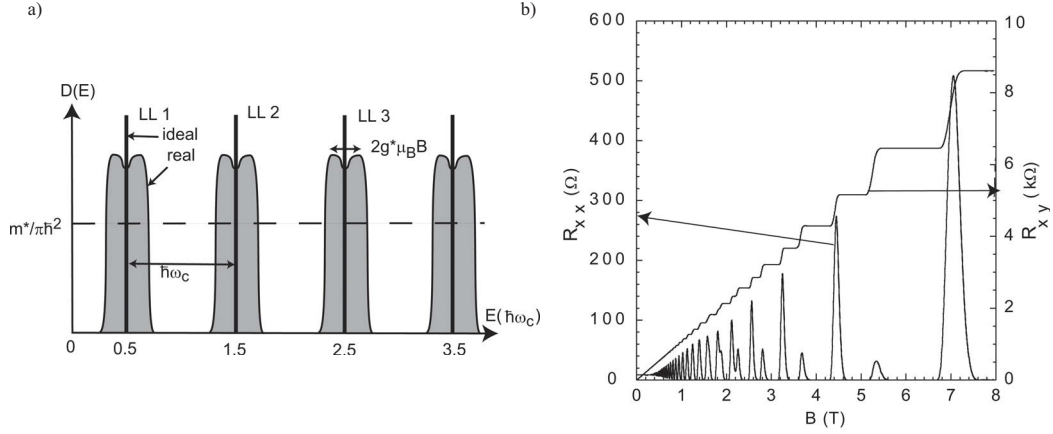
Figure 1.6: a) Change of the DOS of a 2DEG from a constant value (dashed line) to
δ-functions in an idealized system and the more realistic broader peaks.
(Taken from [9]). b) Magnetoresistance measurement of a 2DEG at
$T = 0.1\,\mathrm{K}$. For $B \geq 1\,\mathrm{T}$ well defined plateaus can be seen in the Hall
resistance, whereas Shubnikov-de Haas oscillations are visible in the
longitudinal resistance. (Taken from [9])

transport can be expected. Landau quantization profoundly affects transport in
the on- as well as the off-diagonal components of the magnetoresistivity tensor
mentioned above. In the on-diagonal elements, a vanishing DOS also leads to a
vanishing conductivity, since there are no free electron states available to carry the
current. Via tensor inversion, this also translates to a state of zero resistivity. As a
result the diagonal resistivity oscillates as a function of a perpendicular magnetic
field. This effect was first described in bismuth crystals by L. Shubnikov and
W.J. de Haas [69] and was coined in their honor as Shubnikov-de Haas oscillation
(SdH) later on. Similarly, since the electrons cannot travel freely across the sample,
they cannot equilibrate the effect of a magnetic field, leading to a constant Hall
voltage over the range of vanishing DOS. Only when the DOS is finite, the system
can relaxate and the Hall resistance jumps from one quantized value to the next
one. The effect was therefore coined the quantum Hall effect. As it turns out, the
quantization condition reads $R_H = (1/j)\,(h/e^2)$, with j integer, in the spin-resolved
case [2]. An example of a measurement of both resistivity components is shown in
Fig. 1.6. Later on, Tsui et al. used high-mobility 2DEGs in strong magnetic fields
to reveal the existence of further plateaus at certain fractions of h/e^2, which was
consequently called the fractional quantum Hall effect [3].

1.4 Experimental techniques

1.4.1 Cryogenic setup

In section 1.1 we discussed the high mobility of electrons in 2DEGs based on GaAs/Al$_x$Ga$_{1-x}$As heterostructures. We identified the origins of the high mobility within the properties of the crystal. But this is only partly true. At room temperature, electron-electron and electron-phonon scattering will inhibit reaching the mean free paths, which are necessary for ballistic experiments. For more details concerning the temperature dependence of various scattering mechanisms cf. Refs. [70–72]. Therefore, transport experiments are usually conducted at cryogenic temperatures. A machine that is used to generate and maintain such a temperature is called a cryostat. In the following we will discuss the two types of refrigerators used for the experiments in this thesis. A more thorough introduction to the field of cryogenics can be found for example in Refs. [73, 74].

For temperatures in the range of $T = 1.4 - 100\,\mathrm{K}$ a helium bath cryostat of *Oxford Instruments* is used. Liquid He^4 has a temperature of 4.2 K at atmospheric pressure. By pumping from the surface it can be further reduced. The sample chamber is connected to the helium reservoir via a needle valve, which allows control over the helium gas flow and can be used to set the temperature between 1.4 K and 4.2 K. Elevated temperatures can be obtained with the help of additional heating elements in the sample chamber. The system is furthermore equipped with a superconducting solenoid, producing magnetic fields up to 8 T.

When lower temperatures are needed, a cryo-free dilution refrigerator by *Leiden Cryogenics* pre-cooled by a pulse tube cooler is used. Here the quantum properties of the different helium isotopes He^3 and He^4 are exploited. Even at $T = 0$ the miscibility of these two isotopes remains finite, since He^3 behaves like an ideal Fermi gas in liquid He^4. The increase in the Fermi energy at some point outweighs the gain of mixing the two components. This leads to the formation of a pure He^3 and a mixed phase. By distilling He^3 atoms out of this mixture at a point remote from the phase boundary, one can create a constant flow of He^3 across it. This is thermodynamically identical to conventional evaporative cooling. The concept of the dilution refrigerator goes back to a proposal by H. London et al. [75]. Although in principle there is no lower limit for the temperature one can reach with this, the cooling power decreases with the temperature and at some point reaches an equilibrium with the inevitable heat leaks present in any real setup. The system in use here has a base temperature of 25 mK. A superconducting solenoid allows for magnetic fields up to 12 T, while a piezoelectric rotating stage can set the alignment of the sample to the magnetic field with a precision better than 0.01°.

1.4.2 Electronic measurement setup

Magnetotransport experiments are conventionally conducted electronically. One monitors the response of a system by probing, for example, the voltage drop as a
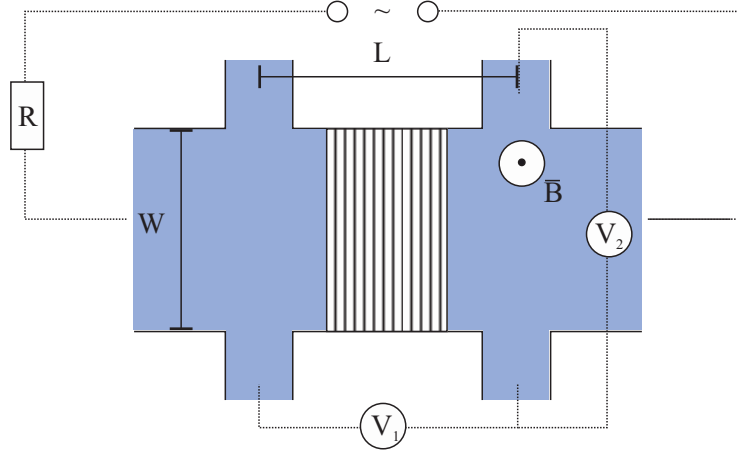
Figure 1.7: Typical Hall bar geometry used for all samples. A resistor with a resistance large compared to the sample resistance ensures a constant low frequency current, which is passed through the structure under investigation. Voltage probes are used to pick up the longitudinal as well as the Hall resistance. The effect of a magnetic field $\vec{B}$ can be studied.

reaction to an applied current. Within this thesis, all of the experiments are done in a so called four-terminal geometry. By picking up the voltage drop from contacts close to the region of experimental interest and separate from the current leads, one avoids to probe the additional contact resistances stemming, for example, from the wires and the ohmic contacts. To do so, the semiconductor is patterned via the techniques presented in section 1.2 to the shape of a Hall bar. A sketch is given in Fig. 1.7. Outside of the Hall bar, the 2DEG is depleted, which allows measurements of the longitudinal (V_1) as well as the transverse (V_2) voltage drop within the structure of interest. When a constant current I is passed through it, these quantities are directly related to the corresponding resistances and can be converted to the resistivities of this structure. It holds

$$R_{xx} = \frac{V_1}{I} = \rho_{xx}\frac{L}{W}, \tag{1.9}$$

$$R_{xy} = \frac{V_2}{I} = \rho_{xy}, \tag{1.10}$$

where L and W are the geometry factors of the Hall bar as in the sketch. The constant current is generated by attaching an ohmic resistor with a resistance R large compared to the one of the sample (typically $R = 10\,\mathrm{M\Omega}$) to the signal generator of a lock-in amplifier. The lock-in technique is also used to measure the voltage drops. The principle behind it is the frequency and phase sensitive detection of signals. The incoming signal is mixed with a reference at the detection frequency and subsequently transmitted through a low-pass filter. Noise signals with a frequency unlike the reference are thus eliminated. This reduces the noise level significantly. Furthermore it is possible to distinguish between ohmic and non-

ohmic parts of a signal via the phase information. A sine signal of a frequency of $f \approx 17\,\mathrm{Hz}$ is used, for at this low frequency, conventional theories of dc-conductivity are still valid. Also it is far away from the $50\,\mathrm{Hz}$ power line noise, but high enough for operating the lock-in amplifier at a reasonable rate.

1.5 Numerical techniques

Numerical simulations are an invaluable tool for experimental physicists. Before a sample is designed and the first experiments are done, one will often want to get an idea what to expect. Can the effect of interest be made visible using the range of realizable experimental parameters? Of course one must not confuse the results of a simulation with reality, but if, for example, we want to observe a ballistic effect and it does not show up in a classical simulation, it is unlikely to appear in experimental results and either the sample design or our understanding of the effect needs to be revised. This procedure makes it possible to reduce the number of experimental iterations, necessary for success. Since sample preparation is time consuming and prone to mistakes, this alone would justify the use of numerical simulations. But they can also support the interpretation of experimental data. For example, by looking at trajectories, in the classical case, or wave-functions, in the quantum case, one can strengthen the physical idea underlying a certain effect. Also it is possible to vary parameters, even to values outside experimental reach, demonstrating the necessary conditions for observing it or study the scaling behavior. Therefore we made frequent use of numerical simulations to obtain the results within this thesis. The techniques within reach of an experimental physicist will be presented in the following. The numerical results concerning chapter 2.3 and the related manuscripts were obtained by N. Siboni and J. Horbach using more sophisticated models from classical molecular dynamics and are beyond our discussion here.

1.5.1 Classical Kubo formalism

For the case of linear response, i.e. small perturbations, R. Kubo could derive a relation between physical quantities of a given system and the dynamics of particles within [76]. Applied to the problem of electron conductivity in a solid, this means that for small electric fields, it can be calculated from the velocity auto-correlation function.

$$\sigma_{ij} = \frac{m^* e^2}{\pi \hbar^2} \int_0^\infty \langle v_i(0) v_j(t) \rangle \exp\left(-t/\tau\right) \mathrm{d}t \qquad (1.11)$$

Here, $i, j = x, y$, while the $\langle .. \rangle$ brackets denote an ensemble averaging and the exponential function takes care of the inclusion of background scattering by weighting the calculation with the Drude scattering time τ. The procedure now consists of solving Newtons equations of motion for an ensemble of electrons, which
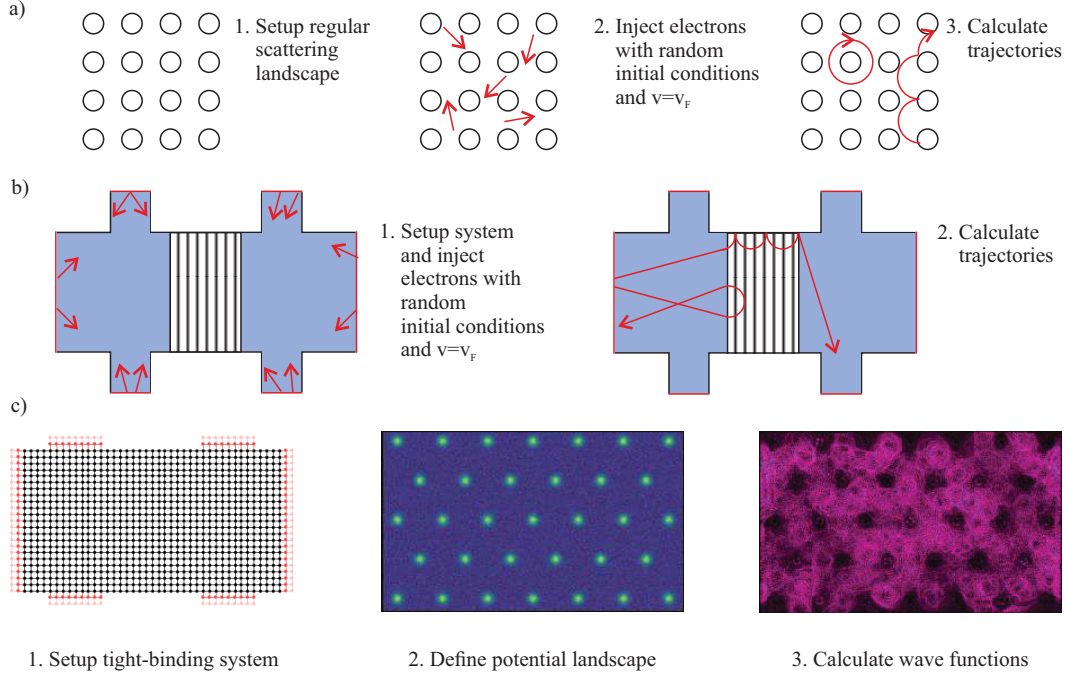
Figure 1.8: Schematics of a) the classical Kubo formalism, b) the classical Landauer-Büttiker formalism and c) a tight-binding calculation based on the Kwant package.

are placed with random initial positions inside a given system. The only admission to quantum mechanics is the fixed total velocity of the electrons at the Fermi level. The results obtained from this type of formalism have proven to be most reliable in describing periodic systems. Here all unit cells are identical and the ensemble averaging is therefore not critical. A sketch of the procedure is shown in Fig. 1.8a). The code used to perform the classical simulations in 2.2 and the related paper was adapted from code written by S. Meckler and H. Xu, which proved its reliability in earlier publications [77, 78].

1.5.2 Classical Landauer-Büttiker formalism

While the Kubo formalism is well suited for infinite and periodic systems, this is often not appropriate for describing a given experiment. In such cases, calculations based on the classical Landauer-Büttiker formalism may be preferential [79–81]. The idea behind this is to link the conductivity of a system to the transmission between contacts. For this purpose one looks at the quasi-one-dimensional modes of a system, that is finite in all but one direction. A contact is then modeled as a semi-infinite lead, which emits electrons. These electrons can then either enter another contact or be reflected to their original one. This probability translated to the transmission T. In the simplest two-contact case this results in a two-terminal

conductance G given by

$$G = \sum_{i=1}^{N} \frac{2e^2}{h} T_i, \tag{1.12}$$

where N is the number of occupied modes and T_i is their respective transmission. For the more complicated case of several contacts, one has to calculate the transmission T_{ij} from contact i to contact j. In Ref. [9] an instructive example is shown how to translate these coefficients to resistivities. In the classical case, T_{ij} is calculated by injecting electrons with a given distribution of electrons into a so called scattering region, solving Newtons equation of motion and tracking their final destination. The procedure as implemented is described in more detail in [82], while a sketch is shown in Fig. 1.8b). The classical Landauer-Büttiker formalism was used extensively in the work covered in chapter 2.1 and is based on code written by M. Cerchez. Previous publications including content from this code are Refs. [38, 82–86].

1.5.3 Tight-binding calculations based on Kwant

Classical simulations are already of great help to an experimentalist, while quantum transport calculations usually require more demanding numerical techniques and were therefore not readily available. This changed with the publication of Kwant [87]. The authors published a powerful tight-binding package as free software under a BSD license, which allows for the efficient implementation of transport calculations on systems, whose dimensions are at least close to actual samples. The package is designed as such that the user only has to define the geometry as well as the Hamiltonian of the sample under study. The actual numerics is hidden from the user. The procedure is shown schematically in Fig. 1.8c). In the following we want to give a brief summary of the underlying concepts as they are used for the 2DEGs in GaAs/Al$_x$Ga$_{1-x}$As heterostructures. The starting point is the effective mass approximation. Without a magnetic field, the Hamiltonian H can then be written as

$$H = \frac{\vec{p}^2}{2m^*} + V(x, y), \tag{1.13}$$

where $p = -i\hbar\nabla$ is the momentum operator and V is a static potential. The tight-binding approximation now consists of reduction of the continuous system to a grid and accordingly the discretization of the derivative in the momentum operator. It holds in two dimensions

$$\nabla^2 f(x,y) = \frac{f(x+a,y) + f(x-a,y) + f(x,y+a) + f(x,y-a) - 4f(x,y)}{a^2} +$$
$$+ \mathcal{O}(a^2), \tag{1.14}$$

where a is the tight-binding lattice constant. One speaks of a tight-binding system, since only the nearest neighbor coupling is included. With the introduction of the

tight-binding energy $t = \hbar^2/2a^2m^*$, this allows to write the Schroedinger equation as

$$
\begin{aligned}
H\psi(x, y) =& E\psi(x, y) \\
=& (4t + V(x, y))\psi(x, y) - \\
& - t(\psi(x + a, y) + \psi(x - a, y) + \psi(x, y + a) + \psi(x, y - a)).
\end{aligned}
\tag{1.15}
$$

One usually refers to $4t + V(x, y)$ as on-site and $-t$ as hopping energy. If one orders the sites of the lattice, this can be understood as a matrix eigenvalue problem. The solving of this problem results in an energy eigenvalue of an allowed state, while the eigenvector is the corresponding wave function. In this way, the problem of tackling a differential equation is transformed to one of linear algebra. The solving of this is implemented efficiently in Kwant. In the presence of a magnetic field, the hopping elements are modified according to the Peierls substitution [48]:

$$
t_{ij} = -t \mapsto t_{ij} = -t \exp\left(-\frac{ie}{\hbar} \int_{\vec{r}_j}^{\vec{r}_i} \vec{A} \cdot d\vec{r}.\right)
\tag{1.16}
$$

Here, $\vec{A}$ is the magnetic vector potential and the integral connects two neighboring sites in real space $\vec{r}_i$ and $\vec{r}_j$. With this at hand, it is now possible to calculate the states within a closed system, say a quantum dot. However, transport experiments are done on open experiments, where a scattering region is connected to semi-infinite leads. Since these feature translational invariance in one direction, one has the formation of modes at every energy. These modes are grouped into outgoing, incoming and evanescent ones. From the matching of the modes in the leads with the wave function in the scattering region one can now derive the coefficients of the scattering matrix S_{nm} connecting the $n-$th with the $m-$th lead. The transmission probability is then simply calculated by $T_{nm} = |S_{nm}|^2$. With these, the resistivity can be calculated as in the classical case. By similar means also other output is available, like the local density of states and the wave function inside the scattering region, which emerges from a single mode in a single lead. To ensure the validity of ones calculations, the condition $E_F < t$, which can also be written as $k_F^2 a^2 < 1$, with k_f the Fermi wave vector, must be met. This can be done by setting the value of the lattice constant a. The physical picture behind this is the need for the lattice constant to be considerably smaller than the Fermi wavelength in order to prevent numerical artifacts. Since Kwant was not used in this group before, a code sample for the calculation of the density states as well as the diagonal and Hall resistance of a Hall bar structure with a multi-probe arrangement can be found in the appendix. The implementation of leads pointing in different directions is done by the method developed by Baranger and Stone in Ref. [88]. Residual disorder can be taken into account via random on-site disorder. At each lattice point a random potential is added, whose value obeys a Gaussian distribution with zero mean. The width of the distribution V_0 can be adjusted to result in a certain mean free path ℓ (see e.g. Ref. [89])

$$
V_0^2 = \frac{a}{\ell} 2t^{3/2} \sqrt{E_F},
\tag{1.17}
$$

for a spin-degenerate 2DEG. Calculations based on Kwant are included in the publications covered in chapters 2.1 and 2.2.

2 Transport in controlled potential landscapes

2.1 Ballistic effects in single magnetic barriers

The effect of spatially inhomogeneous magnetic fields on ballistic 2DEGs has been extensively studied over the past decades [90]. One of the simplest systems that can be thought of is the so-called magnetic barrier structure. It comprises the case of a localized magnetic field spike perpendicular to the plane of the 2DEG, which is constant in one direction, while rapidly decaying in the other. The concept of magnetic barriers was first proposed from a theoretical perspective [91]. Soon after, it was realized that magnetic barriers act as an angle filter on ballistic electrons [92]. This can easily be understood in a classical picture. An electron entering the magnetic field region will undergo cyclotron motion. At a constant velocity it will depend on the angle of incidence, whether the electron will be reflected by the barrier or can be transmitted. The situation is sketched in Fig. 2.1a). When the strength of the barrier field is increased the interval of passing angles gets reduced until at some field the barrier is closed and classically no electron can pass. In experiments where one usually measures the voltage drop across the barrier region (contacts 1 and 2 in the figure), this manifests itself in an increasing resistance with barrier strength. It could be shown, however, that due to the always present edges as well as residual disorder scattering, the resistance stays finite, even if the barrier is classically closed [82]. The first experimental realization of a magnetic barrier made use of a non-planar 2DEG topology [32, 33], while later experiments preferred the stray fields of ferromagnetic films [34–36]. Since this is the approach also followed within in this thesis, we shall briefly discuss this concept here. When a thin rectangular film of a ferromagnetic material is deposited upon a semiconductor (cf. section 1.2) and magnetized by an external field parallel to the plane of the 2DEG, the resulting fringe field has a component perpendicular to it right underneath the edge of the film. Assuming homogeneous magnetization, it can be described by

$$B_z(x) = \frac{\mu_0 M(B_\parallel)}{4\pi} \ln\left(\frac{x^2 + z_0^2}{x^2 + (z_0 + h)^2}\right),\qquad(2.1)$$

where z_0 is the depth of the 2DEG, h the height of the magnetic film and $\mu_0 M$ the magnetization of the film, which depends on the external magnetic field. A sketch of the resulting field profile is shown in Fig. 2.1a). By sweeping the external field,
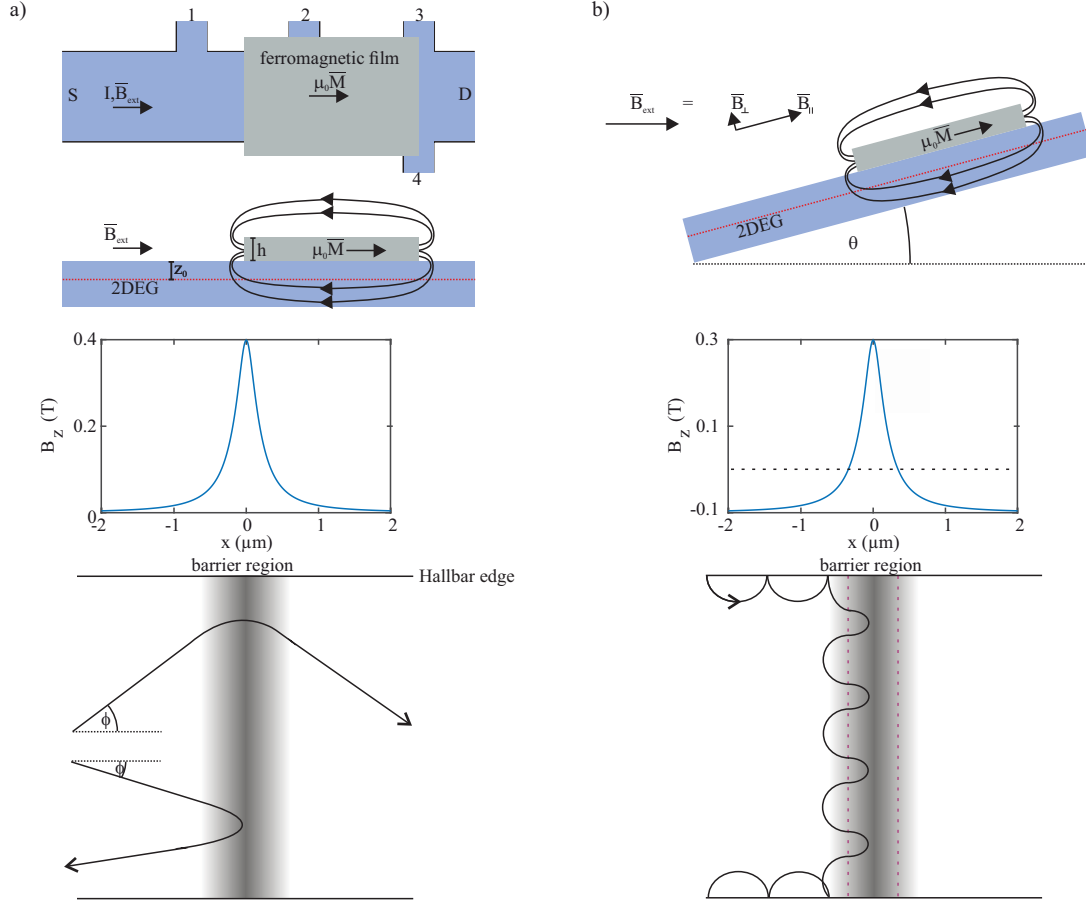
Figure 2.1: a) Top: Top view of a Hall bar structure with a ferromagnetic film deposited upon. An external magnetic field parallel to the plane of the 2DEG is applied to magnetize the film uniformly. Middle: Cross-sectional view of the structure. The stray field of the ferromagnet has a component perpendicular to the plane of the 2DEG, which is largest just beneath its edge. The resulting magnetic field profile for typical parameters is shown underneath. Bottom: Sketch of classical ballistic electron trajectories. The magnitude of the magnetic field perpendicular to the plane of the 2DEG is given by the grey scale. Depending on the angle of incidence, they are either transmitted or reflected by the magnetic barrier. b) Top: Tilting the sample away from the magnetic field by a small angle θ (greatly exaggerated in the sketch) leads to an additional homogeneous magnetic field component perpendicular to the plane of the 2DEG, while, to a first approximation, the magnetization remains unchanged. Middle: The magnetic profile within the Hall bar. The barrier field gets shifted up- or downwards depending on the angle. The dotted line corresponds to $B = 0$. Bottom: Sketch of a classical ballistic electron trajectory. Outside of the barrier region, the electron travels along the sample edges. Upon entering the barrier, it gets channeled downwards in a snake-orbit. In the sketched case a resonant reflection by the barrier is shown. (Modified after [82, 83])

the strength of the magnetic barrier can be controlled, without affecting the 2DEG outside of the barrier region. The tunability is limited by the saturation magnetization of the ferromagnetic material. Using shallow 2DEGs and ferromagnets with a high saturation magnetization, like dysprosium, this allows for the realization of peak barrier fields of up to $\approx 500\,\text{mT}$ [40] and corresponding magnetic field gradients of $\approx 3\,\text{MT/m}$. As a potential application for such structures their use as spin-filters has been discussed [93–97]. Also they form building blocks for more advanced experiments, for example when combined with quasi one-dimensional constrictions, so called quantum points contacts, where they can lead to the formation of magnetically bound states [37–40], which are of particular interest for realizing confinement in graphene based structures [98].

Naturally, the question arises, how one can determine the magnetization of the ferromagnet as a function of the external field in-situ. This information is crucial for interpreting the experimental results and also for modeling. A typical approach is the technique of Hall magnetometry. Here a magnetic structure is placed within a Hall cross and the Hall resistance is measured (contacts 3 and 4 in the figure). Conventionally one has the relation (cf. section 1.3) $R_H = B/ne$, but how is this modified, when the magnetic field is no longer homogeneous? The first naive idea might be to use the average magnetic field within the Hall cross $B \mapsto \langle B \rangle$. This allows one to calculate the magnetization from the measured Hall resistance using suitable models for the expected shape of the magnetic field profile under study. However, it turns out the introduction of an additional factor α, which takes care of the specific geometry of the localized field, is necessary [99]. The relation now reads $R_H = \alpha\langle B \rangle/ne$. Early studies discussed the properties of α in the case of diffusive [100, 101] and ballistic [99, 102] transport in the 2DEG and derived numerical values of it for different magnetic field profiles as well as for different Hall cross shapes. In case the 2DEG behaves ballistically on the scale of the Hall cross, the situation can get even more complex by making α directly dependent on the magnetization [85]. In classical terms this can be understood as an effect caused by certain types of trajectories, which are stable for a range of magnetizations and lead to an either enhanced or reduced accumulation of electrons on one side of the Hall-bar. Within the work of this thesis, we could demonstrate experimentally for the first time a situation, where the Hall resistance actually decreases in an interval of increasing magnetization due to such ballistic effects. Additionally we showed how the dependence of the magnetization on the external magnetic field could still be recovered from these data by making use of numerical simulations within a classical framework [103]. Our results are confirmed by an independent superconductive quantum interference device (SQUID, see e.g. [104]) measurement performed by our collaborators at PTB Braunschweig.

Another question that is tackled in this thesis concerns the effect that a homogeneous magnetic background field has on the transport of electrons through a magnetic barrier. Experimentally this can be realized by tilting away the sample from the parallel alignment to the external magnetic field. When the angle is small, the magnetization of the ferromagnetic film can be considered unchanged,

but an additional perpendicular field component is imposed. In this way, the localized magnetic field profile of the barrier is shifted up- or downwards as a whole. First studies of this were already reported [83], but the comparably low quality of the semiconductor heterostructure impeded the observation of ballistic effects. Of particular interest is the situation, where the magnetic barrier field and the external field are in an anti-parallel configuration. For external fields smaller than the amplitude of the barrier field, this leads to a situation, where there are two zero-magnetic-field crossings close to each other, as is sketched in Fig. 2.1b). In a classical ballistic picture, this leads to the formation of so called snake-orbits, were electrons are channeled along the zero-field line in a characteristic way [105]. Signatures of such snake trajectories have previously been reported for similar structures [106–109]. We could demonstrate, how by adjusting the offset field, one can tune the period of these snake-orbit trajectories and generate resistance oscillations stemming from their commensurability with the extension of the Hall bar [110]. With the help of tight-binding calculations based on the Kwant package (cf. section 1.5), we could clarify that the resonant reflection or transmission of electrons moving in snake-orbits is indeed the source of the observed oscillations.

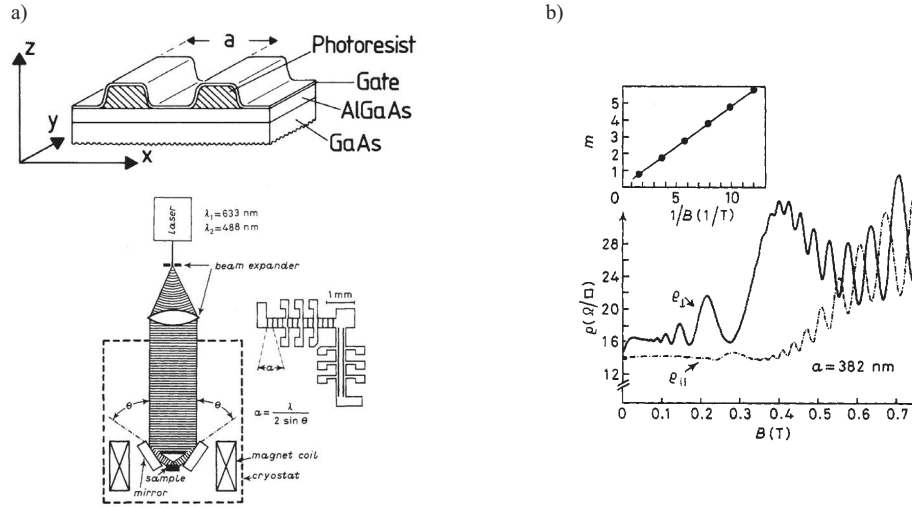## 2.2 Ballistic transport in lateral superlattices

Figure 2.2: a) Two possible experimental realizations of a one-dimensional electro-static lateral superlattice. Top: A structured top-gate is created by not removing the photoresist after lithography (taken from [24]). Bottom: Holographic scheme, where the persistent photocurrent effect is used to create a density gradient (taken from [22]). b) Magnetoresistance trace related to the latter scheme. Pronounced oscillations can be seen as a function of the magnetic field. The inset demonstrated their $1/B$ periodicity. (Taken from [22])

In the previous section we dealt with the interaction of a single magnetic barrier with the electrons in a 2DEG. In a way we can understand this as studying the scattering properties of an artificially introduced potential landscape. In this section we will now generalize this to situation, where there are lots of artificial scatterers, arranged in a periodic fashion. Such structures are commonly referred to as (lateral) superlattices. Their study became possible by advances in 2DEG quality as well as improved lithographic techniques. It became possible to generate extended systems, where the scattering of the electrons predominantly takes place at the artificially introduced structures and not the residual disorder. It is immediately clear that the Stoßzahlansatz of the Boltzmann model can not be the correct way to describe conductivity in such a system, since the scattering is highly correlated. From a theoretical point of view, superlattices are intriguing, since they allow one to study the validity of different models of electronic transport in solids. In the literature, it is often distinguished between, so called, classical, semi-classical and fully quantum mechanical models [111]. In this context, classical means that one considers the electrons as point particles moving according to Newton's equations of motion, but obeying the Fermi-Dirac statistics. An additional phase factor is taken into account within semi-classical models. They can already make features

as the Shubnikov-de Haas oscillations plausible, as a cyclotron orbit is only stable, when the resonance condition $2\pi R_c = n\lambda_F$, with n an integer and λ_F the Fermi-wavelength, is met. One also calls this the quantization of a classical trajectory. Fully quantum mechanical models start from the Schroedinger equation and do not regard electron trajectories. Although it must necessarily be the most correct description of a given system, it is usually not the most intuitive and simple one.

Historically, the first superlattices studied, consisted of a one-dimensional periodic electric field modulation [22, 24, 112] with lattice constant a. The modulation was generated using either a holographic scheme [22] or a lithographically nano-patterned gate electrode [24, 112]. Sketches of the sample geometry are shown in Fig. 2.2a). In both cases, for low magnetic fields, the authors found pronounced magnetoresistance oscillations periodic in $1/B$ in the direction of the potential gradient, say the x-direction, and weaker ones parallel to it, in y-direction. An example for a measurement is shown in Fig. 2.2b. Their origin was discussed quantum mechanically as resulting from an evolution of the Landau levels to Landau bands as a result of the superlattice potential [23, 24, 113]. Wide bands correspond to a high group velocity of electrons in y-direction, resulting in an increased conductivity. Due to the tensorial nature of resistivity, this manifests itself in an increased resistivity ρ_{xx}. The position of the resistivity can be calculated by the formula [22]

$$R_c = \frac{a}{2}\left(n - \frac{1}{4}\right),\tag{2.2}$$

where n is a positive integer and R_c the cyclotron radius. Here we have again an interplay between two length-scales, the lattice constant and the cyclotron radius, and the oscillations in ρ_{xx} are therefore also called commensurability oscillations (COs). A classical model, given by Beenakker [114], was able to reproduce the oscillations in ρ_{xx} in terms of a guiding center drift resonance, but failed to account for the weak oscillations in ρ_{yy}. Only by the incorporation of the residual disorder into a quantum mechanical treatment [113, 115] they could be recovered. Contrary to σ_{yy}, dominated by band conductivity, σ_{xx} is mainly affected by scattering between bound states, which is enlarged, when the density of states (DOS) is high. This type of conductivity is sometimes denoted as collisional or hopping conductivity. A high DOS corresponds to a situation of a narrow bandwidth, which explains, why the oscillations in ρ_{xx} and ρ_{yy} were found to be out of phase. The correct way of treating residual disorder attracted the interest of further theoretical [116–118] as well as experimental [119] studies. The temperature dependence of the COs was studied in Refs. [120, 121] and found to be rather weak, which is in agreement with an interpretation in classical terms. In this context the relevance of classical chaos was also discussed [122]. Later on, Messica et al. studied the zero-field resistance as a function of temperature and dc-bias and interpreted their results as signatures of the importance of electron-electron scattering in superlattices [123]. Further experimental studies were devoted to the DOS [124], the high field magnetoresistance [125] and the development of the quantum Hall effect for strong

modulations [126].

The transition from electrostatic to magnetic superlattices in principle is straight forward. Similar to the setup in the last section, a periodic array of ferromagnets placed on top of a 2DEG and magnetized by an external field perpendicular to the 2DEG, should introduce a periodic magnetic modulation. Calculations had already shown that very similar COs should exist in this case. The condition for minima in resistivity then reads

$$R_c = \frac{a}{2} \left(m + \frac{1}{4} \right), \tag{2.3}$$

for $m = 0, 1, 2...$ [127]. Studies of the quantum transport properties followed soon after [128, 129]. However, early attempts of realizing magnetic superlattices failed [130, 131], because the ferromagnetic gate electrodes deposited upon the semiconductor were accompanied by a piezoelectric strain potential [132–135], which was in itself an electrostatic superlattice shading the effect of the magnetic modulation. These difficulties were overcome, by either applying a positive gate voltage to the ferromagnet [28], changing to dysprosium as ferromagnet [30] or instead using superconductive materials [29] and the theoretical predictions could be confirmed. Subsequent studies revealed for example a large positive magnetoresistance for magnetization profiles with large in-plane components [136] or focused on the electron-electron scattering properties in such an environment [137]. A reversal of the phase of the Shubnikov-de Haas oscillations was discovered in electric [138, 139] as well as magnetic [140, 141] superlattices. The authors explained it in terms of a Landau band broadening, manifesting itself in a rearranged DOS, where the position of maxima and minima are opposite to the unpatterned case.

As one could expect, next we will consider two-dimensional lateral superlattices. Although there exist some experimental [31, 142–145] as well as theoretical [146–148] works on two-dimensional magnetic superlattices, they never received as much attention as their electrostatic counterpart.
Weak two-dimensional modulations were studied both, experimentally [149–151] and theoretically [152–156] in their own right, but were mostly utilized in the hunt for signatures of Hofstadters butterfly. By this we mean a self-similar quantum mechanical level structure, predicted by D. Hofstadter in 1976 [157], which should evolve for electrons on a square lattice and in a magnetic field. Later similar patterns were found e.g. for hexagonal lattices [158]. While it should also be present in regular crystal lattices, the magnetic fields, necessary in this case, are out of experimental reach. But since electrons in a high-mobility 2DEG essentially behave as free electrons, the introduction of a two-dimensional superlattice allowed for a scaling of the required magnetic field. Despite numerous theoretical predictions, see e.g. [159–161], the butterfly remained elusive [162, 163] at first, but could eventually be detected in the Hall conductance [164, 165].

Particular interest was gained by so called antidot structures. These are electrostatic superlattices in the strong modulation limit, i.e. their amplitude is above the Fermi level. They were named antidots, since they generate zones, where electrons cannot enter, often of circular shape. An example of such a lattice is shown in Fig. 2.3a). Their first implementations [25–27] focused on the classical transport properties. Pronounced COs were revealed and their origin was linked to the existence of stable electron trajectories not colliding with the antidots. A typical magnetoresistance trace is shown in Fig. 2.3b). Later on, a more involved classical analysis emphasized the dominant role of classical chaos for the emergence of the COs in antidot lattices [166–168]. Quantum effects were discovered soon after, see e.g. Refs. [169–171], and could be sufficiently understood within a semi-classical analysis [172,173], using the framework of periodic orbit theory [174]. In parallel, a large body of theoretical works, dealt with a correct quantum mechanical description of antidot lattices and discussed extensively the origins of deviations to semi-classical concepts [175–183]. A surprising connection to composite fermions (CFs) was drawn by Kang et al. [184]. They could demonstrate COs in the fractional quantum Hall regime and drew the conclusion that CFs must be *real* objects, if they follow ballistic classical dynamics. Other experimental studies dealt with e.g. the effects of a strong parallel magnetic field component [185], the interplay with residual disorder [186], the impact of microwave radiation [187] or the influence of grain boundaries in the superlattice [78].

Similar to the situation in one-dimensional superlattices described above, also in antidot lattices, the conductivity is often considered to be split between band and hopping contributions. In classical trajectories, the first originates from electrons being channeled from one antidot to another, a so called skipping orbit, whereas the latter is a result of electrons being scattered from one localized state to the next one (see sketch in Fig. 2.3a). Experimental studies on the relative importance of each transport type were conducted in square lattices [188], but due to their anisotropy rectangular lattices became the model system of choice [188–190]. There, transport is also highly anisotropic and ρ_{xx} and ρ_{yy} are dominated by band and hopping conductivity respectively. This manifests itself also in the superimposed quantum oscillations, which turned out to be out of phase, due to their different dependence of the DOS [191]. Within this work, we studied square and hexagonal antidot lattices in high-mobility heterostructures, where pronounced quantum oscillations coexist over a wide range with the COs [192]. We show experimentally and with the help of a tight-binding simulation based on the Kwant package, how in such a setup traces of both conductivity components can be found in the same resistivity component. As the magnetic field is changed, one can therefore keep track of the dominating transport mechanism, by analyzing the superimposed quantum oscillations.

A different experiment presented within this thesis combines an antidot lattice with a one-dimensional magnetic superlattice with zero mean field, which we call a
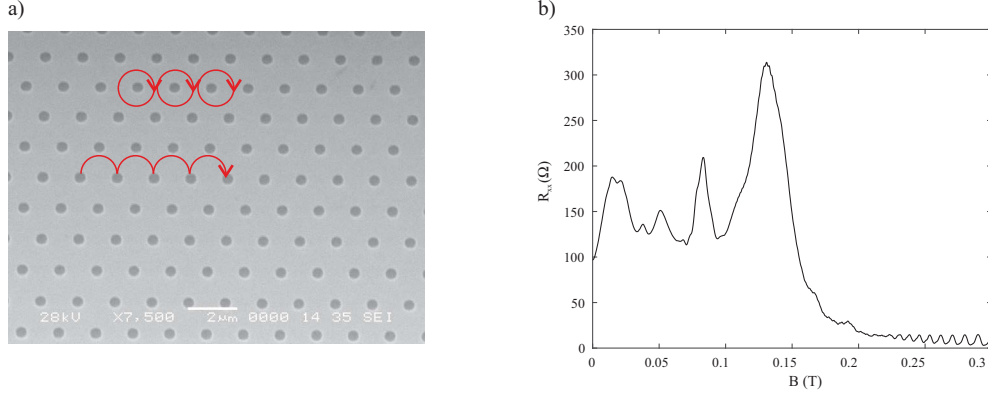
Figure 2.3: a) Electron micrograph of a hexagonal antidot lattice produced by RIE with a lattice constant of $a = 1.5\,\mu\text{m}$ and an antidot diameter of $d = 450\,\text{nm}$. The red lines sketch the different electron transport mechanisms in classical trajectories. b) Related magnetoresistance trace at $T = 0.1\,\text{K}$. Prominent oscillations appear for low magnetic fields, whereas for $B \geq 0.25\,\text{T}$ SdH type oscillations are visible.

magneto-electric hybrid lattice [193]. Hybrid systems had been considered before in the literature, but usually under the restriction of equal lattice constants and only varying relative phases [194–198]. Superlattices with vanishing mean field were studied theoretically [199, 200] and experimentally [201] before, but, to the best of our knowledge, never in combination with an antidot lattice. We find experimentally the emergence of pronounced COs as a function of the magnetization of the one-dimensional stripe lattice. We interpret them as indications of snake trajectories being commensurate with the antidot lattice period.
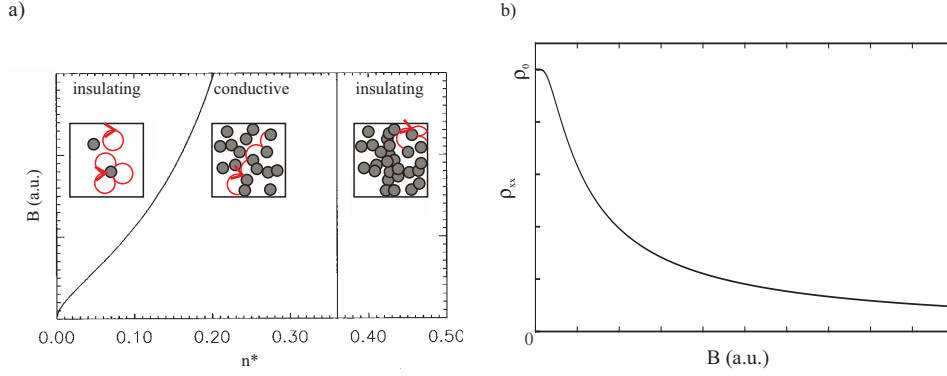
Figure 2.4: a) Phase diagram of a Lorentz gas consisting of circular obstacles. Two insulating phases are separated by a conductive phase. The insets sketch characteristic electron trajectories. In the low-density insulating phase, all electron are either undergoing undisturbed cyclotron motion in the void or are trapped at obstacles. In the conductive region, the electron are scattered from one cluster to another and can therefore traverse the whole sample region. For a further increased density of obstacles, they get trapped in pockets between obstacles. (Modified after [41]) b) Magnetoresistivity for a Lorentz gas in the Grad limit.

2.3 Classical transport properties of Lorentz gases

As was already briefly mentioned in section 1.3, in 1905 H.A. Lorentz proposed a model to describe electronic transport in solids [66], which was named the Lorentz gas due to its analogy with an ideal gas later on. The following assumptions are made in its formulation nowadays, when dealing with magnetotransport problems [18].

1. The electrons are pointlike particles, which do not interact with each other.

2. They move with constant overall velocity in two dimensions under the influence of an external perpendicular magnetic field.

3. Throughout the plane obstacles of uniform size and shape are randomly distributed with a certain density. Mutual overlaps are allowed.

4. The interaction of electrons with obstacles is short ranged. Scattered electrons are reflected specularly.

Of course, these can be modified to deal with e.g. uncharged or three-dimensional particles, which is also a topic of ongoing interest, see e.g. Refs. [202–207], but not at the scope of this work. Similar to what we discussed in the previous section, also in the Lorentz model the scattering takes place in a correlated way, since the positions of the scattering centers are fixed. The *Stoßzahlansatz* is not valid
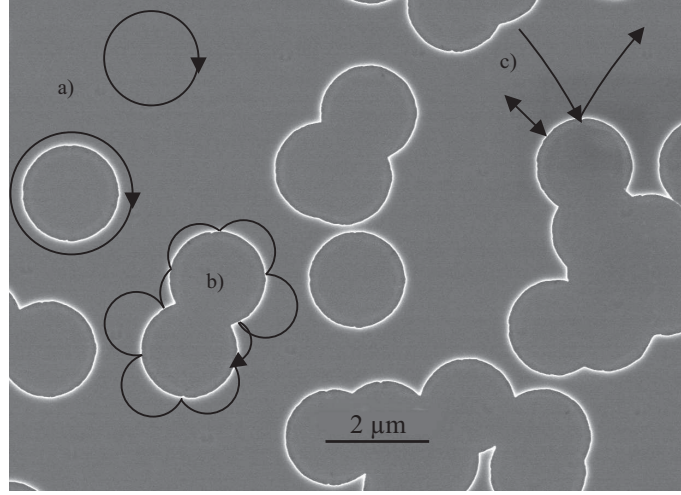
Figure 2.5: Sketch of different types of classical memory effects overlayed on top of a SEM image of an actual Lorentz model sample. a) Unperturbed cyclotron motion, either in the void or around single obstacles. b) Skipping motion along the contour of a cluster of obstacles for stronger magnetic fields. c) Backscattering by an angle of π is suppressed as the magnetic field is increased. (The e-beam lithography as well as the RIE were done by D. Kazazis, who also took the SEM image, at CNRS-C2N in Marcoussis)

and the Drude-Boltzmann description of magnetotransport is bound to fail. This complicates the theoretical description of this system and it has therefore attracted a lot of research interest over the course of the last century. Earlier studies are reviewed for example in Refs. [208–210], but here we want to focus on more recent developments.

First, we take a look at the two-dimensional phase diagram of a Lorentz system, where the magnetic field B is one and the dimensionless density of obstacles $n^* = na^2$, with the number density n and the characteristic obstacle length scale a, the other parameter. It is obvious that if the obstacle density is high enough to form a continuous cluster throughout the whole system, it will be in an insulating state. Such a cluster is called percolating. The critical densities for circles, squares and rods can be found in [211]. It is clear that the magnetic field does not have an impact on this phase boundary. When there is no open path, electrons will not be able to traverse the system, no matter if they are moving in straight lines or in circles. However, in 1978, Baskin et al. published a theoretical study on the existence of a second phase boundary, which depends on the magnetic field [212]. At a given obstacle density, there exists a critical magnetic field B_c, from which on all electrons are localized. They either move in cyclotron orbits in the void between the obstacle clusters or are trapped at their surface, moving in skipping orbits. When the cyclotron radius R_c is sufficiently small, there is no way an electron

can be transferred from one cluster to another and the system is again insulating. Kuzmany and Spohn presented the intuitive picture for circular obstacles, that for the system to be conductive, obstacles of the effective radius $a_e = a + R_c$ need to percolate [41]. This way, the electrons can reach every point in the system. The resulting phase diagram is given in Fig. 2.4a).

First quantitative theories for the magnetoconductivity were published by Bobylev et al. for the case of low obstacle densities in the so called Grad limit, which assumes $n \to \infty$ and $a \to 0$, but $na = const.$ [18, 213]. They calculated the fraction P of electrons, which undergo undisturbed cyclotron motion and therefore do not contribute to the diagonal conductivity and found

$$P = \exp\left(-4\pi R_c an\right). \tag{2.4}$$

Since the scattering centers are fixed, an electron, which can complete one cyclotron orbit, will remain in it forever. Furthermore, so called recollisions with an obstacle already visited before are possible. These kind of effects were related to the memory of the electrons, which is in stark contrast to the Stoßzahlansatz of the Boltzmann model.

The resulting magnetoresistance was found to be negative [214, 215]. In the Grad limit it reads $\rho = \rho_0(1 - P)$, where ρ_0 is the zero field resistivity. A sketch is shown in Fig. 2.4b). Interestingly this is in contrast to the case of long-range scattering, where a positive magnetoresistance was predicted [19, 21] and observed in magnetic [216–219] and electrostatic [220] environments. Negative magnetoresistance can also be caused by weak localization [221], which is a true quantum effect.

Due to the increased quality of 2DEGs in semiconductor heterostructures and progress in lithographic techniques, experimental realizations of Lorentz models became feasible. Residual disorder could be reduced, allowing for the introduction of artificial obstacles, which were big enough for treating their interaction with electrons classically. Soon after the first antidot lattices (see previous section) interest also moved to randomized arrangements of scatterers. An example of an experimental realization produced by etching circular holes at random positions into an semiconductor featuring a 2DEG beneath its surface is shown in Fig. 2.5. Early studies focused on the vanishing of the commensurability oscillations present in regular antidot lattices by adding random displacements to the antidot centers [222, 223]. While the results clearly showed a negative magnetoresistance, these could not be considered as true realizations of a Lorentz model, since there is still a non-negligible degree of order in their samples. This was changed in the work of Lütjering [224], who systematically studied random arrangements as a function of their obstacle density. Nachtwei et al. made use of Lorentz systems in the context of the quantum Hall effect [225, 226], while Yevtuchenko et al. discussed their relation to weak localization [227]. A different approach to generate short range scatterers with a random position was taken by Cina et al., who performed cyclotron resonance experiments on a 2DEG with embedded InAs dots [228]. Progress in the theoretical description allowed for a treatment of mixed disorder [20, 21], which was successfully applied to analyze the magnetoresistance found

in experiments on high-mobility heterostructures with few and large strong scatterers [229]. Rather surprising analogies to the Lorentz gas in 2DEGs were found to be realized in biological systems, namely for bacteria in the vicinity of a surface [230], magnetotactic bacteria [231] and active matter [232].

Despite all this progress in understanding and applying the properties of the Lorentz model, there still remain unanswered questions. In computer simulations of dense Lorentz gases, which defy an analytical treatment, a maximum in diagonal conductivity for finite magnetic fields is observed [41, 233], contradicting the findings of Bobylev et al. in the Grad limit. Up to now, an unambiguous experimental verification of this effect has not been published and its origin remained unclear. We studied the magnetoconductivity of dense Lorentz gases in a high-mobility 2DEG and could demonstrate the existence of a maximum for different obstacle sizes and densities [234]. With the help of molecular dynamics simulations, we could point its origin to a qualitative change of electron motion from diffuse scattering to directed transport along obstacle clusters. We interpret it as a signature of the two metal insulator transitions present in the phase-diagram of the two-dimensional Lorentz gas.

Another aspect of the Lorentz model, which has been neglected so far, is the dependence of magnetotransport on the shape of the obstacle. Almost all studies consider circular obstacles, which may partly be due to practical issues. Whenever one depletes a 2DEG locally, say by RIE, there is always some collateral damage in the surroundings. This so-called depletion zone leads to a rounding of any introduced shape. When the electron mobility of a 2DEG is low and the structural size needs to be small in order to observe ballistic effects, this makes it difficult to discriminate between different shapes. However, the depletion zone can be considered independent of the structure size and therefore has a relatively lower impact on bigger structures. We utilize this in our high-mobility 2DEG to study magnetotransport in Lorentz gases composed of circular, square and cross-shaped obstacles [235]. For square scatterers there exist some theoretical predictions for the zero magnetic field case [211, 236], whereas cross-shaped antidots were studied on a regular lattice experimentally [237]. However, to the best of our knowledge, no systematic studies concerning magnetotransport in Lorentz gases composed of these obstacles exist. Our main focus is on a memory effect, which was identified as the source of a linear negative magnetoresistance by Dmitriev et al. [238]. The authors gave a phenomenological picture, where electron backscattering by an angle of π is reduced by increasing the magnetic field. In the zero magnetic field case, a backscattered electron moves along the same trajectory it came before. The probability of it being scattered again is therefore zero for a certain interval of time. This leads to an increase in resistance, which is then suppressed by the bending of the trajectory as the magnetic field is ramped up. Later on a more sophisticated model was built around this intuitive picture [239–241]. Although this linear negative magnetoresistance was observed before in randomized antidot arrays [222], corrugated surfaces [242] and systems with interface roughness [243], it was never systematically studied in terms of its dependence of obstacle size,

shape and density.

3 Publications

The papers resulting from this work are given in this chapter. Four of them are already published, one is accepted for publication and one is still under review. The papers related to chapter 2.1 are:

1. *Probing magnetic microstructures with quasi-ballistic Hall crosses*, S. Fasbender, J. Schluck, M. Cerchez, T. Heinzel, S. Sievers, K. Pierz, and H. W. Schumacher, Journal of Applied Physics 119, 094302 (2016)

2. *Commensurability oscillations by snake-orbit magnetotransport in two-dimensional electron gases*, A. Leuschner, J. Schluck, M. Cerchez, T. Heinzel, K. Pierz, and H. W.Schumacher, Phys. Rev. B 95, 155440 (2017)

The papers related to chapter 2.2 are:

1. *Quantum signatures of competing electron trajectories in antidot superlattices*, J. Schluck, J. Feilhauer, D. Kazazis, U. Gennser, K. Pierz, H.W. Schumacher, and T. Heinzel, submitted to Phys. Rev. B.

2. *Commensurability resonances in two-dimensional magnetoelectric lateral superlattices*, J. Schluck, S. Fasbender, T. Heinzel, K. Pierz, H. W. Schumacher, D. Kazazis, and U. Gennser, Phys. Rev. B 91, 195303 (2015)

The papers related to chapter 2.3 are:

1. *Nonmonotonic Classical Magnetoconductivity of a Two-Dimensional Electron Gas in a Disordered Array of Obstacles*, N. H. Siboni, J. Schluck, K. Pierz, H. W. Schumacher, D. Kazazis, J. Horbach, and T. Heinzel, Phys. Rev. Lett. 120, 056601 (2018)

2. *Linear negative magnetoresistance in two-dimensional Lorentz gases*, J. Schluck, M. Hund, T. Heckenthaler, D. Kazazis, D. Mailly, U. Gennser, K. Pierz, H. Schumacher, N. Siboni, J. Horbach, and T. Heinzel, accepted for publication in Phys. Rev. B (2018)

Probing magnetic microstructures with quasi-ballistic Hall crosses

S. Fasbender,[1] J. Schluck,[1] M. Cerchez,[1] T. Heinzel,[1,a] S. Sievers,[2] K. Pierz,[2] and H. W. Schumacher[2]

[1]*Solid State Physics Laboratory, Heinrich-Heine-Universität Düsseldorf, 40204 Düsseldorf, Germany*
[2]*Physikalisch-Technische Bundesanstalt, Bundesallee 100, D-38116 Braunschweig, Germany*

Hall sensing is performed on a localized magnetic field pattern using a quasi-ballistic Hall cross device. The Hall resistance shows a pronounced peak as a function of the magnetic field amplitude which is absent in the magnetization hysteresis loop. This non-monotonic response exemplifies qualitatively the failure of conventional Hall sensing. It is demonstrated how, by using a numerical simulation based on the Landauer-Büttiker model, the amplitude of the magnetic field profile can be determined from such measurements. © *2016 AIP Publishing LLC*. [http://dx.doi.org/10.1063/1.4942981]

Reference

S. Fasbender, J. Schluck, M. Cerchez, T. Heinzel, S. Sievers, K. Pierz, and H. W. Schumacher, Journal of Applied Physics 119, 094302 (2016), ©2016 AIP Publishing LLC

Copyright statement

Contributions

I designed and prepared the sample. I participated in the conductance of the experiments and contributed to manuscript writing.

Probing magnetic microstructures with quasi-ballistic Hall crosses

S. Fasbender,[1] J. Schluck,[1] M. Cerchez,[1] T. Heinzel,[1,a] S. Sievers,[2] K. Pierz,[2] and H. W. Schumacher[2]

[1]*Solid State Physics Laboratory, Heinrich-Heine-Universität Düsseldorf, 40204 Düsseldorf, Germany*
[2]*Physikalisch-Technische Bundesanstalt, Bundesallee 100, D-38116 Braunschweig, Germany*

Hall sensing is performed on a localized magnetic field pattern using a quasi-ballistic Hall cross device. The Hall resistance shows a pronounced peak as a function of the magnetic field amplitude which is absent in the magnetization hysteresis loop. This non-monotonic response exemplifies qualitatively the failure of conventional Hall sensing. It is demonstrated how, by using a numerical simulation based on the Landauer-Büttiker model, the amplitude of the magnetic field profile can be determined from such measurements. © 2016 AIP Publishing LLC.
[http://dx.doi.org/10.1063/1.4942981]

I. INTRODUCTION

Quantifying magnetic fields via the Hall resistance R_{xy} in thin conductive layers like metal sheets or low-dimensional electron gases in semiconductors is a standard concept of magnetometry.[1] If the transport in the Hall cross is diffusive and the magnetic field is homogeneous, its quantitative determination is well established. In fundamental science, however, magnetometry faces additional challenges. Ferromagnets with Curie temperatures below room temperature, like Gd or Dy, require studies in a cryogenic environment. Also, structures like magnetic domain patterns,[2,3] ferromagnetic (FM)[4–8] or superconducting[9–11] nanoparticles or superlattices,[12,13] as well as small paramagnets[14,15] generate inhomogeneous magnetic fields on a sub-micrometer scale,[10] the probing of which requires magnetic field sensors with high spatial resolution. A self-evident way to perform magnetometry on these objects is by placing them on a Hall cross prepared in a suitable semiconductor heterostructure that contains a two-dimensional electron gas (2DEG).[2–11]

The small lateral dimension of the Hall cross provides spatial resolution down to the sub-micrometer regime, while the low electron density ensures a high resolution of about 1000 Bohr magnetons.[10]

Particularly relevant for the present work is the fact that many experiments comprising inhomogeneous or localized magnetic field textures are carried out at low temperatures, for example, in relation to mesoscopic systems like magnetic superlattices,[12,13,16] magnetic stripes as spin filters for electrons in a semiconductor heterostructure,[17] or quantum dot systems where the inhomogeneous magnetic field is a part of the spin readout concept.[18] In these studies, the Ga[Al]As heterostructure is frequently used due to its superior performance in terms of electron mobility and versatility. Therefore, there is a common interest to characterize the magnetic properties in such structures on-chip.

However, quantitative magnetometry is non-trivial under these conditions, due to the fact that the magnetic field is not uniform. It is well known that this non-uniformity causes deviations of R_{xy} from the homogeneous case and has been frequently accounted for using the rough approximation that the Hall voltage is proportional to the average magnetic field in the Hall cross using the *correction factor* α

$$R_{xy} = \alpha \frac{\langle B_z \rangle}{ne}, \tag{1}$$

where $\langle B_z \rangle$ denotes the average perpendicular magnetic field in the Hall cross, e is the elementary charge, and n is the two-dimensional electron density. In the diffusive case, the problem can be solved by calculating the response function of the Hall cross.[19] This must be completed for every particular size and geometry of the Hall cross-magnetic structure system. The same is true for the ballistic case where Landauer-Büttiker formalism is employed[20,21] to calculate the Hall voltage depending on the shape and geometry of the system. The conclusion from these studies is that α is not a proportionality constant, but rather a nontrivial function of the magnetic field profile $B_z(x, y)$ and of the geometry of the Hall sensor.[21] It is further known that for some shapes of $B_z(x, y)$ whose lateral extensions are small in comparison to the size of a ballistic Hall cross, $\alpha \approx 1$,[4,20,22] and $\alpha > 1$ is possible for extended magnetic fields.[3,10] In general, however, the dependence of α on the parameters of the system is not well known. This has impeded quantitative Hall magnetometry in many experimental studies.[7,8,16,23–32] The problem has been dealt with in different ways. Some authors restrict themselves to a qualitative discussion,[7,26–29] while others assume $\alpha = 1$ as a coarse approximation,[8,11,23,24,31,32] discuss only the measurements for extremal values of α,[25] or use an ad hoc approximation based on a comparison to numerical studies of α.[16] Therefore, a method to evaluate α as a function of the applied magnetic field for a given sample geometry and for typical experimental parameters, in particular, for some specific magnetic structures on top of quasi-ballistic Hall crosses, is desirable.

Here, we demonstrate that α can be obtained combining experiment and numerical simulations based on the Landauer-Büttiker model in the semiclassical limit and used to determine the amplitude of a magnetic field profile $B_z(x, y)$ for a magnetic

a)thomas.heinzel@hhu.de

barrier having a width of roughly 400 nm. The method is universal in the sense that it works for arbitrary geometries, provided that the functional form of $B_z(x, y)$ is known, the Hall sensor is in the quasi-ballistic regime, and quantization effects can be neglected. The magnetic barrier is produced by a ferromagnetic film that partially covers a quasi-ballistic Hall cross. It generates a pronounced peak in R_{xy} as a function of its magnetization $\mu_0 M$. As the temperature is increased, the peak vanishes and a conventionally shaped Hall resistance $R_{xy}(\mu_0 M)$ develops. This is a clear example where the assumption of a constant α fails.

The paper is organized as follows. In Section II, the sample layout and the experimental setup are described. Section III focuses on the experimental results and their interpretation. The method for determining the magnetic field amplitude from ballistic Hall data is presented in Section IV. We end with a summary and our conclusions in Section V.

II. SAMPLE PREPARATION AND EXPERIMENTAL SETUP

A Hall cross is prepared from a GaAs/Al$_{0.3}$Ga$_{0.7}$As heterostructure that contains a 2DEG 90 nm below the surface. In order to ensure the experiment takes place well into the ballistic regime, a high mobility heterostructure is used. After illuminating the sample with an infrared light pulse of 5 s duration, an electron density of $n = 3.36 \times 10^{15}$ m^{-2} and a mobility of 574 m^2/V s are measured at a temperature of $T = 1.5$ K. This corresponds to an elastic mean free path of $\ell = 55 \, \mu$m. A Hall cross with an area of $10 \, \mu$m $\times$ $10 \, \mu$m is defined using optical lithography and subsequent wet chemical etching. We have opted for a one-dimensional magnetic barrier as a model structure, since the analytical expression for its magnetic field profile $B_z(x, y)$ has been shown in several experiments[16,25,31,33] to describe accurately the barrier's effects on the electron transport in a 2DEG underneath. The sample layout is shown in Fig. 1. After covering the surface with a Cr film of 5 nm thickness, a dysprosium (Dy) pad with a thickness of $h = 250$ nm is deposited with one edge located at the center of the Hall cross ($x = 0$) and aligned parallel to the direction of the Hall field, i.e., along the y direction, see Fig. 1. Dy is used due to its large saturation magnetization $\mu_0 M_s \leq 3.7$ T (Ref. 34) and its compatibility with the GaAs processing technology. To ensure identical

conditions, the section of the Hall bar used to measure the carrier density and the scattering times was also covered by the Cr electrode. A second Dy film with an area of 4 mm $\times$ 4 mm and of the same thickness was prepared on GaAs under identical conditions for comparative superconducting quantum interference device (SQUID) magnetometry.

The transport experiments were performed in a ^{4}He gas flow cryostat with a variable temperature insert and a minimum temperature of $T = 1.5$ K. The cryostat is equipped with a solenoid of 8 T maximum magnetic field strength. For comparison, SQUID-magnetometry was performed in a ^{4}He gas flow cryostat equipped with a 7 T magnet and with a base temperature of 1.8 K. The magnets are used to apply a homogeneous magnetic field B_x along the transport (x) direction, which magnetizes the Dy film according to an *a priori* unknown magnetization function $\mu_0 M(B_x)$. The 2DEG responds predominantly to B_z, which is formed by the z component of the Dy film's fringe field given by[25]

$$B_z(x, B_x) = \frac{\mu_0 M(B_x)}{4\pi} \ln \left[\frac{x^2 + d^2}{x^2 + (d+h)^2} \right], \qquad (2)$$

where d is the distance of the Dy pad to the 2DEG. This magnetic barrier has a full width at half maximum of $2\sqrt{d(d+h)}$ which in our implementation equals 370 nm. $R_{xy}(B_x)$ is obtained by applying an AC current of 100 nA amplitude with a frequency of 17.7 Hz from source S to drain D, and by measuring the voltage difference between the two Hall probes.

III. EXPERIMENTAL RESULTS AND INTERPRETATION

In Fig. 2(a), the magnetization of the Dy film is shown as a function of B_x as measured by SQUID magnetometry at $T = 1.8$ K. A typical, monotonic magnetization curve is observed with a coercive magnetic field of $B_c = 740$ mT and a maximum magnetization, which is not yet fully saturated at $|B_x| = 7$ T, of $\mu_0 M_{max} \approx 2.7$ T. The Hall resistance $R_{xy}(B_x)$ at an electron temperature $T = 1.5$ K shows a strikingly different behavior. As B_x is varied from 8 T to -8 T, R_{xy} shows extreme points at $B_x = -0.32$ T and -1.1 T and reveals a coercive magnetic field of $B_c = 670$ mT. This is somewhat smaller than the value found in SQUID magnetometry, probably because the SQUID probes the average magnetization of the film while the Hall sensor detects the fringe field at its edge. The trace is antisymmetric under reversal of the sweep direction. The Hall resistance at the extremes is roughly a factor of two larger than its value at large $|B_x|$. Notably, the traces show no further conductance fluctuations as frequently observed in semiconductor nanostructures,[35] also in some structures containing local magnetic fields.[32] We attribute this to the absence of closed electron trajectories in our Hall crosses, which impedes interference of the electron waves.

Apparently, the Hall resistance is a non-monotonic function of both B_x and $\mu_0 M$, and it is not *a priori* clear how the film magnetization can be extracted from the Hall measurement. In other words, α is a nontrivial function of B_x and can be determined from the experimental data via
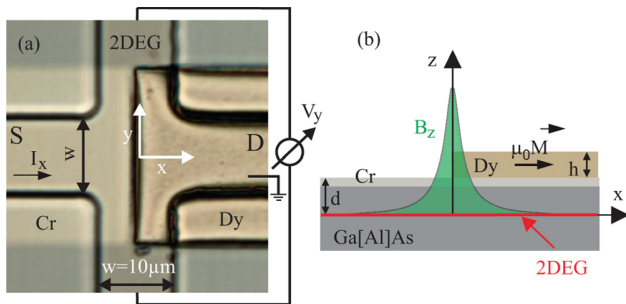

FIG. 1. Left: top view of the Hall cross as seen in an optical microscope. Right: schematic cross section in the xy plane and sketch of the perpendicular magnetic field $B_z(x)$.
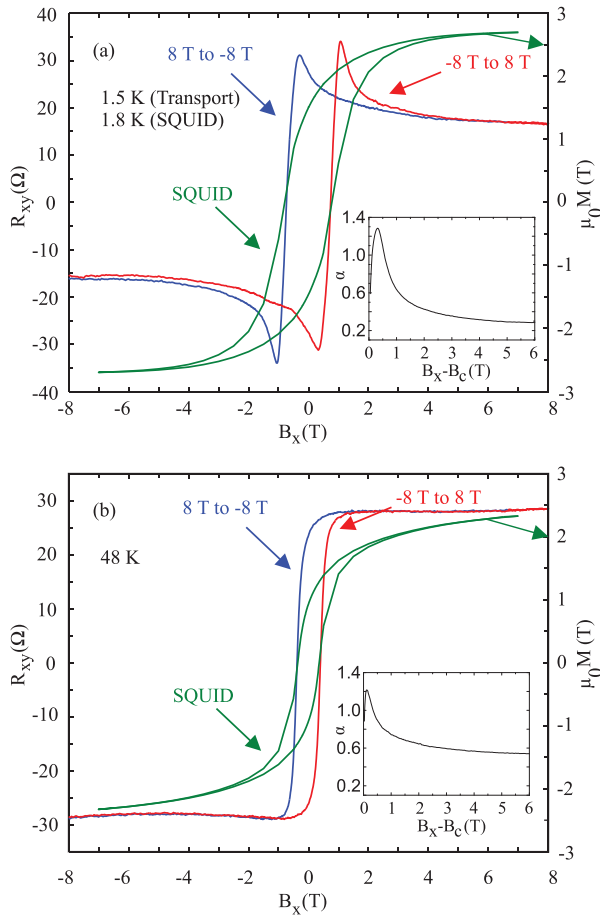
FIG. 2. (a) SQUID-magnetometry measurement and hysteretic Hall resistance as a function of B_x at $T = 1.8$ K and 1.5 K, respectively. The inset shows the magnetic field dependence of α as obtained from these measurements. The results of the same experiments carried out at 48 K are shown in (b).

$\alpha(B_x) = enR_{xy}(B_x)/\langle B_z \rangle(B_x)$, where $\langle B_z \rangle(B_x)$ is obtained from the SQUID magnetometry and with Equation (2). The resulting $\alpha(B_x)$-function, shown in the inset, varies by more than a factor of 4 and peaks at $B_x - B_c \approx 350$ mT, with a maximum value of ≈ 1.3.

As T is increased, the non-monotonic behavior becomes weaker and finally vanishes at $T \approx 48$ K, see Fig. 2(b). The SQUID measurement shows that the magnetization at $B_x = 7$ T has decreased to 2.33 T and the coercive magnetic field to 360 mT. Despite this qualitative convergence of the SQUID- and the Hall measurement, α is still magnetic field dependent and differs significantly from 1, as shown in the inset. The qualitative dependence of $\mu_0 M$ on B_x as measured with the SQUID is, in several respects, expected for granular Dy films. First of all, saturation of the magnetization may require magnetic fields larger than 8 T.[34,36] Second, a comparison of B_c and the shape of $\mu_0 M(B_x)$ to reports in the literature shows consistency with the assumption of a granular structure that has been reported to comprise a mixture of strained hcp and fcc granules of typical sizes around 20 nm.[34,37] Also, it has been shown that the FM-antiferromagnetic (AFM) transition of Dy single crystals at a Curie temperature of $T_c = 85$ K (Refs. 38 and 39) can be replaced by multiple magnetic transitions in granular films.[34] The onset of the AFM state can be

increased to about 100 K,[40] above which the AFM and FM phases can coexist, such that the ferromagnetic response can persist up to $T = 172$ K.[34] This is in agreement with our SQUID measurements, which reveal a vanishing magnetization at a temperature of 171 K (not shown).

Therefore, it becomes apparent that the anomalous Hall resistance must be related to the electronic properties of the Hall cross. This cannot be explained by a temperature-dependent electron density n, which only decreases by 4% as the temperature is increased from 1.5 K to 48 K, similar to earlier observations.[41] However, the Drude scattering time τ varies by about one order of magnitude over this temperature interval, and the elastic mean free path $\ell = \hbar\sqrt{2\pi n}\,\tau/m^*$ decreases from 55 μm at 1.5 K to 3.2 μm at 48 K. Therefore, the increase in temperature causes a transition from the quasi-ballistic into the quasi-diffusive regime, and the previous considerations thus suggest that this transition substantially influences the Hall signal.

To gain more insight into the non-monotonic evolution of $R_{xy}(B_x)$, we simulated R_{xy} while varying the saturation magnetization between $\mu_0 M_s = 0$ and $\mu_0 M_s = 3$ T, using the Landauer-Büttiker formalism in the semiclassical limit,[42] which excludes quantum interference effects. The geometry and sizes given in Fig. 1 are used, and the corners of the Hall cross are assumed to be sharp. 10^6 electrons are injected with the Fermi velocity from each contact, using a cosine distribution of the initial velocity orientations. The starting points are randomly distributed along a cross-sectional line of the contact. Scattering is included with a Poisson distribution of scattering times with the expectation value τ_q, the quantum scattering time. The width of the gaussian scattering angle distribution is chosen such that the calculated resistivity, which determines the Drude scattering time τ, agrees with the experimental one in the Hall bar at zero magnetic field. We can determine τ_q, which is obtained from the envelope of the Shubnikov–de Haas oscillations at low magnetic fields,[43] up to a temperature of 4 K and find the values $\tau_q(1.5\,\text{K}) = 0.6$ ps, $\tau(1.5\,\text{K}) = 218$ ps, $\tau_q(4\,\text{K}) = 0.35$ ps, $\tau(4\,\text{K}) = 89$ ps, and $\tau(48\,\text{K}) = 16$ ps. The electron trajectories are calculated, solving the classical equations of motion of the electrons in the presence of a magnetic field, and zero-electric field. Hard walls are simulated by mirror reflections at the edges of the Hall bar. Calculating the electron transmission probability between each contact and any other allows us to obtain the elements of the conductance matrix $G_{ij}(\mu_0 M)$, $(i, j \epsilon \{1.4\})$ which, in turn, determines $R_{xy}(\mu_0 M)$ (see also Ref. 44). The Landauer-Büttiker formalism extended here into the semi-classical limit is strictly precise in the absence of random scattering. The electrons move in zero-bias, with constant velocity, and the Hall voltage cannot be correctly calculated in the diffusive regime due to the lack of drift velocity in the absence of an electric field. The potential difference between Hall probes is given by the number of electrons that pile up in the two contacts, however if randomizing scattering is present, the model will fail and the predicted difference between Hall probes will be zero. The details of this simulation method and its limitations have been described in Refs. 21 and 31. Since both scattering times are strongly temperature dependent, the simulations

become less reliable for temperatures above 4 K where the width of the scattering angle distribution can only be guessed; hence, Section IV will focus on the low temperature regime.

Fig. 3(a) shows the simulation results for $R_{xy}(\mu_0 M)$ for different quantum scattering times. For an unrealistically large $\tau_q = 100$ ps, corresponding to a quantum scattering length of 25 μm and a mean free path in the millimeter range, the Hall cross resides deep inside the ballistic regime. For low values of the magnetization ($\mu_0 M < 1$ T), $R_{xy}(\mu_0 M)$ is linear. A pronounced peak develops at $\mu_0 M \approx 1.4$ T. As $\mu_0 M$ is further increased, R_{xy} decreases and saturates at about one third of the peak value. Decreasing τ_q leads to a successive suppression of the peak in $R_{xy}(\mu_0 M)$. The correction factor $\alpha(\mu_0 M)$ is obtained by inserting the calculated values for $\langle B_z \rangle$ according to Eq. (2) and the simulated $R_{xy}(\mu_0 M)$ into Eq. (1). The result is shown in the inset of Fig. 3(a), where α has been plotted as a function of the characteristic cyclotron

radius inside the Hall cross, defined as $r_c^* = \hbar\sqrt{2\pi n}/|e\langle B_z \rangle|$. It can be seen that the peak appears close to $2r_c^* \approx w$, the width of the Hall cross.[21] As r_c^* decreases, α decreases significantly below 1 to a minimum value of 0.2.

To shed some light on the origin of the R_{xy} peak, it is helpful to look at some characteristic trajectories of electrons after their injection into the Hall cross from the left contact, see Fig. 3(b). At small magnetization, the electrons typically probe the whole Hall cross and can be collected in all contacts, depending on their angle of injection γ, similar to their motion in a homogeneous magnetic field. Therefore, α is ≈ 1 for large r_c^*. Close to the R_{xy} peak, the collection by the bottom contact is increased, while at the same time, collection by the top contact takes place for an interval of positive γ in which the trajectories contain self-intersecting loops, see the case of $\mu_0 M = 1.4$ T in Fig. 3(b) for an illustration. For large γ, however, the magnetic barrier is open, and the electrons end up in the right contact. This scenario contributes to the increase of R_{xy} corresponding to $\alpha > 1$. The presence of trajectories in the shape of deformed cyclotron semicircles, corresponding to transmission from the left into the right contact, is characteristic here. This explains qualitatively the rule of thumb that the peak in R_{xy} appears roughly where $r_c^* \approx w$. At larger magnetization, like $\mu_0 M = 2.5$ T in Fig. 3(b), the magnetic barrier is closed, and the electrons entering at large γ are now also transmitted into the top contact. This decreases the difference between the number of electrons collected at the top and bottom contacts, and consequently, α decreases. The residual value of R_{xy} reflects the fact that the injected electron distribution is deflected towards the bottom contact by the tail of the magnetic barrier, which makes a collection by the bottom contact more likely. In this scenario, the microscopic role of randomizing scattering can also be readily explained. An electron suffering a scattering event inside the magnetic barrier may change its direction such that it gets transmitted into the right contact. Thus, scattering effectively reopens the magnetic barrier, and the electrons can probe the full Hall cross area again. The characteristic trajectories furthermore illustrate that the non-monotonic behavior depends only weakly on the sharpness of the corners of the Hall cross, since the causal scattering takes place close to the center of the magnetic barrier. This is confirmed by calculations for a Hall cross with rounded corners with a radius of curvature of 1 μm, see the lower right part of Fig. 3(b), and stands in contrast to the prominent role the shape of the Hall cross edges plays in smaller ballistic Hall crosses exposed to homogeneous magnetic fields for the observed non-monotonic or even negative Hall resistance.[45–48]
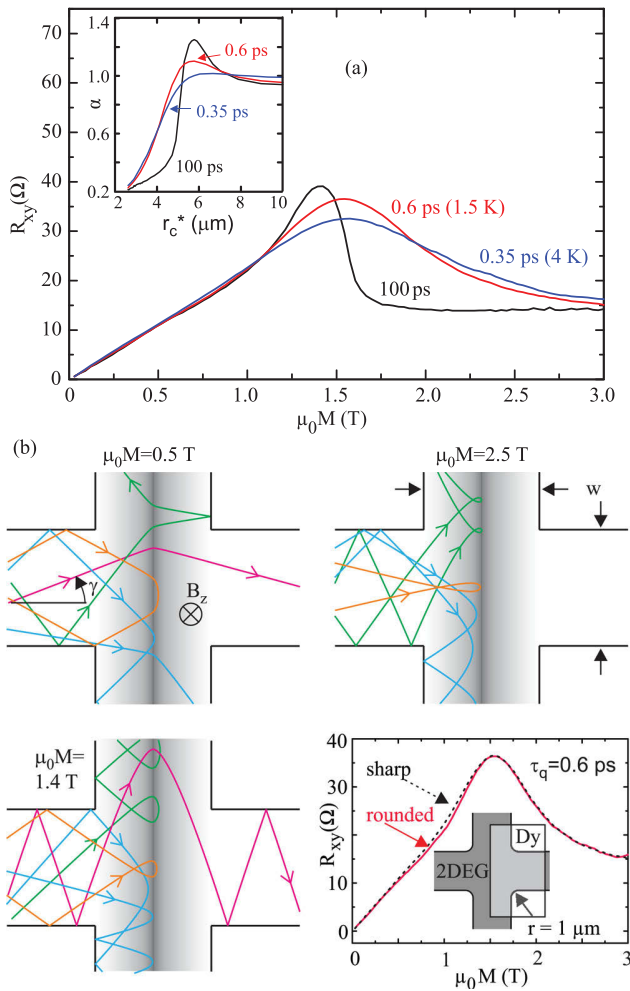

FIG. 3. (a) Simulation of the Hall resistance as a function of the magnetization for various quantum scattering times, some of which correspond to a temperature in the experiment as indicated. Inset: the corresponding calculated correction factors as a function of the characteristic cyclotron radius r_c^*. (b) Characteristic trajectories for a magnetization below (upper left), at (lower left), and well above (upper right) the maximum of $R_{xy}(\mu_0 M)$ for $\tau_q = 100$ ps. $B_z(x)$ is indicated by the gray tone and points into the plane. Lower right: Calculated function $R_{xy}(\mu_0 M)$ for a magnetic barrier on top of a Hall cross with sharp as well as for one with rounded corners.

IV. QUANTITATIVE HALL SENSING FOR CORRECTION FACTORS $\alpha \neq 1$

The results described above suggest that even from Hall measurements in the quasi-ballistic regime, the amplitude of $B_z(x, y)$, or in our present example equivalently the magnetization of the Dy pad, can be determined by dividing the measured Hall resistance by the calculated correction factor α. The validity of this approach can be demonstrated by

comparing the corrected ballistic trace $R_{xy}(B_x)/\alpha(\mu_0 M)$ at $T = 1.5$ K with the corresponding SQUID measurement of the magnetization. Equating the measured Hall resistance $R_{xy}(B_x)$, shown in Fig. 2(b), with the computed values $R_{xy}(\mu_0 M)$ in Fig. 3(a) allows us to transform the magnetization into the corresponding value for B_x. Due to the non-monotonic functions, this must be done in two intervals, the first one ranging from B_x, $\mu_0 M = 0$ to the maximum of R_{xy}, and the second one for larger B_x and $\mu_0 M$ values. It should be noted that close to the maximum, there is a small interval 0.25 T $< B_x - B_c < 0.4$ T where this mapping fails since the computed values for R_{xy} exceed the measured ones, and where therefore the relation $B_x(\mu_0 M)$ cannot be defined.

The measured Hall resistance is transformed into $\mu_0 M(B_x)$ by dividing each measured value $R_{xy}(B_x - B_c)$ by the computed $\alpha(B_x - B_c)$, and the subsequent replacement of $\langle B_z \rangle$ by $\mu_0 M$ according to Eq. (2). The α-corrected magnetization as obtained this way from the Hall measurement is shown in Fig. 4. Its dependence on B_x is now monotonic and the values obtained for the magnetization, shown at the right vertical axis, are in good agreement with the SQUID measurements, in particular at large magnetic fields $B_x - B_c > 3$ T, where the magnetizations differ by less than 4%.

In smaller magnetic fields, the deviations become larger. This may be due to the different spatial regions probed by the two techniques: while the SQUID magnetometry measures the averaged magnetization of the whole Dy film, the Hall measurement determines the magnetization from the stray field at the edge. As the magnetic field is increased, the magnetization homogenizes and thereby leads to a convergence of the two measurement concepts. This method of determining the amplitude of $B_z(x, y)$ is of potential relevance for experiments where Hall magnetometry is to be performed with Hall crosses that cannot be driven into the diffusive regime: it shows that by computing α numerically, the strength of $B_z(x, y)$ can still be determined, although the result is conditioned by its functional form that is required as an input. It should be noted that this analysis requires the experimental determination of τ_q, which via transport experiments is only possible at sufficiently low temperatures. The
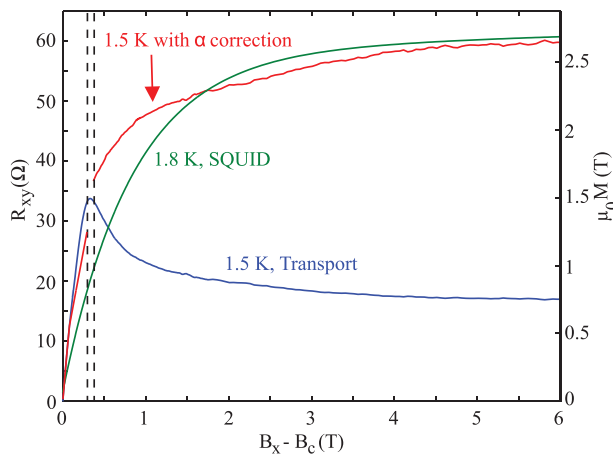
discussion also suggests application of the presented approach to scanning Hall probe microscopy.[49,50] Here, the position of the Hall cross with respect to the magnetic texture is varied quasi-continuously. Since the correction factor may be a function of the probe position, the quantification of the magnetic profile could be improved by weighing the Hall resistance by the computed function $\alpha(x, y)$.

At elevated temperatures like the one shown in Fig. 2(b), a quantitative correction of R_{xy} along these lines is no longer possible. First of all, the angular distribution of the scattering is required as an input, and therefore the quantum scattering time is required. Second, as the Hall cross enters the quasi-diffusive regime, electric fields build up and generate $\vec{E} \times \vec{B}$-drifts, which in the diffusive limit cause the Hall voltage. These effects are disregarded in our model. The data, however, show that even for $T = 48$ K, the assumption of a constant α is too simplistic and tends to underestimate the true value of the magnetization of the Dy film close to saturation.

V. SUMMARY AND CONCLUSIONS

Hall sensing of a magnetic nanostructure with a relatively large Hall cross well inside the ballistic regime was performed. A strongly non-monotonic Hall resistance as a function of the amplitude of the localized magnetic field pattern $B_z(x, y)$ was observed, an effect which impedes quantitative Hall sensing. This anomaly is quite robust and persists even when the electron mean free path is smaller than the width of the Hall cross, a regime usually classified as diffusive or quasi-diffusive. Conventional, monotonic response can be recovered when the Hall cross is deep inside the diffusive regime, i.e., the mean free path should be at least one order of magnitude smaller than the dimensions of the Hall bar. This is not always possible. For example, increasing the temperature to reach the diffusive regime may be hampered by exceeding the Curie temperature for ferromagnetic nanostructures, or by the limits set by the transition temperature for superconductive samples. It may also be difficult to increase the size of the Hall bar, since the sensitivity will suffer. Therefore, it is of relevance to be able to correct for the deviations generated by the ballisticity, and we have demonstrated that this can be done by a numerical simulation of the Hall correction factor α as a function of the amplitude of $B_z(x, y)$, the functional form of which, however, is required as an input and therefore represents a possible error source. In the presented example, the error of the magnetometry at large magnetization has been decreased from a factor of 3.5 to $\lesssim 4\%$. Moderate thermal smearing as well as imperfections of the Hall cross geometry have only a marginal effect on the correction factor.

In situations where both the amplitude and the spatial distribution of the magnetic field are unknown, it will most likely not be possible to extract both from the measured magnetic field dependent Hall resistance. Rather, the concept presented in this work should be useful for experiments where a micromagnet of a well-defined shape is used to generate a certain magnetic texture. In addition to the magnetic barrier we have used, the arrays thereof as well as

FIG. 4. Comparison between the α-corrected magnetization as obtained from the Hall measurement, and the SQUID magnetometry in the ballistic regime. The measured data of $R_{xy}(B_x)$ are shown as well.

ferromagnetic or superconducting cylinders, both single and in arrays, and thin ferromagnetic wires are typical examples. For such structures, the ideal (monodomain) magnetic fringe field is well-known and can therefore be used as an input. It would be useful to establish a set of α-functions for the most common magnetic microstructures as a reference for magnetometry on such ferromagnet/heterostructure systems.

ACKNOWLEDGMENTS

[1]S. M. Sze, *Semiconductor Sensors* (Wiley Interscience, New York, 1994).

[2]K. S. Novoselov, A. K. Geim, S. V. Dubonos, E. W. Hill, and I. V. Grigorieva, Nature **426**, 812 (2003).

[3]D. A. Christian, K. S. Novoselov, and A. K. Geim, Phys. Rev. B **74**, 064403 (2006).

[4]L. Theil Kuhn, A. K. Geim, J. G. S. Lok, P. Hedegård, K. Ylänen, J. B. Jensen, E. Johnson, and P. E. Lindelof, Eur. Phys. J. D **10**, 259 (2000).

[5]Y. Li, P. Xiong, S. von Molnar, Y. Ohno, and H. Ohno, J. Appl. Phys. **93**, 7912 (2003).

[6]K. J. Kirk, S. McVitie, A. R. Long, and E. Skuras, J. Appl. Phys. **93**, 7906 (2003).

[7]D. Reuter, S. Hoch, B. Hausmanns, B. Stahlmecke, G. Dumpich, R. Wieser, U. Nowak, and A. D. Wieck, J. Magn. Magn. Mater. **272**, 1654 (2004).

[8]G. Mihailovic, A. Hoffmann, and S. von Molnar, J. Appl. Phys. **106**, 074518 (2009).

[9]A. K. Geim, I. V. Grigorieva, S. V. Dubonos, J. G. S. Lok, J. C. Maan, A. E. Filippov, and F. M. Peeters, Nature **390**, 259 (1997).

[10]A. K. Geim, S. V. Dubonos, J. G. S. Lok, I. V. Grigorieva, J. C. Maan, L. T. Hansen, and P. E. Lindelof, Appl. Phys. Lett. **71**, 2379 (1997).

[11]S. Pedersen, G. R. Kofod, J. C. Hollingbery, C. B. Sørensen, and P. E. Lindelof, Phys. Rev. B **64**, 104522 (2001).

[12]H. A. Carmona, A. K. Geim, A. Nogaret, P. C. Main, T. J. Foster, M. Henini, S. P. Beaumont, and M. G. Blamire, Phys. Rev. Lett. **74**, 3009 (1995).

[13]P. D. Ye, D. Weiss, R. R. Gerhardts, M. Seeger, K. von Klitzing, K. Eberl, and H. Nickel, Phys. Rev. Lett. **74**, 3013 (1995).

[14]G. Mihailovic, K. Aledealat, P. Xiong, S. von Molnar, M. Field, and G. J. Sullivan, Appl. Phys. Lett. **91**, 172518 (2007).

[15]Y. Kim, S. Joo, W. Lee, J. Hong, S. K. Hong, K. H. Kim, S. U. Kim, K. Rhie, S. Lee, Y. Chung, and K. Shin, J. Korean Phys. Soc. **52**, 513 (2008).

[16]J. Schluck, S. Fasbender, T. Heinzel, K. Pierz, H. W. Schumacher, D. Kazazis, and U. Gennser, Phys. Rev. B **91**, 195303 (2015).

[17]J. Wrobel, T. Dietl, A. Lusakowski, G. Grabecki, K. Fronc, R. Hey, K. H. Ploog, and H. Shtrikman, Phys. Rev. Lett. **93**, 246601 (2004).

[18]Y. S. Shin, T. Obatao, Y. Tokura, M. Pioro-Ladriere, R. Brunner, T. Kubo, K. Yoshida, and S. Tarucha, Phys. Rev. Lett. **104**, 046802 (2010).

[19]I. S. Ibrahim, V. A. Schweigert, and F. M. Peeters, Phys. Rev. B **57**, 15416 (1998).

[20]F. M. Peeters and X. Q. Li, Appl. Phys. Lett. **72**, 572 (1998).

[21]M. Cerchez and T. Heinzel, Appl. Phys. Lett. **98**, 232111 (2011).

[22]J. G. S. Lok, A. K. Geim, J. C. Man, S. V. Dubonos, L. T. Kuhn, and P. E. Lindelof, Phys. Rev. B **58**, 12201 (1998).

[23]M. Johnson, B. R. Bennett, M. J. Yang, M. M. Miller, and B. V. Shanabrook, Appl. Phys. Lett. **71**, 974 (1997).

[24]F. G. Monzon, M. Johnson, and M. L. Roukes, Appl. Phys. Lett. **71**, 3087 (1997).

[25]T. Vançura, T. Ihn, S. Broderick, K. Ensslin, W. Wegscheider, and M. Bichler, Phys. Rev. B **62**, 5074 (2000).

[26]V. Kubrak, A. Neumann, B. L. Gallagher, P. C. Main, M. Henini, C. H. Marrows, and B. J. Hickey, J. Appl. Phys. **87**, 5986 (2000).

[27]B. L. Gallagher, V. Kubrak, A. W. Rushforth, A. C. Neumann, K. W. Edmonds, P. C. Main, M. Henini, C. H. Marrows, B. J. Hickey, and S. Thoms, Physica E **11**, 171 (2001).

[28]Y. Li, P. Xiong, S. von Molnar, S. Wirth, Y. Ohno, and H. Ohno, Appl. Phys. Lett. **80**, 4644 (2002).

[29]H. Rolff, W. Pfützner, C. Heyn, and D. Grundler, J. Magn. Magn. Mater. **272–276**, 1623 (2004).

[30]S. Joo, J. Hong, K. Rhie, K. Y. Jung, K. H. Kim, S. U. Kim, B. C. Lee, W. H. Park, and K. Shin, J. Korean Phys. Soc. **48**, 642 (2006).

[31]M. Cerchez, S. Hugger, T. Heinzel, and N. Schulz, Phys. Rev. B **75**, 035341 (2007).

[32]S. Hugger, H. Xu, A. Tarasov, M. Cerchez, T. Heinzel, I. V. Zozoulenko, D. Reuter, and A. D. Wieck, Phys. Rev. B **78**, 165307 (2008).

[33]A. Nogaret, J. Phys.: Condens. Matter **22**, 253201 (2010).

[34]G. Scheunert, W. Hendren, A. Lapicki, P. Jesudoss, R. Hardeman, M. Gubbins, and R. M. Bowman, J. Phys. D: Appl. Phys. **46**, 152001 (2013).

[35]C. W. J. Beenakker and H. van Houten, in *Solid State Physics*, edited by H. Ehrenereich and D. Turnbull (Academic Press, 1991), Vol. 44, pp. 1–228.

[36]V. Stepankin, Physica B **211**, 345 (1995).

[37]K. Y. Mulyukov, G. F. Korzinova, and S. A. Nikitin, J. Appl. Phys. **79**, 8584 (1996).

[38]K. Niira, Phys. Rev. **117**, 129 (1960).

[39]D. Jiles, *Introduction to Magnetism and Magnetic Materials* (Chapman and Hall, London, 1998).

[40]S. Chaudhary, P. Garg, and S. Rajput, Solid State Commun. **132**, 293 (2004).

[41]S. Svensson and A. W. Swanson, J. Appl. Phys. **59**, 2870 (1986).

[42]C. W. J. Beenakker and H. van Houten, Phys. Rev. Lett. **63**, 1857 (1989).

[43]T. Ando, A. B. Fowler, and F. Stern, Rev. Mod. Phys. **54**, 437 (1982).

[44]S. Hugger, M. Cerchez, H. Xu, and T. Heinzel, Phys. Rev. B **76**, 195308 (2007).

[45]C. J. B. Ford, S. Washburn, M. Büttiker, C. M. Knoedler, and J. M. Hong, Phys. Rev. Lett. **62**, 2724 (1989).

[46]A. M. Chang, T. Y. Chang, and H. U. Baranger, Phys. Rev. Lett. **63**, 996 (1989).

[47]M. R. Roukes, A. Scherer, S. J. Allen, H. G. Craighead, R. M. Ruthen, E. D. Beebe, and J. P. Harbison, Phys. Rev. Lett. **59**, 3011 (1987).

[48]H. U. Baranger and A. D. Stone, Phys. Rev. Lett. **63**, 414 (1989).

[49]A. Oral, S. J. Bending, R. G. Humphreys, and M. Henini, Supercond. Sci. Technol. **10**, 17 (1997).

[50]V. V. Khotkevych and S. J. Bending, J. Phys.: Conf. Ser. **150**, 012021 (2009).

Commensurability oscillations by snake-orbit magnetotransport in two-dimensional electron gases

A. Leuschner, J. Schluck, M. Cerchez,[*] and T. Heinzel

Solid State Physics Laboratory, Heinrich-Heine-Universität Düsseldorf, 40204 Düsseldorf, Germany

K. Pierz and H. W. Schumacher

Physikalisch-Technische Bundesanstalt, Bundesallee 100, D-38116 Braunschweig, Germany

Commensurate magnetoresistance periodic oscillations generated by transversal electron snake orbits are found experimentally. A two-dimensional electron gas is exposed to a magnetic field that changes sign along the current longitudinal direction and is homogeneous in the transverse direction. The change in sign of the magnetic field directs the electron flow along the transversal direction, in snake orbits. This generates resistance oscillations with a predictable periodicity that is commensurate with the width of the electron gas. Numerical simulations are used to reveal the character of the oscillations.

Reference

A. Leuschner, J. Schluck, M. Cerchez, T. Heinzel, K. Pierz, and H. W. Schumacher, Phys. Rev. B 95, 155440 (2017), ©2017 American Physical Society

Copyright statement

The author has the right to use the article or a portion of the article in a thesis or dissertation without requesting permission from APS, provided the bibliographic citation and the APS copyright credit line are given on the appropriate pages.

Contributions

I wrote the quantum code based on the Kwant package and performed numerical simulations used for the interpretation of the experimental data and contributed to manuscript writing.

Commensurability oscillations by snake-orbit magnetotransport in two-dimensional electron gases

A. Leuschner, J. Schluck, M. Cerchez,[*] and T. Heinzel

Solid State Physics Laboratory, Heinrich-Heine-Universität Düsseldorf, 40204 Düsseldorf, Germany

K. Pierz and H. W. Schumacher

Physikalisch-Technische Bundesanstalt, Bundesallee 100, D-38116 Braunschweig, Germany

Commensurate magnetoresistance periodic oscillations generated by transversal electron snake orbits are found experimentally. A two-dimensional electron gas is exposed to a magnetic field that changes sign along the current longitudinal direction and is homogeneous in the transverse direction. The change in sign of the magnetic field directs the electron flow along the transversal direction, in snake orbits. This generates resistance oscillations with a predictable periodicity that is commensurate with the width of the electron gas. Numerical simulations are used to reveal the character of the oscillations.

I. INTRODUCTION

Magnetotransport phenomena in magnetic fields localized at least in one direction have been reported for some time, and the interest has been both at the fundamental and application levels [1]. Various magnetic field profiles led to effects such as commensurate oscillations [2,3], a giant magnetoresistance [4], and snake-orbit dominated transport [5]. Also magnetic wave guiding of electrons [6], resistance oscillations at magnetic edge states [7], detection of spin resonance by electron channeling along snake orbits [8], and snake-orbit induced rectification [9] were reported. Magnetic barriers, i.e., localized magnetic fields in the direction of the current which are homogeneous in the transverse direction, have been studied in great detail [10–17], and typically show a smooth magnetoresistance which is influenced by both momentum-randomizing scattering in the bulk and $\vec{E} \times \vec{B}$ drift at the sample edges [18]. Inhomogeneous magnetic fields in quantum wires, on the other hand, show phenomena such as transmission and reflection resonances [19] and can host quantum states which have no semiclassical analog [20–22]. Two-dimensional electron gases (2DEGs) exposed to inhomogeneous magnetic fields raise application interest in particular in relation to Hall magnetometry on magnetic micro- or nanostructures [23–29] and to solid-state spin filters [30–35]. More recently, localized magnetic fields at quantum dots were used to manipulate single spins [36,37] and to demonstrate electrical control of a spin qubit [38]. In applications such as these, it is potentially important to develop a thorough understanding of the possible magnetotransport outcome that the magnetic field profile may generate.

In the general effort of understanding and exploiting the potential of localized magnetic fields, this paper reports the observation of magnetoresistance periodic oscillations in localized magnetic fields, which are due to transverse electron snake orbits commensurate with the spatial extension of the 2DEG. The interpretation of the experimental results is based on classical and quantum simulations showing, through classical electron trajectories as well as the

electron local density of states, how the transversal snake-orbit electron transport is responsible for the magnetoresistance oscillations.

Section II describes the geometry and preparation of the samples. The experimental results and their interpretation are presented in Sec. III. The paper closes with conclusions in Sec. IV.

II. SAMPLE PREPARATION, EXPERIMENTAL SETUP, AND CHARACTERIZATION MEASUREMENTS

The samples were prepared from two $GaAs/Al_{0.3}Ga_{0.7}As$ heterostructures (samples A and B). The 2DEG in sample A is located $d = 150$ nm below the surface and had, after illumination with an infrared light-emitting diode for a few seconds, an electron density of $n = 2.7 \times 10^{15}$ m^{-2} and a mobility of $\mu = 168$ m^2/Vs at a temperature of ≈ 100 mK. The corresponding values for sample B were $d = 90$ nm, $n = 3.5 \times 10^{15}$ m^{-2}, and $\mu = 131$ m^2/Vs. Optical lithography and wet chemical etching were used to define a Hall bar of $w = 10$ μm width in the y direction. This is smaller than the mean free path of 14 μm in sample A and 12 μm in sample B, such that the electrons could cross the Hall bar ballistically. After covering the surface with a Cr film of 5 nm thickness, a ferromagnetic Dy platelet with a thickness of $h = 250$ nm was deposited by thermal evaporation in a vacuum chamber. Finally, the samples were covered by a Cr/Au gate that protects the Dy from oxidation and could be used to tune the electron density.

The experiments were carried out at an electron temperature of $T \approx 100$ mK in a dilution refrigerator, equipped with a 12 T superconducting magnet. The sample holder had a rotatable stage such that the sample could be oriented with respect to the magnetic field by rotation about the y axis. The Dy film was magnetized by applying an in-plane magnetic field $B_{\parallel}$ in the transport (x) direction. The 2DEG responds predominantly to the perpendicular magnetic field $B_z(x)$ via the Lorentz force. Effects due to in-plane magnetic fields and to spin splitting were much weaker and are neglected in the following. The perpendicular magnetic field in the plane of the 2DEG close to $x = 0$ in the configuration shown in Figs. 1(a) and 1(b) is
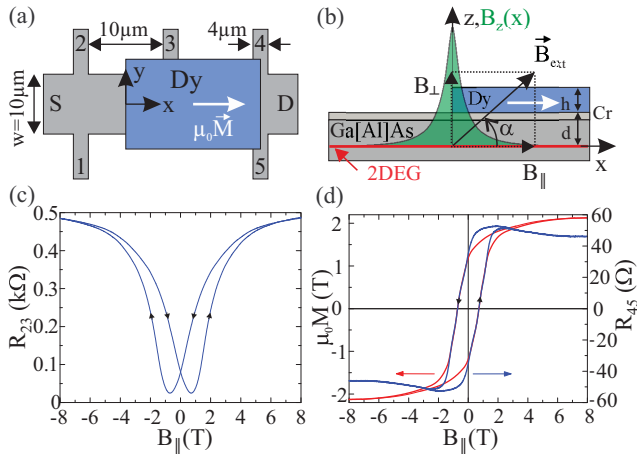
---
[*]mihai.cerchez@hhu.de

FIG. 1. (a) Top-view scheme of the sample layout. The Dy film is magnetized in the transport direction, creating a localized magnetic field profile under the edges. The homogeneous Cr/Au gate that covers the whole structure is not shown. (b) Sketch of the sample orientation with respect to the magnetic field $\vec{B}_{ext}$ generated by the superconducting magnet. (c) Longitudinal resistance of the magnetic barrier as a function of $B_\parallel$ for parallel alignment of the sample. Arrows indicate the sweep direction. (d) The barrier's Hall resistance (blue) and the extracted magnetization trace of the Dy film (red).

given by [15]

$$B_z(x, B_x) = B_\perp - \frac{\mu_0 M(B_x)}{4\pi} \ln\left[\frac{x^2 + d^2}{x^2 + (d+h)^2}\right], \quad (1)$$

where $B_\perp$ denotes the homogeneous component that was tuned by rotating the sample. The second term originates from the fringe field generated by the Dy platelet. This structure is usually denoted as *magnetic barrier* and has an approximately Lorentzian shape with a full width at half maximum of $2\sqrt{d(d+h)}$, which amounted to 420 nm for sample A and 350 nm for sample B. At our maximum Dy magnetization of $\mu_0 M_s = 2.1$ T (see below), its peak reaches values as high as 370 mT for sample A and 440 mT for sample B, respectively. Consequently, magnetic field gradients of the order of 2×10^6 Tm^{-1} can be generated by magnetic barriers in 2DEGs. Offsetting the magnetic barrier by applying $B_\perp$ of opposite sign thus forces the electrons on snake trajectories, oriented in the y direction along the roots of $B_z(x, B_x)$. This concept is used in the following to generate and tune snake trajectories. As shown in Fig. 1(a), one edge of the Dy platelet resides in between contacts 2 and 3. This allows studies of the longitudinal magnetoresistance R_{xx} produced by the corresponding magnetic texture. The opposite edge is located inside contacts 4 and 5 in order to measure the Hall voltage generated by the magnetic barrier and thereby to determine the magnetization of the Dy film.

Rotating the sample about the y axis by small angles $\alpha \leqslant 3°$ with respect to the parallel configuration, in a magnetic field of 10 T, allows the saturation magnetization to remain in the x-y plane to a very good approximation (99.8%), while $B_\perp$ with strengths up to the order of the magnetic barrier amplitude can be added [39]. A scheme of the rotated sample is shown in Fig. 1(b).

An ac current of 50 nA amplitude and with a frequency of 37 Hz is maintained through the sample. The Dy film and the magnetic barrier are characterized by resistance measurements in applied parallel magnetic fields; see Fig. 1(c). The longitudinal magnetoresistance R_{23} shows the typical hysteretic $B_\parallel$ dependence of magnetic barriers [14,15]. In our sample, the relative increase of the magnetic barrier resistance of more than a factor of 20 is quite large, which can be traced back to the small rate of elastic scattering that promotes transmission through the barrier [18]. The large ballisticity of our samples is also reflected in the Hall resistance $R_{45}(B_\parallel)$, which shows a characteristic maximum at intermediate magnetic fields ($B_\parallel = 2.2$ T for the up-sweep). It has been shown recently that this structure is due to a ballistic focusing effect, but the Hall voltage may nevertheless be used to determine the Dy film magnetization [40,41], which for our samples gives the magnetization trace shown in Fig. 1(d). It saturates for $B_\parallel \geqslant 7$ T at a value of $\mu_0 M_s = 2.1$ T. Furthermore, we have studied the Hall resistance as a function of α up to $\alpha = 3°$ and confirmed that the homogeneous perpendicular component $B_\perp$ in this interval is a simple superposition to the magnetic barrier field, in agreement with findings reported earlier [39].

III. RESULTS AND DISCUSSIONS

In order to study the effects of $B_\perp$, the external magnetic field is set to $B_{ext} = 10$ T and R_{23} is measured as a function of the rotation angle α. The Hall voltage between probes 1 and 2 was simultaneously recorded and was used to determine $B_\perp$. The results are shown in Fig. 2, where $R_{23}(B_\perp)$ is plotted for both samples and as a function of the electron density. In sample A [Fig. 2(a)], up to three resistance peaks are observed on top of a smoothly varying background in the interval where $B_\perp$ is antiparallel to the magnetic barrier ($\alpha < 0$ in Fig. 1) but of smaller amplitude. The peak positions shift slightly towards more negative values of $B_\perp$ as n is increased, while their amplitude is most pronounced for slightly negative gate voltages, around electron densities of 2.4×10^{15} m^{-2}. Furthermore, the amplitude tends to decrease as $B_\perp$ becomes more negative. We note that the tuning range of n is quite limited, a well-known problem in high-mobility heterostructures which has been traced back to hysteresis effects [42]. In addition, one resistance peak is observed in the interval where $B_\perp$ and the magnetic barrier are coparallel (for positive values of $B_\perp$). Similar features are observed in sample B, where the background resistance has a different shape, while the peak at coparallel alignment is absent. A corresponding experiment in the quasidiffusive regime where the mean free path was smaller than w has been carried out by Hugger *et al.* [39]. In that experiment, a magnetoresistance with a similar smooth variation was observed and could be explained by competing contributions of snake and cycloid orbits in the y direction, in combination with $\vec{E} \times \vec{B}$ drifts at the sample edges. However, the periodic oscillations reported in this work were absent in that experiment. The appearance of these oscillations in the range of $B_\perp$ where $B_z(x)$ changes its sign suggests that they may be related to electron transport along snake trajectories, which are oriented in the y direction, along the roots of $B_z(x)$.

We proceed by interpreting the origin of the oscillations with guidance from numerical simulations. Semiclassical
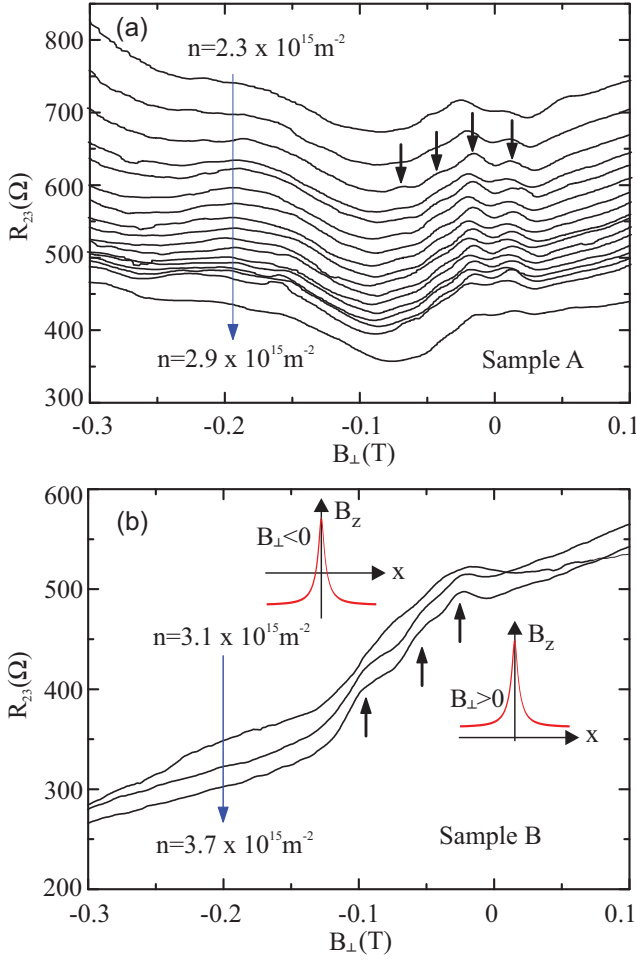
FIG. 2. $R_{23}(B_\perp)$ for samples (a) A and (b) B for different electron densities, with the Dy film at saturation magnetization. The insets in (b) sketch $B_z(x)$ (red) for positive and negative $B_\perp$.

simulations are carried out within the Landauer-Büttiker formalism [43], in the ballistic limit [44]. Electrons are treated as point particles and injected at the Fermi energy in a four-probe geometry with parameters identical to those of sample B, and the magnetoresistance components are calculated as described in detail elsewhere [39]. In Fig. 3, the results of the simulation (trace b) are compared to the experimental trace. Five magnetoresistance peaks are found for the antiparallel alignment of the magnetic barrier and $B_\perp$, and an additional peak is observed for the coparallel alignment very close to $B_\perp = 0$. The positions of peaks 1 to 3 agree reasonably well with the measurements, while peaks 4 and 5 are not observed experimentally. This is due to the effect of scattering which is absent in simulations. For $B_\perp < -0.2$ T, no further oscillations appear and a smooth, almost constant magnetoresistance is found.

These simulations show that the oscillations have a classical character. By inspection of the calculated trajectories, it is conceptually possible to find characteristic orbits that move along the y direction at the magnetoresistance maxima for $B_\perp < 0$. If $B_z(x)$ has no sign change and the magnetic barrier is closed, electrons in the bulk are reflected, but transmission is still possible by $\vec{E} \times \vec{B}$ drifts at the Hall bar edges. As was
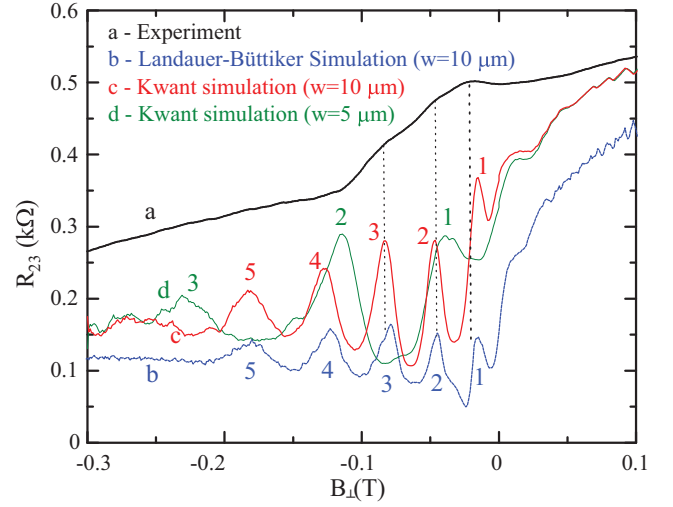

FIG. 3. Experimental data from sample B in comparison with the semiclassical and the quantum simulations, for the electron density $n = 3.5 \times 10^{15}$ m^{-2}. The dotted lines indicate the position of the oscillations that are visible in the experimental curve (corresponding to peaks 1, 2, and 3).

already shown in Ref. [39], by superimposing $B_\perp$ with opposite orientation to the magnetic barrier, two lines of zero field along the y direction are generated, and the $\vec{E} \times \vec{B}$ drift at one edge changes sign, thereby suppressing the edge transmission. On the other hand, this structure can enable a guided transfer of electrons from one Hall bar edge to the other, where they either pass the barrier or are reflected, depending on the exact position and angle at which the electrons hit the edge.

To understand the relevance of this interplay for the oscillatory behavior, one needs either to look at classical trajectories from a statistical point of view in the classical picture or calculate the local density of states (LDOS) in the barrier region within a quantum mechanical treatment which, for sufficiently many occupied states, should be interpretable in terms of classical trajectories.

In the following, we opt for the second possibility and show that the oscillations can be interpreted in a straightforward way with the help of the local density of states. We use the KWANT package [45] for the implementation of the quantum simulations, where again the geometry (with slight modifications for the contacts) and parameters of sample B form the starting point [46]. Electron waves enter the Hall bar via the leads formed by contacts S, 1, and 2 in Fig. 1(a). The tight-binding model is used to calculate the electronic wave functions inside the Hall bar, the resulting local density of states (LDOS), as well as the longitudinal resistance R_{23}. The results (trace c in Fig. 3) agree well with those of the classical simulations, thereby supporting the view that quantum aspects are of minor relevance. The oscillation amplitude in the quantum simulation is larger compared to the classical one, which is most likely due to elastic scattering which is included in the Landauer-Büttiker model, but not in the quantum simulation. In Fig. 4, the local density of states is shown for the states that are occupied by electron injection from contacts S, 1, and 2 for selected values of $B_\perp$. For $B_\perp = -48$ mT [Fig. 4(a)], R_{23} is at the maximum
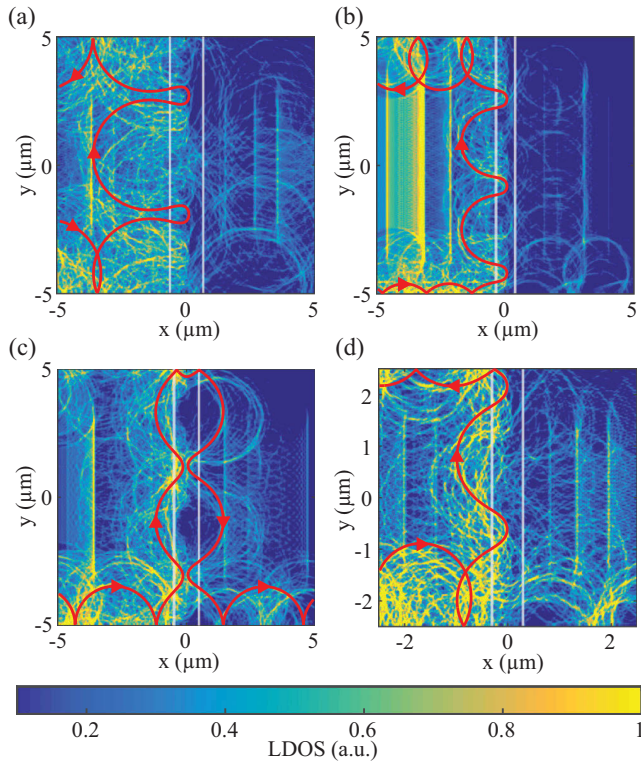
FIG. 4. Local density of states at the maxima of resistance peaks (a) 2 and (b) 3 as well as at the minimum in between (c) for the experimentally implemented structure with a Hall bar width of 10 μm, and (d) for the maximum of resistance peak 2 in a 5-μm-wide Hall bar. In each case, the electron motion is exemplified by a corresponding classical trajectory (red lines with arrows). Also, the zero lines of the perpendicular magnetic field $B - z(x)$ are denoted by the semitransparent gray lines.

of peak 2. Since this magnetic field is chosen to point in the $-z$ direction, the electrons move towards the magnetic barrier preferably via the lower edge of the Hall bar due to $\vec{E} \times \vec{B}$ drift, are reflected at the barrier with a large probability, and move towards contact 2 along the upper Hall bar edge. Close to the magnetic barrier, the LDOS develops a localized shape which we interpret as the superposition of electronic waves that form snake trajectories.

For an illustration of this interpretation, a calculated classical representative trajectory is superimposed to the LDOS. In this picture, the electrons leave the lower sample edge within one cyclotron radius from the magnetic barrier, but still some distance away from the root of the magnetic profile. They move in the $+y$ direction via snake trajectories that are quasicommensurate with the width of the Hall bar, i.e., their period is approximately $w/2$ in this particular case. Due to this commensurability, the electrons hit the upper edge also at a relatively large distance from the magnetic barrier to its left side, which ensures backscattering towards lead 2.

This pattern reappears qualitatively at the peak of oscillation 3 [$B_\perp = -85$ mT, Fig. 4(b)]. Here, the snake trajectory shows a period of $w/3$. The LDOS for $B_\perp = -65$ mT, at the resistance minimum between peaks 2 and 3, is shown in Fig. 4(c). Again, a snake trajectory along the magnetic barrier is visible, but it is incommensurate with w. The small LDOS at the upper

left edge of the Hall bar and the increased one at the lower right edge agree with the reduced backscattering and the increased transmission. Here, the fact that approximately 2.5 snake-trajectory periods fit in the Hall bar ensures that many electrons occupying the snake trajectories hit the upper Hall bar in the interval where $B_z > 0$, and they therefore cross the magnetic barrier. We have also calculated the magnetoresistance for the same magnetic structure in a Hall bar with smaller width of $w = 5$ μm (trace d in Fig. 3). Within the commensurability picture, resistance peak 2 (Fig. 3) is attributed to approximately two snake periods across the Hall bar. This oscillation is thus shifted to a more negative value of $B_\perp$, i.e., to -115 mT. The corresponding LDOS at this peak position is reproduced in Fig. 4(d), where again quasicommensurate snake orbits can be identified. We emphasize that further trajectories, such as cycloid and incommensurate snake orbits, do exist for all magnetic fields. However, the LDOS suggests that they contribute with a lower weight to the oscillations. Within this picture, it furthermore becomes apparent why the oscillations disappear for more negative values of $B_\perp$. The zeros of $B_z(x)$ approach the center of the magnetic barrier and finally vanish, together with the snake orbits, as $B_z(x)$ becomes unipolar.

Finally, we comment on the peak observed in the absence of a sign change of $B_z(x)$ at sample A [first marked peak on the right-hand side in Fig. 2(a)]. This peak appears in the simulations very close to $B_\perp = 0$ on top of a strongly increasing background. While it is clear that this peak must have a different character than those due to the snake-orbit electron motion, we could not identify characteristic trajectories. Comparing the quantum simulations for $w = 10$ and 5 μm, we notice that this peak does not change its position. This suggests that it does not originate from a commensurability effect of some orbit across the Hall bar, but may be due to noncommensurate cycloid orbits or related to the sharply changing $\vec{E} \times \vec{B}$ drift at the intersections of the magnetic barrier with the Hall bar edges.

IV. CONCLUSIONS

We have observed commensurability oscillations in two-dimensional electron gases exposed to an inhomogeneous magnetic field in the transport direction, which is translationally invariant in the transverse direction. For magnetic field profiles with two sign changes in series, resistance oscillations are observed as a function of the homogeneous magnetic field component. Based on our simulations, we interpret the resistance oscillations as dominated by snake-orbit enhanced backscattering, an effect which is particularly strong when the snake trajectories are commensurate with the Hall bar in the sense that the Hall bar width is a multiple integer of the snake-trajectory period.

The effect can thus be interpreted in classical terms, in contrast to the resonances in a magnetic field profile with a single sign change. The observation is based on electrons that cross the Hall bar ballistically in the transverse direction. Therefore, the conditions for the width of the Hall bar are quite stringent, since on the other hand in the implementation presented here, the period of the snake orbit cannot be made much smaller than about 2 μm due to the available magnetic barrier amplitudes. A comparison of the simulated amplitudes to the experimental

ones also suggests that unknown imperfections, such as inhomogeneities of the magnetic barrier or additional diffusive scattering at the edge of the Hall bar, have some influence on the visibility of these commensurability oscillations.

[1] A. Nogaret, J. Phys. Condens. Matter **22**, 253201 (2010).

[2] P. D. Ye, D. Weiss, R. R. Gerhardts, M. Seeger, K. von Klitzing, K. Eberl, and H. Nickel, Phys. Rev. Lett. **74**, 3013 (1995).

[3] H. A. Carmona, A. K. Geim, A. Nogaret, P. C. Main, T. J. Foster, M. Henini, S. P. Beaumont, and M. G. Blamire, Phys. Rev. Lett. **74**, 3009 (1995).

[4] A. Nogaret, S. Carlton, B. L. Gallagher, P. C. Main, M. Henini, R. Wirtz, R. Newbury, M. A. Howson, and S. P. Beaumont, Phys. Rev. B **55**, R16037(R) (1997).

[5] J. Schluck, S. Fasbender, T. Heinzel, K. Pierz, H. W. Schumacher, D. Kazazis, and U. Gennser, Phys. Rev. B **91**, 195303 (2015).

[6] A. Nogaret, D. N. Lawton, D. K. Maude, J. C. Portal, and M. Henini, Phys. Rev. B **67**, 165317 (2003).

[7] A. Nogaret, S. J. Bending, and M. Henini, Phys. Rev. Lett. **84**, 2231 (2000).

[8] A. Nogaret, F. Nasirpouri, J.-C. Portal, H. E. Beere, D. A. Ritchie, A. T. Hindmarch, and C. H. Marrows, Europhys. Lett. **94**, 28001 (2011).

[9] M. Hara, A. Endo, S. Katsumoto, and Y. Iye, Phys. Rev. B **69**, 153304 (2004).

[10] F. M. Peeters and A. Matulis, Phys. Rev. B **48**, 15166 (1993).

[11] A. Matulis, F. M. Peeters, and P. Vasilopoulos, Phys. Rev. Lett. **72**, 1518 (1994).

[12] F. G. Monzon, M. Johnson, and M. L. Roukes, Appl. Phys. Lett. **71**, 3087 (1997).

[13] M. Johnson, B. R. Bennett, M. J. Yang, M. M. Miller, and B. V. Shanabrook, Appl. Phys. Lett. **71**, 974 (1997).

[14] V. Kubrak, A. Neumann, B. L. Gallagher, P. C. Main, M. Henini, C. H. Marrows, and B. J. Hickey, J. Appl. Phys. **87**, 5986 (2000).

[15] T. Vančura, T. Ihn, S. Broderick, K. Ensslin, W. Wegscheider, and M. Bichler, Phys. Rev. B **62**, 5074 (2000).

[16] B. L. Gallagher, V. Kubrak, A. W. Rushforth, A. C. Neumann, K. W. Edmonds, P. C. Main, M. Henini, C. H. Marrows, B. J. Hickey, and S. Thoms, Physica E (Amsterdam) **11**, 171 (2001).

[17] V. Kubrak, K. W. Edmonds, A. C. Neumann, B. L. Gallagher, P. C. Main, M. Henini, C. H. Marrows, B. J. Hickey, and S. Thoms, IEEE Trans. Magn. **37**, 1992 (2001).

[18] M. Cerchez, S. Hugger, T. Heinzel, and N. Schulz, Phys. Rev. B **75**, 035341 (2007).

[19] A. Tarasov, S. Hugger, H. Xu, M. Cerchez, T. Heinzel, I. V. Zozoulenko, U. Gasser-Szerer, D. Reuter, and A. D. Wieck, Phys. Rev. Lett. **104**, 186801 (2010).

[20] J. Reijniers, A. Matulis, K. Chang, F. M. Peeters, and P. Vasilopoulos, Europhys. Lett. **59**, 749 (2002).

[21] H. Xu, T. Heinzel, M. Evaldsson, S. Ihnatsenka, and I. V. Zozoulenko, Phys. Rev. B **75**, 205301 (2007).

[22] B. Schüler, M. Cerchez, H. Xu, J. Schluck, T. Heinzel, D. Reuter, and A. D. Wieck, Phys. Rev. B **90**, 201111(R) (2014).

[23] A. K. Geim, I. V. Grigorieva, S. V. Dubonos, J. G. S. Lok, J. C. Maan, A. E. Filippov, and F. M. Peeters, Nature (London) **390**, 259 (1997).

[24] A. K. Geim, S. V. Dubonos, J. G. S. Lok, I. V. Grigorieva, J. C. Maan, L. T. Hansen, and P. E. Lindelof, Appl. Phys. Lett. **71**, 2379 (1997).

[25] F. M. Peeters and X. Q. Li, Appl. Phys. Lett. **72**, 572 (1998).

[26] S. Pedersen, G. R. Kofod, J. C. Hollingbery, C. B. Sørensen, and P. E. Lindelof, Phys. Rev. B **64**, 104522 (2001).

[27] K. S. Novoselov, A. K. Geim, S. V. Dubonos, Y. G. Cornelissens, F. M. Peeters, and J. C. Maan, Phys. Rev. B **65**, 233312 (2002).

[28] K. S. Novoselov, A. K. Geim, S. V. Dubonos, E. W. Hill, and I. V. Grigorieva, Nature (London) **426**, 812 (2003).

[29] G. Mihailovic, A. Hoffmann, and S. von Molnar, J. Appl. Phys. **106**, 074518 (2009).

[30] A. Majumdar, Phys. Rev. B **54**, 11911 (1996).

[31] Y. Guo, B.-L. Gu, Z. Zeng, J.-Z. Yu, and Y. Kawazoe, Phys. Rev. B **62**, 2635 (2000).

[32] G. Papp and F. M. Peeters, Appl. Phys. Lett. **78**, 2184 (2001).

[33] G. Papp and F. M. Peeters, Appl. Phys. Lett. **79**, 3198 (2001).

[34] H. Z. Xu and Y. Okada, Appl. Phys. Lett. **79**, 3119 (2001).

[35] F. Zhai and H. Q. Xu, Appl. Phys. Lett. **88**, 032502 (2006).

[36] M. Pioro-Ladriére, T. Obata, Y. Tokura, Y.-S. Shin, T. Kubo, K. Yoshida, T. Taniyama, and S. Tarucha, Nat. Phys. **4**, 776 (2008).

[37] K. C. Nowack, F. H. L. Koppens, Y. V. Nazarov, and L. M. K. Vandersypen, Science **318**, 1430 (2007).

[38] E. Kawakami, P. Scarlino, D. R. Ward, F. R. Braakman, D. E. Savage, M. G. Lagally, M. Friesen, S. N. Coppersmith, M. A. Eriksson, and L. M. K. Vandersypen, Nat. Nano **9**, 666 (2014).

[39] S. Hugger, M. Cerchez, H. Xu, and T. Heinzel, Phys. Rev. B **76**, 195308 (2007).

[40] S. Fasbender, J. Schluck, M. Cerchez, T. Heinzel, S. Sievers, K. Pierz, and H. W. Schumacher, J. Appl. Phys. **119**, 094302 (2016).

[41] M. Cerchez and T. Heinzel, Appl. Phys. Lett. **98**, 232111 (2011).

[42] C. Rüssler, T. Feil, P. Mensch, T. Ihn, K. Ensslin, D. Schuh, and W. Wegscheider, New J. Phys. **12**, 043007 (2010).

[43] M. Büttiker, Phys. Rev. Lett. **57**, 1761 (1986).

[44] C. W. J. Beenakker, Phys. Rev. Lett. **62**, 2020 (1989).

[45] C. W. Groth, M. Wimmer, A. R. Akhmerov, and X. Waintal, New J. Phys. **16**, 063065 (2014).

[46] H. U. Baranger and A. D. Stone, Phys. Rev. Lett. **63**, 414 (1989).

Quantum signatures of competing electron trajectories in antidot superlattices

J. Schluck* and T. Heinzel

Condensed Matter Physics Laboratory, Heinrich-Heine-Universität, D-40204 Düsseldorf, Germany

J. Feilhauer,† K. Pierz, and H. W. Schumacher

Physikalisch-Technische Bundesanstalt, Bundesallee 100, D-38116 Braunschweig, Germany

D. Kazazis‡ and U. Gennser

Centre de Nanosciences et de Nanotechnologies (C2N), CNRS,
Univ. Paris Sud-Université Paris-Saclay, 91120 Palaiseau, France
(Dated: September 18, 2017)

Magnetotransport measurements on antidot lattices with square and hexagonal geometries are reported. The resistivity shows a superposition of the classical commensurability resonances and Shubnikov-de Haas type oscillations. The latter have two components where one is in phase and the other one ist out of phase with the Hall resistivity. Within the magnetic field range of the commensurability resonances the out of phase component dominates, whereas for increased magnetic fields the conventional in-phase behavior is recovered. This is interpreted with the help of numerical simulations as a quantum signature of the competition between skipping and hopping transport in antidot superlattices.

Reference

J. Schluck, J. Feilhauer, D. Kazazis, U. Gennser, K. Pierz, H.W. Schumacher, and T. Heinzel, submitted to Phys. Rev. B.

Copyright statement

Contributions

I designed the sample and contributed to sample preparation. I conducted the experiments and analyzed the experimental data. I wrote the quantum code based on the Kwant package and performed numerical simulations used for the interpretation of the experimental data. I wrote the main body of the manuscript.

Quantum signatures of competing electron trajectories in antidot superlattices

J. Schluck* and T. Heinzel

Condensed Matter Physics Laboratory, Heinrich-Heine-Universität, D-40204 Düsseldorf, Germany

J. Feilhauer,† K. Pierz, and H. W. Schumacher

Physikalisch-Technische Bundesanstalt, Bundesallee 100, D-38116 Braunschweig, Germany

D. Kazazis‡ and U. Gennser

Centre de Nanosciences et de Nanotechnologies (C2N), CNRS,
Univ. Paris Sud-Université Paris-Saclay, 91120 Palaiseau, France
(Dated: September 18, 2017)

Magnetotransport measurements on antidot lattices with square and hexagonal geometries are reported. The resistivity shows a superposition of the classical commensurability resonances and Shubnikov-de Haas type oscillations. The latter have two components where one is in phase and the other one ist out of phase with the Hall resistivity. Within the magnetic field range of the commensurability resonances the out of phase component dominates, whereas for increased magnetic fields the conventional in-phase behavior is recovered. This is interpreted with the help of numerical simulations as a quantum signature of the competition between skipping and hopping transport in antidot superlattices.

I. INTRODUCTION

Antidot superlattices in two-dimensional electron gases (2DEGs) have been an active field of research since their first implementations. Originally studied mostly in Ga[Al]As-heterostructures[1–3], more recent experiments focused on novel materials like graphene[4,5], topological insulators[6,7] and black phosphorus[8]. In the semiclassical regime, which can be characterized by a lattice constant a significantly larger than the electron Fermi wavelength λ_F but small compared to the mean free path ℓ of the electrons in the absence of the superlattice, the longitudinal magnetoresistivity $\rho_{xx}(B)$ shows prominent commensurability resonances, which demonstrates the inadequacy of the Boltzmann model that predicts ρ_{xx} to be independent of the applied perpendicular magnetic field B. Rather, the dominant scattering takes place at the superlattice potential, and neither the location nor the shape and strength of the scatterers are random. This correlated scattering leads to a mixed phase space for the conduction electrons, where regular and chaotic regions coexist, the relevance of which depends on the experimental parameters.[9,10]

In extension to these classical effects, superimposed quantum oscillations have been observed in several experiments[11–15]. They can be modeled semiclassically using the periodic orbit theory[16,17], but also fully quantum mechanical calculations have been reported[18–21]. In case they are B-periodic, they indicate electronic interferences along trajectories which are commensurate with the superlattice potential but independent of B within a certain magnetic field interval,[11–13,16,17]. 1/B-periodic quantum oscillations, on the other hand, are attributed to Landau quantization where the electron trajectories are cyclotron orbits which remain essentially undisturbed by the weak superlattice potential[15]. The type of periodicity may furthermore depend on the magnetic field. For example, Weiss et al. have reported 1/B-periodicity for magnetic fields where the cyclotron orbit fits in the area in between the antidots, and B-periodicity for smaller magnetic fields.[11] In this way, antidot lattices have also been test systems for the relation between classical trajectories and the quantum properties of the system. The resulting contributions to conductivity are often grouped as being related to either scattering or band transport. In a classical picture, the former describes a hopping between localized states, while the latter is associated with extended states in the antidot lattice that skip along the lines of antidots. The relevance of each contribution depends on the sample parameters and the magnetic field range. An instructive demonstration was reported for rectangular lattices[22–24], where electrons were found to skip along the short lattice direction and hop along the long one.

In the present work we demonstrate experimentally how hopping and skipping transport contribute to the conductivity in square and hexagonal antidot lattices. Our samples are in a regime, where quantum signatures of both transport mechanisms coexist in the magnetoresistance over a wide magnetic field range. We identify the underlying semiclassical dynamics via a comparison to the quantum features visible in the Hall resistance. By this means we are able to deduce a B - dependent relevance of the classical trajectories for transport from tracking the amplitude of their corresponding quantum oscillations. In Section II we present our experimental setup and details on the sample preparation. Our experimental findings are discussed in Section III and interpreted with the help of numerical simulations in Section IV. The paper ends with a conclusion in Section V.

II. SAMPLE PREPARATION AND EXPERIMENTAL SETUP

A $Ga_{0.7}Al_{0.3}As$ heterostructure with a 2DEG formed 90 nm below the surface is used. After infrared illumination the pristine 2DEG has a density of $n = 4.0 \times 10^{15}\,\mathrm{m^{-2}}$ and a mobility of $890\,\mathrm{m^2/Vs}$ at liquid helium temperature, corresponding to a mean free path of $92\,\mu\mathrm{m}$. Antidot lattices with square and hexagonal symmetries are prepared by electron beam lithography and subsequent reactive ion etching. A lattice constant of $a = 750\,\mathrm{nm}$ and a lithographic antidot diameter of $d = 150\,\mathrm{nm}$ is used for both geometries, cf. Fig. 1(c) for atomic force microscope (AFM) images. The depletion zone can be estimated from Aharonov-Bohm like oscillations[25] in strong magnetic fields to be smaller than $50\,\mathrm{nm}$[26]. The resulting aspect ratio d/a thus lies in the range $0.2 < d/a < 0.33$. The lattices extend over $250\,\mu\mathrm{m}$ in length and $100\,\mu\mathrm{m}$ in width, which is also the width of the Hall bar. The spacing between the voltage probes is $150\,\mu\mathrm{m}$. The samples are transferred to a dilution refrigerator with a base temperature of $25\,\mathrm{mK}$ and an electron temperature estimated to be $0.1\,\mathrm{K}$. Measurements at elevated temperatures are performed in a Helium gas flow cryostat with a variable temperature insert. The diagonal and Hall resistance are probed by applying a low frequency ac current and measuring the voltage drop across the Hall bar with a lock-in amplifier.

III. EXPERIMENTAL RESULTS

In Fig. 1 we show the results of the magnetoresistance measurements. For both the square (Fig. 1(a)) and the hexagonal (Fig. 1(b)) lattice a series of pronounced commensurability oscillations (COs) is observed, with the principal peak at a magnetic field around $270\,\mathrm{mT}$. The numbers labeling the resistance maxima in the figure indicate the number of antidots that are encircled at the given magnetic field. Superimposed to this, a short period oscillation emerges at about $100\,\mathrm{mT}$ at $0.1\,\mathrm{K}$. It gets rapidly suppressed as one increases the temperature and has a $1/B$ periodicity. It is straightforward to interpret it as a type of Shubnikov de-Haas(SdH) oscillation. Spin-splitting becomes visible for magnetic fields $B \geq 700\,\mathrm{mT}$ and will therefore be neglected in the following. For some magnetic fields, deviations from the periodicity can be observed. In the hexagonal lattice at $330\,\mathrm{mT}$ and at $300\,\mathrm{mT}$ in the square lattice there appears an additional maximum in the resistance accompanied by a suppression of the amplitude of the neighboring peaks. At lower magnetic fields additional distortions can be seen in both amplitude and periodicity. In Fig. 1(c) the Hall effect for both samples is shown. From the comparison of the classical extrapolation to the data one can see that for low magnetic fields ($B \leq 250\,\mathrm{mT}$) the modification induced by the antidots is negligible. For magnetic fields beyond the principal CO, quantum Hall signatures are found and
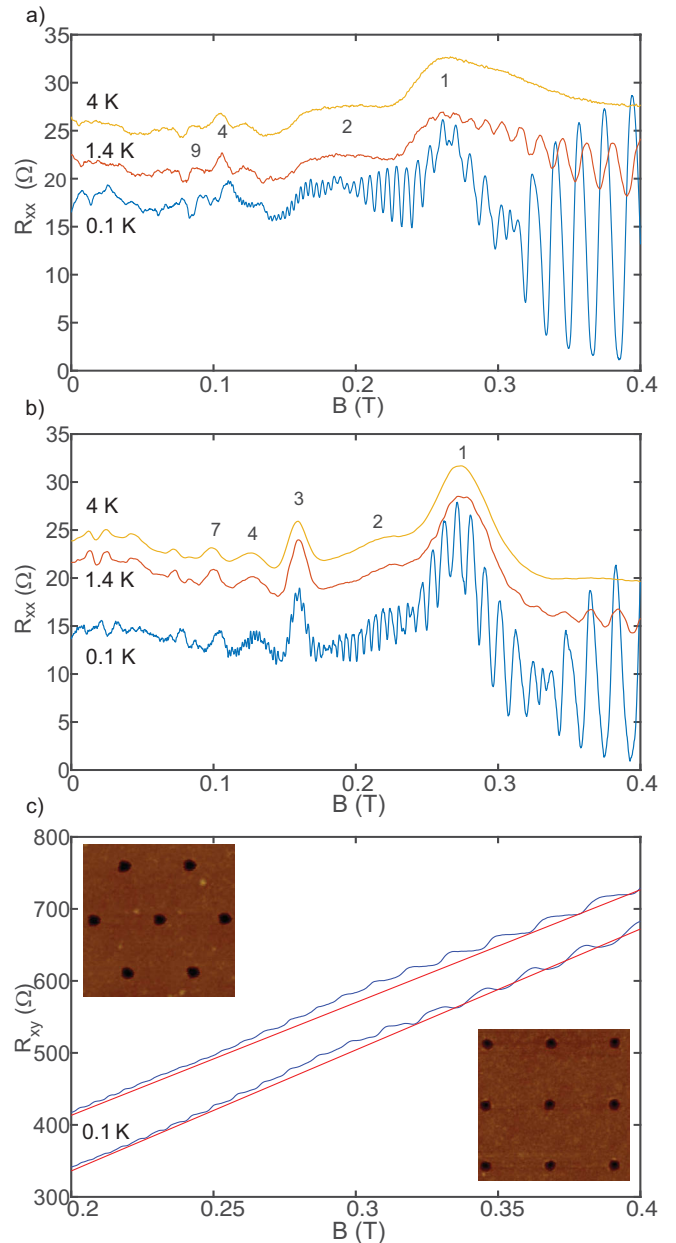

FIG. 1. (color online). (a) $R_{xx}(B)$ of the sample with square symmetry at several temperatures. (b) $R_{xx}(B)$ of the sample with hexagonal symmetry at several temperatures. Numbers label the resistance maxima by the number of antidots encircled at the given magnetic field. The traces at elevated temperatures are vertically offset for clarity. (c) Insets: AFM pictures of the two samples. The lattice constant a is 750 nm in both cases. Main figure: Hall resistance for both sample types at base temperature. The hexagonal trace is vertically offset by $100\,\Omega$ for clarity. The classical extrapolation is shown in red.

the average slope of the data coincides with the classical extrapolation. In the magnetic field range of the principal CO however, the Hall resistance is increased with respect to the classical extrapolation, although plateaus

are already formed.

We proceed by studying the interplay of diagonal and Hall resistance. For pristine 2DEGs the maxima in the SdH oscillations coincide with the transitions between quantum Hall plateaus. This can be understood in terms of the formation of extended states throughout the sample. To check this connection in our system, we numerically take the derivative of the Hall resistance with respect to the magnetic field dR_{xy}/dB and compare it to the diagonal resistance. The result is shown in Fig. 2(a) and Fig. 2(b) for the square and hexagonal lattice, respectively. Here we have plotted the data against the spin-resolved Landau-level filling factor $\nu = hn/eB$. In this representation it becomes visible that in fact the superimposed quantum oscillation has a more complex structure. Besides a dominant large amplitude oscillation, there is also a small amplitude oscillation visible (marked by the pink arrows), which is out of phase with the former one. It is more prominent in the case of the square lattice, but also visible in the hexagonal lattice. For a pristine 2DEG one can expect the maxima in R_{xx} and dR_{xy}/dB to occur at odd integers, corresponding to half filled Landau-levels. For magnetic fields beyond the principal CO, this is also what we observe in our samples. Interestingly the situation changes for lower magnetic fields. For filling factors $\nu \geq 50$, the resistance maxima in R_{xx} still coincide with odd filling factors, but the maxima in dR_{xy}/dB can be found at even integers. This oscillation is now in-phase with the small amplitude oscillation observed in R_{xx}.

IV. INTERPRETATION AND NUMERICAL SIMULATIONS

Previously, quantum effects in antidot superlattices were often interpreted semiclassically[16,17]. The framework of periodic orbit theory allows for a calculation of the contributions to the density of states (DOS) stemming from various periodic orbits. From this the periods and occurrences of quantum oscillations were predicted.

In our case such a treatment is not justified. Our sample design leads to a situation, where the potential outside of the antidots is almost constant. Therefore, the previously reported oscillations caused by electron cyclotron motion being strongly modified[11,13], observed for antidot lattices with large d/a ratio, are expected to play only a minor role in our case. The only significant periodic orbits remaining are the ones where the electron undergoes cyclotron motion undisturbed by the superlattice. The effects observed by us are also unlikely to originate from the Hofstadter butterfly[27–30]. Such effects are periodic in $\phi/\phi_0 = BAe/h$, where A is the size of the unit cell of the superlattice, in contrast to the 1/B-periodicity seen here.

Instead we propose an explanation in terms of the relation between the density of states (DOS) and ρ_{xx}, which can be connected to skipping and hopping transport as
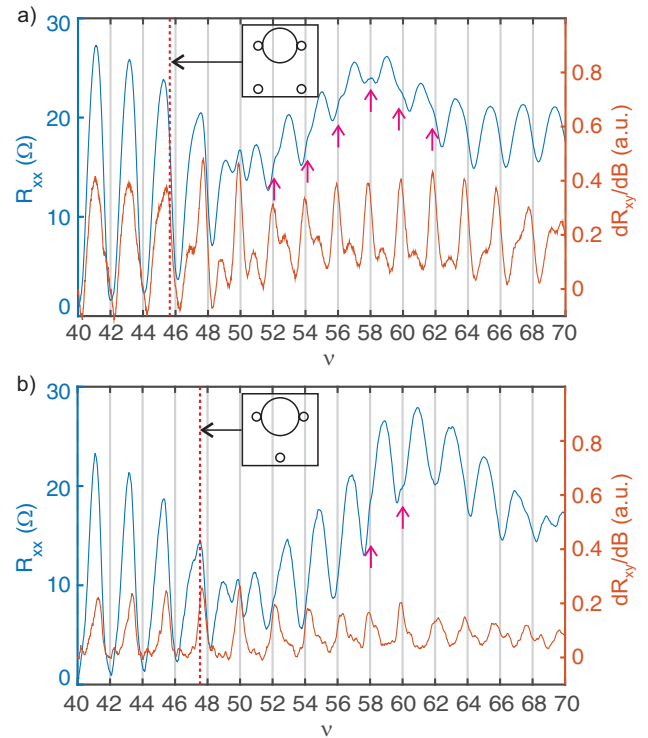

FIG. 2. (color online). Comparison of the diagonal resistance R_{xx} and the derivative of the Hall resistance R_{xy}/dB for the square(a) and hexagonal(b) lattice as a function of the filling factor $\nu = hn/eB$. The dashed lines indicate the magnetic field where the cyclotron circle just fits in between two nearest neighbor antidots (see the insets), thereby marking the limit for skipping transport.

used for a description within a classical picture. We first take a look at the elements of the conductivity tensor. Assuming isotropic transport we have $\sigma_{xx} = \frac{\rho_{xx}}{\rho_{xx}^2 + \rho_{xy}^2}$ and $\sigma_{xy} = \frac{-\rho_{xy}}{\rho_{xx}^2 + \rho_{xy}^2}$. For the whole range of interest $(0.1\,\mathrm{T} < B < 0.5\,\mathrm{T})$, we find the Hall conductivity to be at least one order of magnitude larger than the diagonal one. We can conclude $\sigma_{xx} \approx \rho_{xx}/\rho_{xy}^2$, which implies maxima in resistivity to coincide with maxima in conductivity. This is in contrast to earlier works by Ishizaka et al.[21,31], who reported changes in the interplay of resistivity and DOS over the course of the COs, but in their system $\sigma_{xx} \approx \sigma_{xy}$ and thus the relevant structure was caused by the Hall conductivity.

More relevant to our situation, Schuster et al. studied rectangular antidot lattices[22] and found a magnetic field range, where quantum oscillations were present in ρ_{xx} and ρ_{yy} that were out of phase. Neudert et al. explained this in terms of transport being dominated by skipping along the short period of the lattice and by hopping between bound states along the long period[23]. In this picture the conductance by hopping is enlarged at the maxima in the density of states, where many bound states exist. The electrons then travel along the lattice via a so-called scattering conductivity, i.e. by being scat-

tered from one bound state to another. In contrast to this the skipping along a line of antidots is identified as a band transport mechanism. The associated group velocity and thus also the contribution to conductivity was found to be enhanced for situations where there are few bound states. Intuitively one can consider the skipping orbits to carry current most efficiently when there are no bound states for them to scatter into; therefore their contribution to conductivity is biggest for a low density of states.

To apply these finding to our observations we assume the peaks in the dR_{xy}/dB trace to be indicative of the centers of the Landau levels, i.e. coinciding with maxima in the DOS. As Ishizaka et al. argued[21], skipping orbits do not contribute to the Hall conductivity. Therefore, a change in σ_{xy} must be caused by hopping transport, which is in phase with the DOS. This means that within the principal CO in our sample the Landau level centers are shifted from odd to even integer filling factor values. The assumption of such a level shift is consistent with the shift of the Hall resistance seen in Fig. 1(c). An increase of the energy of the Landau levels causes a relative increase of the Hall resistance compared to the classical extrapolation. This effect was already reported for unidirectional electric[32] and magnetic[33–35] superlattices and it is plausible to occur also in two-dimensional superlattices. In this case we conclude that the dominant contribution to the conductivity, and thus also the resistivity within the principal CO, is caused by band transport, since it is out of phase with the DOS. The low amplitude quantum oscillation which is in phase with the DOS signifies the small but visible contribution of hopping transport to the overall conductivity in this magnetic field range. For stronger magnetic fields ($B \geq 0.35\,T$), hopping dominates the transport and consequently, the transitions in the Hall effect coincide with resistance maxima and odd filling factors again. In a classical picture this corresponds to the magnetic field range where the condition $2R_c < a - d$ is fulfilled, and is readily interpreted as the vanishing of skipping orbits. Electrons can no longer travel along a line of antidots, but are rather bound to closed orbits either around antidots or in the void space between them. Judging from the amplitude of the oscillations, at filling factor 50 the significance of band and hopping transport is equally strong, resulting in the prominent triple peak.

A similar analysis in terms of electron trajectories was done by Schuster et al.[36]. There the authors increased the diameter of the antidots by a top gate and observed a change from band to hopping transport within the classical CO. Lüthi et al.[24] described the influence of both transport mechanisms in terms of trajectories in rectangular lattices. They clearly state the coexistence of pinned and skipping orbits in their lattice, but, in contrast to our findings, each type of orbit only affects either σ_{xx} or σ_{yy}.

To substantiate our interpretation we employ numerical simulations based on the Kwant transport package[37].

Kwant allows for the implementation of finite tight binding scattering regions connected to semi-infinite leads, which models our Hall bar structure connected to voltage probes. It gives access to various transport properties, like the transmission between the contacts, which can be converted to a resistance via the Landauer-Büttiker formalism[38]. We calculate the 4-terminal resistance[39] as well as the DOS of a $6 \times 4.5\,\mu m^2$ scattering region. Larger arrays are beyond the scope of the present work due to technical limitations. A tight-binding lattice constant of $3\,nm$ and Fermi energy corresponding to the density of our 2DEG was used. A square lattice antidot potential is implemented via the on-site potential

$$V(x,y) = V_0 \left(\sin \frac{\pi x}{a} \sin \frac{\pi y}{a} \right)^\beta , \qquad (1)$$

where V_0 is chosen such that the Fermi energy is crossed at the lithographic diameter of the antidots. The steepness parameter is set to $\beta = 16$ reflecting the low value of d/a in our samples. The simulation does not take thermal smearing into account, but its effect is emulated by numerical smoothing of the results. Scattering at residual impurities is included via random on-site disorder. In Fig. 3 the resistance and the DOS are shown as a function of the filling factor in the range of the principal CO. The position of the classical resistance peak around fill-
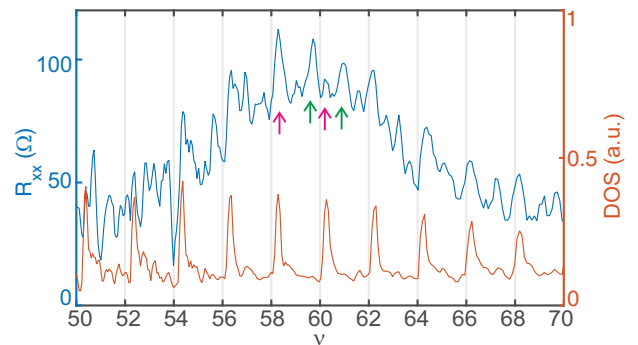

FIG. 3. (color online). Fully quantum mechanical calculation of the magnetoresistance (blue) and the density of states (red) of a square antidot lattice as a function of the filling factor at $T = 0$ based on the Kwant package. Green arrows exemplify resistance maxima that are out of phase with the DOS, while pink arrows point to maxima in phase with it.

ing factor 60 is well reproduced. Additional oscillations with varying amplitudes are superimposed. In the DOS a series of well developed peaks, which are periodic in $1/B$, can be observed. Qualitatively we can observe similar behaviour in the relation between DOS and resistance as in our experiment. The position of the DOS peaks is shifted away from odd filling factors towards even ones over the magnetic field range of the classical peak. Also in the simulation we can see resistance maxima, which are in phase with the DOS (pink arrows) and should therefore be interpreted as being caused by hopping transport. They correspond to the small amplitude quantum oscillation in

our measurements. Furthermore there are peaks in the simulated resistance that occur for minima in the DOS (green arrows) and are thus indicative of band transport. The experimental counterpart of this oscillation is the dominating quantum oscillation within the principal CO in both lattices. To bring measurements and simulation into better agreement, one would have to increase the simulated sample size and include thermal broadening. This is beyond our scope here.

V.   SUMMARY AND CONCLUSIONS

In conclusion we have demonstrated experimentally the coexistence of quantum signatures of hopping and skipping transport in antidot superlattices with low aspect ratio within one resistivity component. Within the principal commensurability resonance, skipping transport dominates the resistivity as is indicated by a superimposed quantum oscillation which is out of phase with the density of states. As the magnetic field is increased, the behavior of a pristine 2DEG is gradually recovered, implying the dominance of hopping transport. Also a shift of the Landau levels from odd to even integer filling factors is observed in this range in accordance with earlier observations in unidirectional superlattices[32–35]. For stronger magnetic fields, the transition to hopping dominated transport is seen and the behavior of a conventional pristine 2DEG is recovered. Our findings are in qualitative agreement with tight-binding calculations. The results show that the dominating transport mechanism can be determined experimentally from a comparison of the quantum effects visible in diagonal and Hall resistivity. The small d/a ratio corresponds to an approximately constant potential in between the antidots. The resulting 1/B-periodicity of the quantum oscillations allows a straightforward interpretation of the oscillatory structures. This way, the classical commensurability resonances and the superimposed quantum oscillations are intimately related.

ACKNOWLEDGEMENT

* jakob.schluck@hhu.de
† Present Address: Institute of Electrical Engineering, Slovak Academy of Sciences, 841 04 Bratislava, Slovakia
‡ Present Address: Paul Scherrer Institut, Villigen-PSI, 5232, Switzerland

[1] D. Weiss, M. L. Roukes, A. Menschig, P. Grambow, K. von Klitzing, and G. Weimann, Phys. Rev. Lett. **66**, 2790 (1991).

[2] K. Ensslin and P. M. Petroff, Phys. Rev. B **41**, 12307 (1990).

[3] A. Lorke, J. P. Kotthaus, and K. Ploog, Phys. Rev. B **44**, 3447 (1991).

[4] R. Yagi, R. Sakakibara, R. Ebisuoka, J. Onishi, K. Watanabe, T. Taniguchi, and Y. Iye, Phys. Rev. B **92**, 195406 (2015).

[5] A. Sandner, T. Preis, C. Schell, P. Giudici, K. Watanabe, T. Taniguchi, D. Weiss, and J. Eroms, Nano Letters **15**, 8402 (2015).

[6] M. Song, J.-H. Chu, J. Zhou, S. Tongay, K. Liu, J. Suh, H. Chen, J. S. Kang, X. Zou, and L. You, Nanotechnology **26**, 265301 (2015).

[7] H. Maier, J. Ziegler, R. Fischer, D. Kozlov, Z. D. Kvon, N. Mikhailov, S. A. Dvoretsky, and D. Weiss, ArXiv e-prints (2017), arXiv:1708.07766 [cond-mat.mes-hall].

[8] A. Cupo, P. Masih Das, C.-C. Chien, G. Danda, N. Kharche, D. Tristant, M. Drndi, and V. Meunier, ACS Nano **11**, 7494 (2017).

[9] R. Fleischmann, T. Geisel, and R. Ketzmerick, Phys. Rev. Lett. **68**, 1367 (1992).

[10] R. Fleischmann, T. Geisel, and R. Ketzmerick, Europhys. Lett. **25**, 219 (1994).

[11] D. Weiss, K. Richter, A. Menschig, R. Bergmann, H. Schweizer, K. von Klitzing, and G. Weimann, Phys. Rev. Lett. **70**, 4118 (1993).

[12] R. Schuster, K. Ensslin, D. Wharam, S. Kühn, J. P. Kotthaus, G. Böhm, W. Klein, G. Tränkle, and G. Weimann, Phys. Rev. B **49**, 8510 (R) (1994).

[13] F. Nihey, S. W. Hwang, and K. Nakamura, Phys. Rev. B **51**, 4649 (1995).

[14] Y. Iye, M. Ueki, A. Endo, and S. Katsumoto, J. Phys. Soc. Japan **73**, 3370 (2004).

[15] Y. Kato, A. Endo, S. Katsumoto, and Y. Iye, Phys. Rev. B **86**, 235315 (2012).

[16] K. Richter, Europhys. Lett. **29**, 7 (1995).

[17] G. Hackenbroich and F. van Oppen, Europhys. Lett. **29**, 151 (1995).

[18] D. Pfannkuche and R. R. Gerhardts, Phys. Rev. B **46**, 12606 (1992).

[19] R. B. S. Oakeshott and A. MacKinnon, Journal of Physics: Condensed Matter **6**, 1519 (1994).

[20] H. Silberbauer and U. Rössler, Phys. Rev. B **50**, 11911 (1994).

[21] S. Ishizaka, F. Nihey, K. Nakamura, J. Sone, and T. Ando, Phys. Rev. B **51**, 9881 (1995).

[22] R. Schuster, K. Ensslin, J. P. Kotthaus, G. Böhm, and W. Klein, Phys. Rev. B **55**, 2237 (1997).

[23] R. Neudert, P. Rotter, U. Rössler, and M. Suhrke, Phys. Rev. B **55**, 2242 (1997).

[24] S. Lüthi, T. Vancura, K. Ensslin, R. Schuster, G. Böhm, and W. Klein, Phys. Rev. B **55**, 13088 (1997).

[25] Y. Aharonov and D. Bohm, Phys. Rev. **115**, 485 (1959).

[26] J. Schluck, S. Fasbender, T. Heinzel, K. Pierz, H. W. Schumacher, D. Kazazis, and U. Gennser, Phys. Rev. B **91**, 195303 (2015).

[27] D. Hofstadter, Phys. Rev. B **14**, 2239 (1976).

[28] F. H. Claro and G. H. Wannier, Phys. Rev. B **19**, 6068 (1979).

[29] T. Schlösser, K. Ensslin, J. P. Kotthaus, and M. Holland, Europhys. Lett. **33**, 683 (1996).

[30] M. C. Geisler, J. H. Smet, V. Umansky, K. von Klitzing, B. Naundorf, R. Ketzmerick, and H. Schweizer, Phys. Rev. Lett. **92**, 256801 (2004).

[31] S. Ishizaka and T. Ando, Phys. Rev. B **56**, 15195 (1997).

[32] M. Tormow, D. Weiss, A. Manolescu, R. Menne, K. v. Klitzing, and G. Weimann, Phys. Rev. B **54**, 16397 (1996).

[33] K. W. Edmonds, B. L. Gallagher, P. C. Main, N. Overend, R. Wirtz, A. Nogaret, M. Henini, C. H. Marrows, B. J. Hickey, and S. Thoms, Phys. Rev. B **64**, 041303 (2001).

[34] J. Shi, F. M. Peeters, K. W. Edmonds, and B. L. Gallagher, Phys. Rev. B **66**, 035328 (2002).

[35] A. Endo and Y. Iye, Journal of the Physical Society of Japan **77**, 054709 (2008).

[36] R. Schuster, G. Ernst, K. Ensslin, M. Entin, M. Holland, G. Böhm, and W. Klein, Phys. Rev. B **50**, 8090 (1994).

[37] C. W. Groth, M. Wimmer, A. R. Akhmerov, and X. Waintal, New Journal of Physics **16**, 063065 (2014).

[38] M. Büttiker, Phys. Rev. Lett. **57**, 1761 (1986).

[39] H. U. Baranger and A. D. Stone, Phys. Rev. B **40**, 8169 (1989).

Commensurability resonances in two-dimensional magnetoelectric lateral superlattices

J. Schluck, S. Fasbender, and T. Heinzel[*]

Condensed Matter Physics Laboratory, Heinrich-Heine-Universität, D-40225 Düsseldorf, Germany

K. Pierz and H. W. Schumacher

Physikalisch-Technische Bundesanstalt, Bundesallee 100, D-38116 Braunschweig, Germany

D. Kazazis and U. Gennser

CNRS-LPN, Route de Nozay, 91960 Marcoussis, France

(Received 16 December 2014; revised manuscript received 23 February 2015; published 6 May 2015)

Hybrid lateral superlattices composed of a square array of antidots and a periodic one-dimensional magnetic modulation are prepared in Ga[Al]As heterostructures. The two-dimensional electron gases exposed to these superlattices are characterized by magnetotransport experiments in vanishing average perpendicular magnetic fields. Despite the absence of closed orbits, the diagonal magnetoresistivity in the direction perpendicular to the magnetic modulation shows pronounced classical resonances. They are located at magnetic fields where snake trajectories exist which are quasicommensurate with the antidot lattice. The diagonal magnetoresistivity in the direction of the magnetic modulation increases sharply above a threshold magnetic field and shows no fine structure. The experimental results are interpreted with the help of numerical simulations based on the semiclassical Kubo model.

Reference

J. Schluck, S. Fasbender, T. Heinzel, K. Pierz, H. W. Schumacher, D. Kazazis, and U. Gennser, Phys. Rev. B 91, 195303 (2015), ©2015 American Physical Society

Copyright statement

Contributions

I designed the sample and contributed to sample preparation. I participated in the conduction of the experiments and the analysis of the experimental data. I rewrote the existing classical Kubo-code and performed numerical simulations used for the interpretation of the experimental data. I contributed to manuscript writing.

Commensurability resonances in two-dimensional magnetoelectric lateral superlattices

J. Schluck, S. Fasbender, and T. Heinzel[*]

Condensed Matter Physics Laboratory, Heinrich-Heine-Universität, D-40225 Düsseldorf, Germany

K. Pierz and H. W. Schumacher

Physikalisch-Technische Bundesanstalt, Bundesallee 100, D-38116 Braunschweig, Germany

D. Kazazis and U. Gennser

CNRS-LPN, Route de Nozay, 91960 Marcoussis, France

Hybrid lateral superlattices composed of a square array of antidots and a periodic one-dimensional magnetic modulation are prepared in Ga[Al]As heterostructures. The two-dimensional electron gases exposed to these superlattices are characterized by magnetotransport experiments in vanishing average perpendicular magnetic fields. Despite the absence of closed orbits, the diagonal magnetoresistivity in the direction perpendicular to the magnetic modulation shows pronounced classical resonances. They are located at magnetic fields where snake trajectories exist which are quasicommensurate with the antidot lattice. The diagonal magnetoresistivity in the direction of the magnetic modulation increases sharply above a threshold magnetic field and shows no fine structure. The experimental results are interpreted with the help of numerical simulations based on the semiclassical Kubo model.

　　　　　　PACS number(s): 73.23.−b, 73.63.−b

I. INTRODUCTION

Artificial lateral superlattices (LSLs) in two-dimensional electron gases (2DEGs) [1–5] are of great interest for fundamental studies of the electron dynamics in periodic potentials. Since it is very common that the artificial lattice constants place the systems in the transition region between the quantum and the classical regime, classical, semiclassical, as well as quantum descriptions are all justifiable and enable studies of the validity of these approaches including their limits. Besides the Fermi wavelength λ_F and the electronic coherence length, the elastic mean-free path is an important parameter as well, since it defines the length scale below which interaction with the LSL potential dominates over random scattering. Many different variants of LSLs have been investigated in great depth. One-dimensional electrostatic [1,2] and magnetic [6–8] lattices, where the modulation extends along one spatial coordinate and the structure is homogeneous along the second one, show magnetoresistivity resonances that can be explained in terms of guiding center drift resonances of the cyclotron motion within a classical picture [9] or by miniband formation in a quantum picture [2,10,11]. One-dimensional magnetoelectric hybrid LSLs have been studied in some experiments as well, where the strain imposed by the ferromagnetic or superconductive electrodes used to define the magnetic LSL also generates an electrostatic superlattice [12]. Two-dimensional LSLs, both magnetic [7,13] and electrostatic [3–5], have been studied thoroughly as well. Their classical dynamics corresponds to a mixed phase space where chaotic and regular dynamics coexist [14,15] and causes commensurability resonances that are characteristic for the type of Bravais superlattice employed, such as square [3–5], rectangular [16], or hexagonal [17,18]. Within a quantum picture, on the other hand, a fractal energy

spectrum, also known as the Hofstadter butterfly [19,20], is seen for weak electrostatic modulation amplitudes [21]. B-periodic oscillations on top of commensurability resonances [16,18,22] can be explained within a semiclassical approach by the Aharonov-Bohm [23]—or Altshuler-Aronov-Spivak [24]—effect in terms of quantized motion along closed trajectories defined by the LSL potential and the magnetic field [25].

2DEGs with very high electron mobilities [26,27] have recently been developed into mature systems. They enable the preparation of LSLs with large lattice constants in the classical ballistic regime and facilitate the definition of novel types of LSLs with more complex unit cells. Here, the study of such a hybrid LSL, composed of a a two-dimensional, square antidot lattice and a one-dimensional magnetic array is reported. The magnetic LSL consists of approximately Lorentzian shaped peaks of alternating sign and thus has a vanishing average magnetic field. Snake trajectories, i.e., trajectories formed by the superposition of an oscillatory motion along the first direction and a motion with nonvanishing average velocity along the second direction [28], can become commensurate with the antidot lattice, and magnetoresistivity resonances are to be expected. Furthermore, for the magnetic modulation amplitudes applied here, closed electronic orbits are absent.

After the sample preparation and the experimental setup are introduced in Sec. II, the measurements are presented in Sec. III and interpreted with the help of numerical simulations in Sec. IV. The paper concludes with a summary and an outlook in Sec. V.

II. SAMPLE PREPARATION AND EXPERIMENTAL SETUP

A GaAs/Al$_{0.3}$Ga$_{0.7}$As heterostructure with a 2DEG 90 nm below the surface is used. After a brief illumination with infrared light, the unpatterned 2DEG has a density of 3.6×10^{15} m^{-2} and a mean-free path of 88 μm at liquid

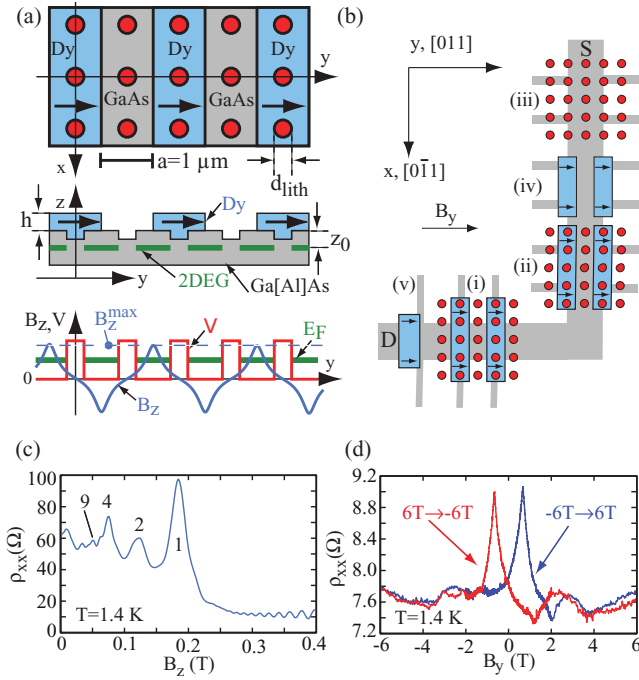―――――――
[*]thomas.heinzel@hhu.de

FIG. 1. (Color online) (a) Scheme of the hybrid lateral superlattice geometry. Circular holes (red circles) that form the antidots are etched into the sample. Every second line of antidots is covered by a Dy stripe of 1 μm width. The top view of the pattern is shown in the uppermost part. In the middle, a cross section in the yz plane at $x = 0$ is shown. The 2DEG is depleted underneath the etched regions. The Dy stripes are magnetized in the y direction, as indicated by the arrows. The corresponding electrostatic potential (possible strain effects are neglected) and the perpendicular magnetic field $B_z(y)$ are shown in the lowermost part. (b) Sketch of the sample layout. Two identical hybrid LSLs, (i) and (ii), are defined in an L-shaped Hall bar. The two components of the hybrid LSL, namely the antidot lattice (iii) and ferromagnetic stripes (iv) are defined separately, and the edge of a Dy pad centered in a Hall cross (v) enables Hall magnetometry. The coordinate system shows the crystallographic orientation of the Hall bar. (c) ρ_{xx} of array (iii) as a function of a homogeneous perpendicular magnetic field. Here, the peaks are labeled by the number of antidots in one cyclotron orbit. (d) $\rho_{xx}(B_y)$ of array (iv).

helium temperatures. The sample geometry is sketched in Figs. 1(a) and 1(b). An L-shaped Hall bar, oriented parallel to the natural GaAs cleavage directions, was prepared by optical lithography. Three identical, square antidot lattices (lattice constant $a = 1.0$ μm) were patterned on one Hall bar by electron beam lithography and subsequent reactive ion etching. Lithographic antidot diameters of $d_{\text{lith}} = 200$ nm (sample A) as well as $d_{\text{lith}} = 300$ nm (sample B) were prepared on separate Hall bars. As a consequence of a lateral depletion length of 45 nm around the antidots, this corresponds to electronic diameters of $d \approx 290$ nm and $d \approx 390$ nm, respectively, as measured by the Aharonov-Bohm oscillation period observed in large magnetic fields [29,30]. Since $(a - d)/\lambda_F \approx 17$ for sample A and ≈ 14 for sample B, these LSLs reside well inside the classical regime. After the definition of the antidots, Dy stripes of width a and a period of $2a$ were prepared on top of two antidot lattices by electron beam lithography,

enabling measurements of all resistivity components in one cool-down; see Fig. 1(b). The Dy stripes have a thickness of $h = 250$ nm to ensure a strong fringe field when magnetized. In sample A, they were deposited directly on the GaAs, while in sample B, a homogeneous film of 5 nm Cr plus 5 nm Au thickness was evaporated on top of the antidot lattice prior to the Dy deposition. This allows us to estimate the role of strain effects [7,31] possibly induced by the Dy stripes, which are centered at the columns of antidots and aligned parallel to the x direction. The lateral size of the superlattices is 100 μm in longitudinal and 50 μm in transverse direction (100 × 25 unit cells). For control measurements, the Hall bar furthermore contains a nominally identical magnetic stripe array without the antidots underneath, and the edge of a Dy film in a Hall cross for Hall magnetometry [32,33].

The samples were inserted in a ^{4}He gas flow cryostat with a variable temperature insert and a base temperature of 1.4 K. The system is equipped with a magnet of 8 T maximum field strength. The external magnetic field B_y was applied in the y direction. It magnetizes the Dy stripes to a magnetization of $\mu_0 M(B_y)$. The 2DEG responds predominantly to the z component of the fringe field of the Dy stripes, and we therefore neglect the influence of in-plane magnetic fields on the 2DEG throughout this paper. The magnetic field profile $B_z(y)$ is indicated in the lowermost section of Fig. 1(a). From the fringe field of a perfectly magnetized stripe, one expects [34]

$$B_z(y, B_y) = \frac{\mu_0 M(B_y)}{4\pi} \sum_{j=0}^{N-1} \ln\left(\frac{A^-}{A^+}\right),$$

$$A^{\pm} = \frac{\left[y - a\left(2j \mp \frac{1}{2}\right)\right]^2 + z_0^2}{\left[y - a\left(2j \mp \frac{1}{2}\right)\right]^2 + (z_0 + h)^2},$$

(1)

where z_0 is the distance between the 2DEG and the bottom of the Dy film, j is an integer, and N denotes the total number of Dy stripes. This magnetic profile has peaks of alternating sign with amplitude $B_z^{\max}(B_y) \equiv |B_z(y = [2j - \frac{1}{2}]a, B_y)|$. The maximum magnetization of our Dy films is $\mu_0 M \approx 2.7$ T for $B_y > 5$ T, corresponding to an upper limit of $B_z^{\max} \approx 480$ mT. The coercive magnetic field is $B_c = 670$ mT. The resistivity components $\rho_{ij}(B)$ with $i, j \in \{x, y\}$ were determined by applying an ac current of 100 nA with a frequency of 17.7 Hz from source S to drain D, see Fig. 1(b), and by measuring the electrostatic potentials in the x and y directions at voltage probes with a lock-in amplifier.

III. EXPERIMENTAL RESULTS

In Figs. 1(c) and 1(d), the magnetoresistivities of the LSL components of sample A for the two hybrid LSL components, namely the square antidot lattice (iii) and the array of magnetic stripes (iv), respectively, are reproduced. The antidot lattice reveals the well-known commensurability resonances with resistivity maxima at perpendicular magnetic fields where the cyclotron orbit is commensurate with one, two, four, or nine enclosed antidots [3–5]. For $B_z > 250$ mT, Shubnikov–de Haas oscillations set in. $\rho_{xx}(B_y)$ of the Dy stripes shows a peak centered at B_c and some weak features at larger magnetizations. This type of magnetoresistivity of magnetic
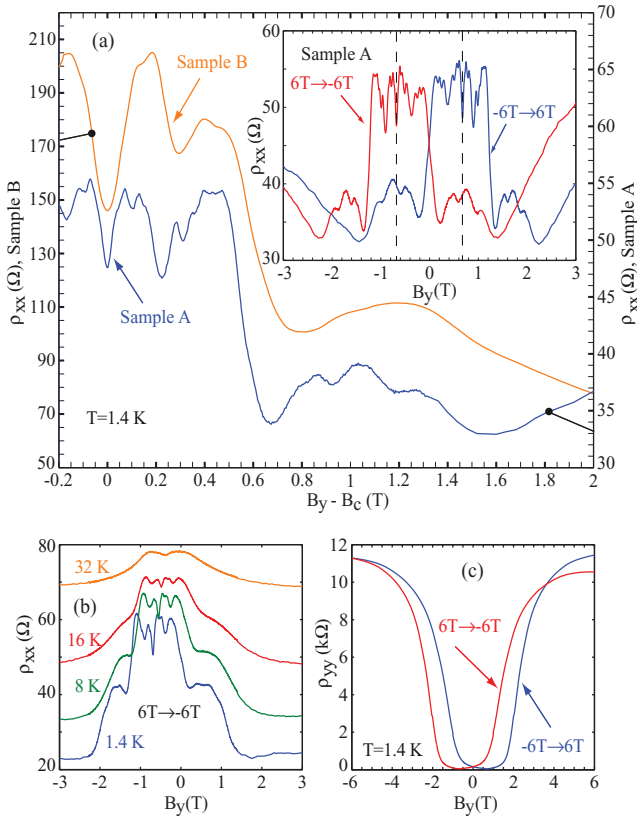
FIG. 2. (Color online) (a) Magnetoresistivities $\rho_{xx}(B_y - B_c)$ of the hybrid superlattices of samples A and B, shown for the up-sweeps (increasing B_y). The inset shows the hysteretic behavior, exemplified for sample A. The dashed lines indicate B_c. (b) Temperature dependence of $\rho_{xx}(B_y)$ for sample A, as observed in a different cool-down. Only the down-sweep direction is shown for clarity. The measurement of $\rho_{yy}(B_y)$ for sample A is reproduced in (c).

stripe arrays in in-plane magnetic fields has been studied theoretically [35], while to the best of our knowledge, experiments have been reported only in related configurations [36]. Numerical simulations based on the classical Kubo formalism (see below for details) give a weak, positive magnetoresistivity without fine structure [30], as measured for $|B_y| \gtrsim 4$ T. This indicates that the peak at B_c is not an intrinsic classical property of the magnetic profile itself, and we tentatively attribute it to the frequently observed and still not fully understood negative colossal magnetoresistance in high-mobility 2DEGs [37–39], which is beyond our focus here, possibly in combination with other effects such as weak localization. The strength of this feature depends on the cool-down cycle. It should be emphasized that ρ_{xx} of the 2DEG underneath the Dy array is constant over the full scan range within ± 0.8 Ω. For the following, this contribution can therefore be neglected.

The diagonal magnetoresistivities $\rho_{xx}(B_y)$ and $\rho_{yy}(B_y)$ of the hybrid LSLs are reproduced in Fig. 2, and we first focus on $\rho_{xx}(B_y)$ as observed on samples A and B (a). As B_y is detuned away from B_c, a positive magnetoresistivity is observed. As B_y is further increased, two peaks are seen, separated by a pronounced minimum. Around $B_y - B_c \approx 600$ mT, a decrease of ρ_{xx} by roughly a factor of 2 is seen, followed by

a broad maximum that extends up to $B_y - B_c \approx 2$ T. These most prominent features appear in sample B at somewhat larger magnetic fields than in sample A. Also, even though the positive magnetoresistance is less pronounced in sample A than in sample B, sample A shows clear additional finer structures, some of which are also adumbrated in $\rho_{xx}(B_y)$ of sample B. These differences can be traced back to the Cr/Au electrode present in sample B, as will be discussed below in more detail. In the following, we focus on sample A. In the inset of Fig. 2(a), the hysteretic behavior of $\rho_{xx}(B_y)$ is reproduced. The features observed in a single sweep are fairly symmetric about B_c, while reflection of the up-sweep about $B_y = 0$ coincides very well with the down-sweep. This behavior reflects the hysteretic magnetization of the Dy stripes which is not perfectly antisymmetric about $B_y = B_c$ (see below). These magnetoresistivity features show a weak temperature dependence, see Fig. 2(b), and the most pronounced ones remain visible up to $T \approx 16$ K. This suggests that they should be interpretable within a classical picture. They are furthermore superimposed on a slowly varying negative magnetoresistivity that extends to $|B_y - B_c| \approx 1.6$ T, after which it increases slightly. This background depends somewhat on the cool-down cycle. The strong positive magnetoresistivity in a narrow interval around B_c is still clearly visible at 32 K, and behaves similarly to that one observed in two-dimensional antidot lattices; see also Fig. 1(c). It is due to a B_z-induced increase in scattering at the antidots and is of no further interest here.

A smooth increase of $\rho_{yy}(B_y)$ is observed as B_y is driven away from B_c. A sharp increase sets in for $|B_y - B_c| \approx 1.6$ T and stops for $|B_y - B_c| \approx 3.5$ T; see Fig. 2(c). The shape of $\rho_{yy}(B_y)$ strongly resembles the one observed for single magnetic barriers [34], as well as magnetic barriers in series of alternating polarity [40]. Within a classical picture, the increasing amplitude of $B_z(y)$ reflects an increasing fraction of the incident electrons that gets reflected at the magnetic barrier. Above a threshold amplitude of $B_z(y)$, electrons can only pass the barrier via $\vec{E} \times \vec{B}$ drift at the edges of the Hall bar, or by scattering events inside the magnetic barrier [41]. These effects cause a saturation of ρ_{yy} at large $B_z^{\max}$. Since our ferromagnetic array represents an array of magnetic double barriers in series [40], $\rho_{yy}(B_y)$ can thus be qualitatively understood in terms of the properties of magnetic double barriers with the antidots acting as scatterers [30] and is not a unique signature of the hybrid lattice. The onset of the sharp increase of ρ_{yy} furthermore correlates with the end of the negative magnetoresistivity in the x direction. Comparison of $\rho_{xx}(B_y)$ to $\rho_{yy}(B_y)$ reveals that the transport at large magnetic fields is highly anisotropic. For example, for $|B_y - B_c| = 2.5$ T, the ratio ρ_{yy}/ρ_{xx} reaches a value of ≈ 230. This suggests that for sufficiently large magnetization of the Dy stripes, the electrons are guided along the x direction by the magnetic modulation, while crossing the magnetic walls is highly unlikely.

The off-diagonal components of the magnetoresistivity tensor were measured as well [30]. Since the average perpendicular magnetic field is zero, they vanish to a good approximation in the magnetic field range where the resonances in $\rho_{xx}(B_y)$ appear and are thus not very helpful for their interpretation.

IV. MODEL CALCULATION AND DISCUSSION

A coarse estimation, to be substantiated below, reveals that for $B_z^{max} \lesssim 500$ mT, $B_z(y)$ is too weak to generate closed cyclotron-type orbits. Therefore, the magnetoresistivity resonances must originate from open trajectories. This situation is quite different in comparison to antidot lattices in homogeneous magnetic fields where closed orbits, runaway trajectories, and chaotic orbits coexist and all contribute to the magnetoresistivity with a magnetic field-dependent weight [42]. Open cycloid orbits are absent as well in the interval where the resonances appear, and it is therefore expected that snake trajectories play an important role, the most obvious type of which is centered at the roots of $B_z(y)$ and runs along columns of antidots in the x direction. Since this is a classical picture and moreover the most pronounced features of the magnetoresistivity show a weak temperature dependence, it appears plausible to model them using the classical Kubo formalism. The code we use has been presented in detail elsewhere [43] and is therefore only briefly sketched here. We show the simulations for the parameters of sample A. Electrons are injected at random locations inside a unit cell of the LSL. They initially move in random directions with their Fermi velocity of $v_F = 2.6 \times 10^5$ m/s. The incremental change of the direction of motion by the inhomogeneous magnetic field given by Eq. (1) is calculated with a step width of 2 nm, and specular reflection at the antidots with $d = 290$ nm is assumed. Furthermore, $z_0 = 90$ nm is used, and we assume that the antidot potential is hard wall, as justified by the large a/d ratio. The simulations are carried out for zero temperature. From the simulated diffusion tensor obtained via the Kubo formula, the magnetoresistivity components are obtained via the Einstein relation for a degenerate 2DEG.

Figure 3(a) shows the simulated magnetoresistivity ρ_{xx} as a function of the maximum of the perpendicular magnetic field B_z^{max}; see also Figs. 1(a) and 1(b).

As in the experiment, several features in ρ_{xx} are observed. Close to $B_z^{max} = 0$, a positive magnetoresistivity is present. For $B_z^{max} < 250$ mT, a series of resistivity minima at $B_z^{max} = 32$ mT, 53 mT, and ≈ 110 mT is visible. A clear but weaker additional minimum is visible at $B_z^{max} \approx 170$ mT. Above a sharp decrease of ρ_{xx} at $B_z^{max} \approx 260$ mT, a broad minimum around 280 mT is present, followed by some weakly pronounced maxima and minima. Finally, another sharp decrease of ρ_{xx} around $B_z^{max} = 500$ mT is observed. A direct comparison with the measurements requires knowledge of the transformation function $\mu_0 M(B_y)$. Conceptually, it can be determined by Hall magnetometry of the stripe array on top of Hall crosses well inside the diffusive regime. In the ballistic or quasiballistic regime, the Hall voltage translates into the magnetization by nontrivial correction factors [33,44], the detailed discussion of which is beyond our scope here. Since such an estimation would still assume perfect, monodomain magnetization of the Dy stripes as well as a certain shape of the fringe field, some uncertainty would remain. Therefore, in order to estimate $\mu_0 M(B_y)$, we restricted ourselves to Hall magnetometry of the edge of a Dy film, prepared in the same process step as the magnetic lattice. The measured Hall voltage as a function of B_y, reproduced in Fig. 3(b), shows a marked peak where the average cyclotron diameter equals the width
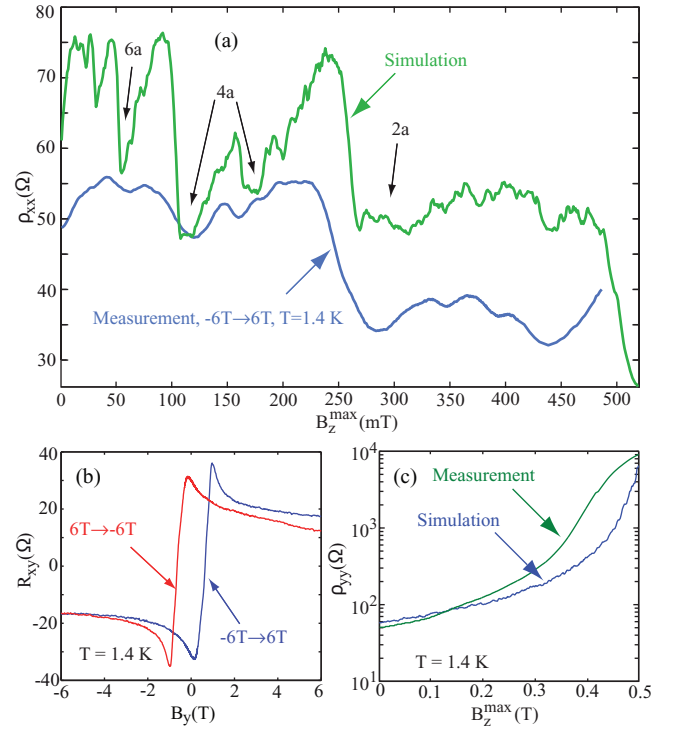

FIG. 3. (Color online) (a) $\rho_{xx}(B_z^{max})$ as simulated within the Kubo model, plotted as a function of the maximum of B_z. The period of the commensurate snake trajectories is indicated at the most prominent resistivity minima. The experimental trace of sample A has been scaled to B_z with the help of the magnetization trace, as obtained from the Hall resistance of one Dy edge centered inside a Hall cross (b). (c) Simulation results for $\rho_{yy}(B_z^{max})$ in comparison to the scaled experimental data of sample A.

of the voltage probe. The decrease of the Hall voltage at larger magnetic fields originates from ballistic effects [33]. The asymmetry of the Hall voltage furthermore indicates that the magnetization of the film is not perfect. Therefore, we compare the measured data to the simulations by scaling it with an approximated function $\mu_0 M(B_y)$, obtained numerically along the lines of Ref. [33], where $\mu_0 M$ is roughly proportional to B_y for $|B_y - B_c| < 600$ mT and depends only weakly on B_y for larger applied magnetic fields. This analysis of the Hall magnetometry indicates a saturation magnetization for the Dy stripes of ≈ 2.7 T, and $B_c = 670$ mT can be read out directly. The data measured at sample A in the up-sweep for $B_y > B_c$ in Fig. 2(a) are scaled accordingly and replotted in Fig. 3(a) as a function of B_z^{max}, which allows a more direct comparison to the simulations.

Even though the simulated function $\rho_{xx}(B_z^{max})$ deviates from the experimental trace in several aspects, the most prominent features are reproduced qualitatively, namely the positive magnetoresistivity around $B_z^{max} = 0$, minima close to $B_z^{max} = 53$ mT, 110 mT, 170 mT, and 280 mT, the decrease of ρ_{xx} at $B_z^{max} \approx 260$ mT, and some weakly pronounced maxima and minima at larger magnetic fields. The sharp decrease of of ρ_{xx} around $B_z^{max} = 500$ mT is not observed experimentally, most likely because our fringe fields are too weak.

The simulation of $\rho_{yy}(B_z^{\max})$ is compared to the scaled experimental data in Fig. 3(c). Very good agreement is found for $B_z^{\max} \leqslant 0.3$ T, while the strong increase of the resistivity around $B_z^{\max} \approx 0.4$ T is reproduced as well, though shifted to slightly higher magnetic fields. Further simulations [30] show that the presence of the antidots does influence $\rho_{yy}(B_z^{\max})$ to some extent, but the overall behavior is dominated by the magnetic barriers and is not an effect of the hybrid superlattice.

We proceed by interpreting the magnetoresistivity features in terms of the electron dynamics which determines the components of the magnetoconductivity tensor [30]. The off-diagonal elements σ_{xy} and σ_{yx} are approximately independent of $B_z^{\max}$ and of the order of 0.1 mS. σ_{yy} decreases from 18 mS at $B_z^{\max} = 0$ to almost zero at $B_z^{\max} \approx 0.5$ T. Only σ_{xx} shows resonances as $B_z^{\max}$ is changed. This implies that $\rho_{xx} \approx 1/\sigma_{xx}$ and $\rho_{yy} \approx 1/\sigma_{yy}$, while $\rho_{xy}(B_y) \approx \sigma_{xy}/(\sigma_{xx}\sigma_{yy})$. The sharp increase of ρ_{xy} (see Ref. [30]) and ρ_{yy} at $B_z^{\max} = 0.5$ T has thus its origin in the strongly suppressed diagonal conductivity in the y direction.

A deeper insight into the underlying electron dynamics can be gained by looking at characteristic electron trajectories. They can be identified with the help of Poincaré sections, which illustrate the dynamics of the electrons by their coordinates in a (i, v_j) cross section of the phase space ($i = x, y$ and $v_j, j = x, y$ denote the position and velocity coordinates, respectively). We start with a discussion of the minima of ρ_{xx} at smaller magnetic fields, $B_z^{\max} < 280$ mT. Each dot in Figs. 4(a)–4(e) represents the coordinates of an electron passing with $v_x > 0$ through one of the (y, v_y) planes located at $x = ma$, where m is an integer. The Poincaré section for $B_z^{\max} = 265$ mT (a) shows a pronounced accumulation of the electrons in a semicircle-like structure that extends over 85% of possible v_y components. This region hosts quasicommensurate snake trajectories with a wavelength very close to $2a$. They run parallel to the magnetic stripes, as illustrated by the sample trajectories shown in Fig. 4(f), and typically get scattered at the antidots after less than 30 snake periods. Likewise, the Poincaré sections for the minima of ρ_{xx} at $B_z^{\max} = 170$ mT (b), 108 mT (c), and at 53 mT (d) reveal that here, quasicommensurate snake trajectories of various periodicity exist. They extend along the x direction, and their weight decreases as the magnetic field is decreased, which correlates with the magnitude of the corresponding resistivity dips. Outside the resistivity minima, such an accumulation of electrons in snake trajectories is not seen in the Poincaré sections, as illustrated for $B_z^{\max} = 240$ mT in Fig. 4(e).

In addition, snake orbits exist which run at an angle $\neq 0$ to the x direction, as exemplified in Fig. 4(f). In the Poincaré sections, such trajectories form white regions, since the electrons do not return to the column in which they start. They can be found over the whole interval where resonances are observed, and we do not find a correlation between their weight in the Poincaré section and the magnetoresistivity. We furthermore emphasize that, as anticipated above, closed orbits are absent. It thus emerges that the minima of $\rho_{xx}(B_y)$ for $B_z^{\max} \lesssim 280$ mT correlate with the presence of quasicommensurate snake trajectories that run parallel to the magnetic stripes for many antidot periods, while snake trajectories running in other directions do not show such a correlation. Both the depletion and accumulation regions of the Poincaré
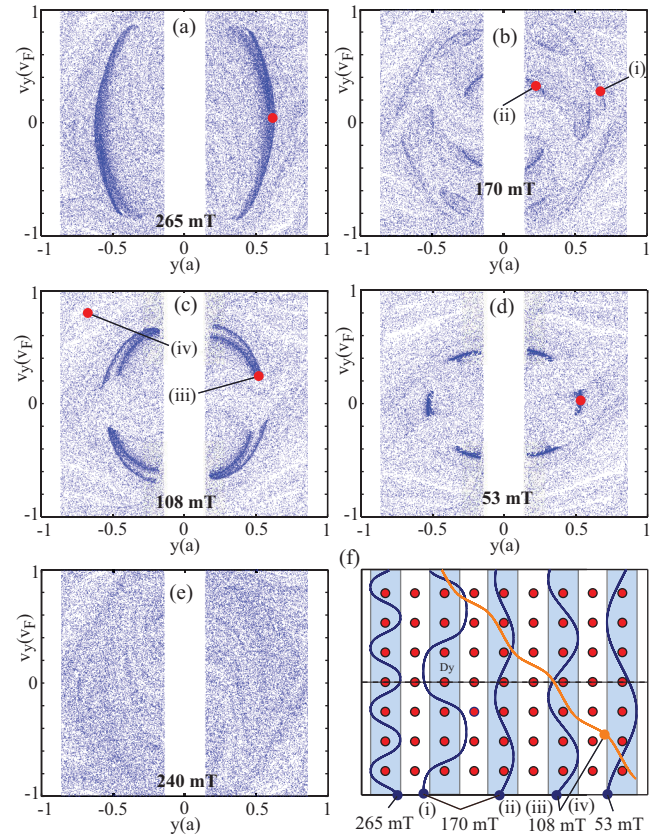

FIG. 4. (Color online) Poincaré sections for various values of $B_z^{\max}$ (a)–(e). Some characteristic trajectories are shown in (f), the initial conditions of which are indicated by full circles in the corresponding Poincaré sections.

sections are embedded in an approximately homogeneously filled background, which is due to electrons that move in snake orbits as well, but experience frequent scattering at the antidots. Typically, such trajectories complete no more that two snake periods before they get scattered [30]. We note that both the accumulation and the depletion regions contain mostly not perfectly periodic trajectories and are thus chaotic as well. Regular orbits should exist inside the accumulation regions, but we have been unable to identify such points in the Poincaré sections, which indicates that the regular regions have a very small volume. The composition of the phase space of this hybrid LSL is thus different to that of antidot lattices where disjunct, extended regular and chaotic regions coexist.

It is remarkable that adjacent resistivity minima sometimes correlate with accumulations of snake orbits of the same periodicity. For example, the minima at $B_z^{\max} = 170$ mT and at 108 mT both correlate with the accumulation of snake trajectories with a period close to $4a$. While the snake trajectories that belong to the pronounced minimum of ρ_{xx} at 108 mT remain commensurate over a relatively large interval of magnetic fields and initial conditions, those found at the weak minimum at 170 mT, like the two shown in (f) with their location indicated in the Poincaré section in (b), are more fragile.

For $B_z^{\max} > 280$ mT, the simulation shows a series of weakly pronounced features that end with a strong decrease
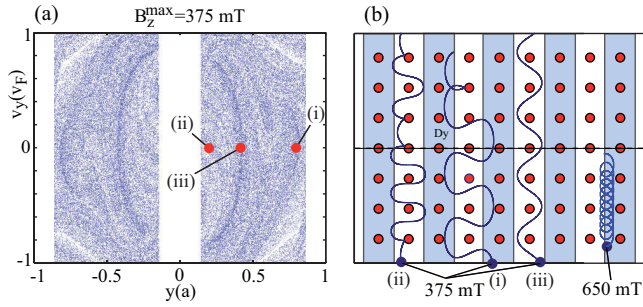
FIG. 5. (Color online) (a) Poincaré section for $B_z^{max} = 375$ mT. (b) Some typical trajectories at $B_z^{max} = 375$ mT with initial conditions as indicated by full circles in (a), and a cycloid trajectory for $B_z^{max} = 650$ mT.

of ρ_{xx} at $B_z^{max} \approx 500$ mT. Qualitatively similar features are observed experimentally for sample A and can be only guessed for sample B. In this interval, the Poincaré sections show a rich pattern of accumulation regions, together with a few depleted areas; see Fig. 5(a). This pattern evolves smoothly as a function of B_z^{max} without changing its qualitative appearance. The snake trajectories in this interval have a period close to $2a$ and show only a few oscillations before they get scattered. We also find occasional trajectory segments of skipping orbits; see Fig. 5(b). Thus, the magnetoresistivity features in the interval 280 mT $< B_z^{max} <$ 500 mT do not correlate in a straightforward way with characteristic trajectories.

The limit of large magnetic fields is characterized by $B_z^{max} \approx 500$ mT. It is not experimentally accessible in our samples. The simulations suggest that the decrease of ρ_{xx} originates from the formation of cycloid trajectories which drift along the magnetic field peaks. An example of such a trajectory is shown in Fig. 5(b). For $B_z^{max} > 520$ mT, cycloid orbits exist that never hit an antidot. Therefore, highly conductive channels in the x direction are formed.

We conclude this section by discussing possible reasons for the differences observed between sample A and sample B, as well as for the deviations between the simulations and the experiments. The most prominent features in sample B appear at higher magnetic fields than their respective counterparts in sample A. With the support of the corresponding numerical simulations, this can be traced back to the larger distance of the Dy stripes to the 2DEG due to the Cr/Au layer in between, which makes a higher magnetization necessary to achieve a fringe field of the same magnitude at the depth of the 2DEG. Also, the less prominent features observed at sample A are suppressed in sample B. This may be due to the larger antidot diameters in sample B which are known to smear out commensurability resonances [3]. Also, gating of high-mobility heterostructures can decrease the mobility [27].

The simulated amplitudes of the commensurability oscillations are furthermore stronger than the measured ones. We attribute this partly to the deviations of the real magnetic field profile $B_z(y)$ from the simulated one, which is to be expected from the asymmetric magnetization characteristics of the Dy film. Deviations from the assumed hard-wall potential may deform the trajectories, thereby weakening the resonances. Another possible reason is piezoelectric effects

due to strain imposed by the Dy stripes, which could modulate the electron density and the mobility for our crystallographic orientation of the Hall bars. This effect has been reported in the literature to get attenuated by depositing the stripes on top of a homogeneous metallic layer [7]. Therefore, by comparing the measurements of sample A with those of sample B, we conclude that if strain effects were relevant, they would generate additional fine structure rather than smearing it out. To further elucidate this issue, we have performed numerical simulations as described above, with an additional electrostatic potential of a cosine shape in the y direction with the period of the magnetic stripes and a rather strong amplitude of 1 meV, in accordance with typical values found in the literature [31,45]. Somewhat surprisingly, we do not find significant deviations of the resistivity from the unmodulated case (not shown) and therefore conclude that the magnetic field gradient dominates over electrostatic effects in the regime where the resonances are observed. Strain effects thus do not play a prominent role. Also, the simulation neglects finite-size effects. For example, a magnetic barrier close to the Hall bar edges induces $\vec{E} \times \vec{B}$ drift, and electron scattering at the Hall bar edges may provide additional conductance channels. Finally, at the large in-plane magnetic fields present in our implementation, magnetic mass effects can deform the snake trajectories to a small extent [46].

V. SUMMARY AND CONCLUSIONS

Hybrid magnetoelectric lateral superlattices composed of a two-dimensional antidot array and a one-dimensional magnetic modulation have been defined in high-mobility two-dimensional electron gases and studied by transport experiments in a configuration with vanishing average perpendicular magnetic field. Despite the absence of closed trajectories, pronounced classical magnetoresistivity resonances have been observed. The magnetoresistivity minima correlate with the accumulation of electrons in snake trajectories, as observed in Poincaré sections, that are quasicommensurate with the antidot lattice and oriented along the direction in which the magnetic field is homogeneous. Snake trajectories running in other directions are present as well, but their appearance does not correlate with the resistivity minima. The Poincaré sections do not show extended regular islands. We hope that these results will trigger quantum simulations of this system which should be able to interpret the magnetoresistivity resonances on a more fundamental level. The longitudinal magnetoresistivity is furthermore strongly anisotropic, with resistivity ratios above 200 for large magnetic fields. To a good approximation, however, the magnetoresistance in the direction perpendicular to the magnetic stripes can be understood as a resistance of magnetic barriers in series and does not reveal superlattice-specific properties. Further experiments may comprise the application of additional homogeneous perpendicular magnetic fields, a more detailed study of ρ_{yy}, the interaction of the electrons in snake trajectories with resonant electromagnetic radiation, or magnetic mass effects.

[1] D. Weiss, K. von Klitzing, K. Ploog, and G. Weimann, Europhys. Lett. **8**, 179 (1989).

[2] R. W. Winkler, J. P. Kotthaus, and K. Ploog, Phys. Rev. Lett. **62**, 1177 (1989).

[3] D. Weiss, M. L. Roukes, A. Menschig, P. Grambow, K. von Klitzing, and G. Weimann, Phys. Rev. Lett. **66**, 2790 (1991).

[4] K. Ensslin and P. M. Petroff, Phys. Rev. B **41**, 12307 (1990).

[5] A. Lorke, J. P. Kotthaus, and K. Ploog, Phys. Rev. B **44**, 3447 (1991).

[6] H. A. Carmona, A. K. Geim, A. Nogaret, P. C. Main, T. J. Foster, M. Henini, S. P. Beaumont, and M. G. Blamire, Phys. Rev. Lett. **74**, 3009 (1995).

[7] P. D. Ye, D. Weiss, R. R. Gerhardts, M. Seeger, K. von Klitzing, K. Eberl, and H. Nickel, Phys. Rev. Lett. **74**, 3013 (1995).

[8] K. W. Edmonds, B. L. Gallagher, P. C. Main, N. Overend, R. Wirtz, A. Nogaret, M. Henini, C. H. Marrows, B. J. Hickey, and S. Thoms, Phys. Rev. B **64**, 041303 (2001).

[9] C. W. J. Beenakker, Phys. Rev. Lett. **62**, 2020 (1989).

[10] I. S. Ibrahim, V. A. Schweigert, and F. M. Peeters, Phys. Rev. B **56**, 7508 (1997).

[11] R. R. Gerhardts, Phys. Rev. B **53**, 11064 (1996).

[12] J. Shi, F. M. Peeters, K. W. Edmonds, and B. L. Gallagher, Phys. Rev. B **66**, 035328 (2002).

[13] J. Eroms, M. Tolkiehn, D. Weiss, U. Rössler, J. de Boeck, and G. Borghs, Europhys. Lett. **58**, 569 (2002).

[14] R. Fleischmann, T. Geisel, and R. Ketzmerick, Phys. Rev. Lett. **68**, 1367 (1992).

[15] R. Fleischmann, T. Geisel, and R. Ketzmerick, Europhys. Lett. **25**, 219 (1994).

[16] R. Schuster, K. Ensslin, J. P. Kotthaus, M. Holland, and C. Stanley, Phys. Rev. B **47**, 6843 (1993).

[17] D. Weiss, K. Richter, E. Vasiadou, and G. Lütjering, Surf. Sci. **305**, 408 (1994).

[18] F. Nihey, S. W. Hwang, and K. Nakamura, Phys. Rev. B **51**, 4649 (1995).

[19] D. Hofstadter, Phys. Rev. B **14**, 2239 (1976).

[20] D. Pfannkuche and R. R. Gerhardts, Phys. Rev. B **46**, 12606 (1992).

[21] M. C. Geisler, J. H. Smet, V. Umansky, K. von Klitzing, B. Naundorf, R. Ketzmerick, and H. Schweizer, Phys. Rev. Lett. **92**, 256801 (2004).

[22] D. Weiss, K. Richter, A. Menschig, R. Bergmann, H. Schweizer, K. von Klitzing, and G. Weimann, Phys. Rev. Lett. **70**, 4118 (1993).

[23] Y. Aharonov and D. Bohm, Phys. Rev. **115**, 485 (1959).

[24] B. L. Altshuler, A. G. Aronov, and B. Z. Spivak, Pis'ma Zh. Eksp. Teor. Fiz. **33**, 101 (1981) [JETP Lett. **33**, 94 (1981)].

[25] K. Richter, Europhys. Lett. **29**, 7 (1995).

[26] V. Umansky, R. de Picciotto, and M. Heiblum, Appl. Phys. Lett. **71**, 683 (1997).

[27] C. Roessler, T. Feil, P. Mensch, T. Ihn, K. Ensslin, D. Schuh, and W. Wegscheider, New J. Phys. **12**, 043007 (2010).

[28] A. Nogaret, J. Phys. Condens. Matter **22**, 253201 (2010).

[29] Y. Iye, M. Ueki, A. Endo, and S. Katsumoto, J. Phys. Soc. Jpn. **73**, 3370 (2004).

[30] See Supplemental Material at http://link.aps.org/supplemental/10.1103/PhysRevB.91.195303 for additional magnetoresistivity measurements and for numerical simulations of the magneto-conductivity tensor elements.

[31] P. H. Beton, E. S. Alves, P. C. Main, L. Eaves, M. W. Dellow, M. Henini, O. H. Hughes, S. P. Beaumont, and C. D. W. Wilkinson, Phys. Rev. B **42**, 9229 (1990).

[32] M. Johnson, B. R. Bennett, M. J. Yang, M. M. Miller, and B. V. Shanabrook, Appl. Phys. Lett. **71**, 974 (1997).

[33] M. Cerchez and T. Heinzel, Appl. Phys. Lett. **98**, 232111 (2011).

[34] T. Vančura, T. Ihn, S. Broderick, K. Ensslin, W. Wegscheider, and M. Bichler, Phys. Rev. B **62**, 5074 (2000).

[35] I. S. Ibrahim and F. M. Peeters, Phys. Rev. B **52**, 17321 (1995).

[36] A. Nogaret, F. Nasirpouri, J.-C. Portal, H. E. Beere, D. A. Ritchie, A. T. Hindmarch, and C. H. Marrows, Europhys. Lett. **94**, 28001 (2011).

[37] L. Bockhorn, P. Barthold, D. Schuh, W. Wegscheider, and R. J. Haug, Phys. Rev. B **83**, 113301 (2011).

[38] A. T. Hatke, M. A. Zudov, L. N. Pfeiffer, and K. W. West, Phys. Rev. B **83**, 121301 (2011).

[39] Q. Shi, P. D. Martin, Q. A. Ebner, M. A. Zudov, L. N. Pfeiffer, and K. W. West, Phys. Rev. B **89**, 201301(R) (2014).

[40] V. Kubrak, F. Rahman, B. L. Gallagher, P. C. Main, M. Henini, C. H. Marrows, and M. A. Howson, Appl. Phys. Lett. **74**, 2507 (1999).

[41] M. Cerchez, S. Hugger, T. Heinzel, and N. Schulz, Phys. Rev. B **75**, 035341 (2007).

[42] I. V. Zozoulenko, F. A. Maao, and E. H. Hauge, Phys. Rev. B **56**, 4710 (1997).

[43] S. Meckler, T. Heinzel, A. Cavanna, G. Faini, U. Gennser, and D. Mailly, Phys. Rev. B **72**, 035319 (2005).

[44] A. K. Geim, S. V. Dubonos, J. G. S. Lok, I. V. Grigorieva, J. C. Maan, L. T. Hansen, and P. E. Lindelof, Appl. Phys. Lett. **71**, 2379 (1997).

[45] I. A. Larkin, J. H. Davies, A. R. Long, and R. Cuscó, Phys. Rev. B **56**, 15242 (1997).

[46] N. M. Sotomayor Choque, G. M. Gusev, J. R. Leite, A. A. Bykov, L. V. Litvin, N. T. Moshegov, A. I. Toropov, D. K. Maude, and J. C. Portal, Phys. Rev. B **66**, 035324 (2002).

Commensurability resonances in two-dimensional magneto-electric lateral superlattices

J. Schluck, S. Fasbender, and T. Heinzel

Condensed Matter Physics Laboratory, Heinrich-Heine-Universität, D-40225 Düsseldorf, Germany

K. Pierz and H. W. Schumacher

Physikalisch-Technische Bundesanstalt, Bundesallee 100, D-38116 Braunschweig, Germany

D. Kazazis and U. Gennser

CNRS-LPN, Route de Nozay, 91960 Marcoussis, France

(Dated: February 23, 2015)

This supplement provides additional information in relation to the sample parameters and the magnetoresistivity components of the hybrid superlattice.

PACS numbers: 73.23.-b, 73.63.-b
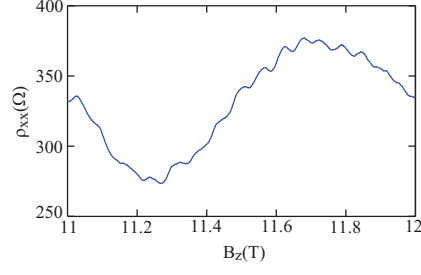
FIG. 1. Magnetoresistivity of an antidot lattice prepared by an identical process to that one in the paper, with the same lithographic diameter of $d_{lith} = 100\,\text{nm}$, without the magnetic stripes on top, in high magnetic fields. On top of the Shubnikov - de Haas resonance, a B-periodic modulation with a period of $\Delta B = 61\,\text{mT}$ is observed, that is interpreted as the Aharonov-Bohm oscillations around single antidots. It corresponds to a lateral depletion width of $45\,\text{nm}$.
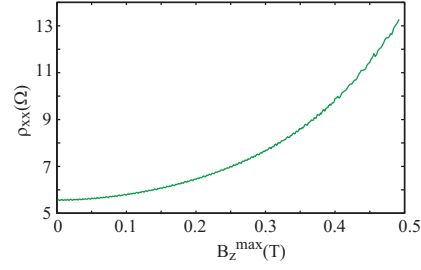
FIG. 2. Simulated classical $\rho_{xx}(B_y)$ of the Dy stripe array without the antidots underneath. A weak positive magnetoresistivity without fine structure up to $B_z^{max} \approx 0.48\,\text{T}$ is observed.
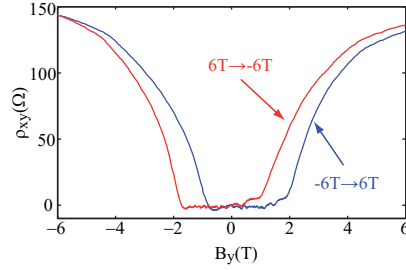
FIG. 3. (color online). Measurement of $\rho_{xy}(B_y)$. The absence of a Hall voltage for small B_y reflects that the average magnetic field in z-direction is zero. At larger B-fields, a non-zero Hall voltage is measured. It originates from the suppression of the off-diagonal components of the conductivity tensor, see Fig. 4.
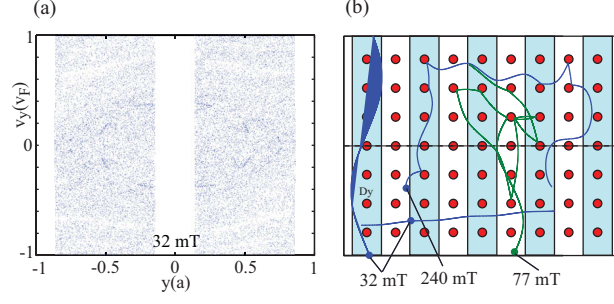
FIG. 4. (color online). (a) Poincaré section of the electron dynamics in the superlattice for the resistivity minimum at $B_z^{max} = 32$ mT. Only a very weak accumulation of electrons is visible. (b) Example trajectories for various values of B_z^{max}, in particular in the resistivity minimum at $B_z^{max} = 32$ mT, and outside the magnetoresistivity minima at $B_z^{max} = 77$ mT and 240 mT.
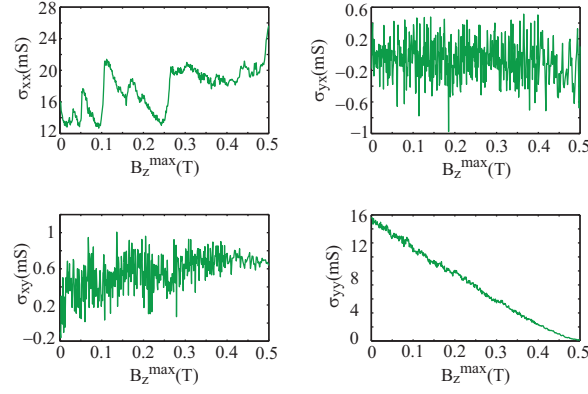

FIG. 5. (color online). Simulated magnetoconductivity tensor components of the hybrid superlattice. These data have been used to determine the elements of the resistivity tensor shown in the paper.
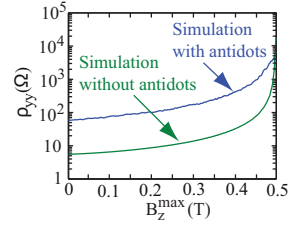
FIG. 6. (color online). Simulated magnetoresistivity $\rho_{yy}(B_z^{max})$ for the hybrid LSL in comparison to the magnetic LSL without antidots. For smaller magnetic fields, the antidots act as additional scatterers and increase the resistivity. For larger magnetic fields, where the magnetic barriers are high or even closed, scattering at the antidots facilitates the transmission of electrons, thereby decreasing the resistivity. Note that the antidots do not change the overall shape of $\rho_{yy}(B_z^{max})$.

Nonmonotonic Classical Magnetoconductivity of a Two-Dimensional Electron Gas in a Disordered Array of Obstacles

N. H. Siboni,[1] J. Schluck,[2] K. Pierz,[3] H. W. Schumacher,[3] D. Kazazis,[4,‡] J. Horbach,[1,*] and T. Heinzel[2,†]

[1]*Institut für Theoretische Physik II, Heinrich-Heine-Universität, Universitätsstraße 1, 40225 Düsseldorf, Germany*
[2]*Institut für Experimentelle Physik der kondensierten Materie, Heinrich-Heine-Universität,*
Universitätsstraße 1, 40225 Düsseldorf, Germany
[3]*Physikalisch-Technische Bundesanstalt, Bundesallee 100, 38116 Braunschweig, Germany*
[4]*CNRS, Université Paris-Sud, Université Paris-Saclay, C2N Marcoussis, 91460 Marcoussis, France*

Magnetotransport measurements in combination with molecular dynamics simulations on two-dimensional disordered Lorentz gases in the classical regime are reported. In quantitative agreement between experiment and simulation, the magnetoconductivity displays a pronounced peak as a function of the perpendicular magnetic field B which cannot be explained by existing kinetic theories. This peak is linked to the onset of a directed motion of the electrons along the contour of the disordered obstacle matrix when the cyclotron radius becomes smaller than the size of the obstacles. This directed motion leads to transient superdiffusive motion and strong scaling corrections in the vicinity of the insulator-to-conductor transitions of the Lorentz gas.

Reference

N. H. Siboni, J. Schluck, K. Pierz, H. W. Schumacher, D. Kazazis, J. Horbach, and T. Heinzel, Phys. Rev. Lett. 120, 056601 (2018), ©2018 American Physical Society

Copyright statement

Contributions

I designed the sample and contributed to sample preparation. I conducted the experiments and analyzed the experimental data. I contributed to manuscript writing.

Nonmonotonic Classical Magnetoconductivity of a Two-Dimensional Electron Gas in a Disordered Array of Obstacles

N. H. Siboni,[1] J. Schluck,[2] K. Pierz,[3] H. W. Schumacher,[3] D. Kazazis,[4,‡] J. Horbach,[1,*] and T. Heinzel[2,†]

[1]*Institut für Theoretische Physik II, Heinrich-Heine-Universität, Universitätsstraße 1, 40225 Düsseldorf, Germany*
[2]*Institut für Experimentelle Physik der kondensierten Materie, Heinrich-Heine-Universität,*
Universitätsstraße 1, 40225 Düsseldorf, Germany
[3]*Physikalisch-Technische Bundesanstalt, Bundesallee 100, 38116 Braunschweig, Germany*
[4]*CNRS, Université Paris-Sud, Université Paris-Saclay, C2N Marcoussis, 91460 Marcoussis, France*

Magnetotransport measurements in combination with molecular dynamics simulations on two-dimensional disordered Lorentz gases in the classical regime are reported. In quantitative agreement between experiment and simulation, the magnetoconductivity displays a pronounced peak as a function of the perpendicular magnetic field B which cannot be explained by existing kinetic theories. This peak is linked to the onset of a directed motion of the electrons along the contour of the disordered obstacle matrix when the cyclotron radius becomes smaller than the size of the obstacles. This directed motion leads to transient superdiffusive motion and strong scaling corrections in the vicinity of the insulator-to-conductor transitions of the Lorentz gas.

A system of noninteracting particles moving in a Poisson-distributed array of identical obstacles is known as a Lorentz gas. Originally proposed for the motion of electrons in a metal [1], the Lorentz gas has developed into a universal model for transport phenomena in many types of heterogeneous media, like anomalous diffusion in colloidal and biosystems [2–10], microwave-induced magnetoresistance oscillations [11], or negative magnetoresistance in metallic and semiconductor systems [12–17]. Versatile implementations of Lorentz gases can be realized experimentally by two-dimensional electron gases (2DEGs) exposed to a random array of obstacles. Such systems provide a high intrinsic electron mobility and the option to pattern the obstacles lithographically. A perpendicular magnetic field B tunes the cyclotron radius $R_{\mathrm{cy}} \propto B^{-1}$ of the electronic motion, acting as an additional characteristic length scale.

Experimental studies of the magnetotransport of 2DEGs in disordered obstacle arrays have been scarce (see, e.g., Refs. [18–23]). Especially, the magnetoconductivity $\sigma_{xx}(B)$ in a regime of high obstacle densities $n^\star$ and large magnetic fields has not been systematically explored up to now. Here, $n^\star$ denotes the dimensionless number density of obstacles, $n^\star = (N/A)R_{\mathrm{int}}^2$, with N the number of obstacles, A the area of the system, and R_{int} the interaction distance between an electron and an obstacle, i.e., the effective radius of the (circular) obstacles. In this Letter, we present a classical experimental realization of a Lorentz gas in combination with classical molecular dynamics (MD) simulations and demonstrate that the electron transport qualitatively changes if the cyclotron radius R_{cy} becomes smaller than

the interaction distance R_{int}. As expected from kinetic theories, the conductivity $\sigma_{xx}(B)$ is a monotonically decaying function at low densities. For large densities and $R_{\mathrm{cy}} \lesssim R_{\mathrm{int}}$, however, it exhibits a maximum that moves to larger values of B with increasing $n^\star$. This maximum has been observed in simulations [24,25], but it has hitherto remained unexplained and not been observed experimentally. Our study provides the first experimental verification of the phase diagram for the magnetotransport in the 2D Lorentz gas, and our simulation analysis elucidates a so far unexplored dynamic regime.

The magnetotransport in the 2D Lorentz gas is associated with two insulator-to-conductor transitions at high and low obstacle density $n^\star$ which are due to underlying static percolation transitions [24,25]. The location of the transition at a high density is independent of the magnetic field B and located at a critical density $n_c^\star = 0.359$ for a Poisson-distributed arrangement of overlapping disks: While for $n < n_c^\star$ the electron exhibits diffusive transport through the void space between the obstacles, for $n > n_c^\star$ the void space is disconnected into finite pockets in which the electron is trapped. The second, B-dependent localization transition occurs at a density $n_{\mathrm{ld},c}^\star(B) < n_c^\star$. It can be understood in terms of skipping orbits that the electrons, acting as tracer particles in this experimental implementation, perform around the obstacles, or clusters thereof. This localizes all particles as $n^\star$, or the cyclotron radius R_{cy}, respectively, is decreased [24].

For a fixed B field, the magnetoconductivity exhibits a maximum as a function of $n^\star$ which is located at $n_{\mathrm{ld},c}^\star < n_{\max}^\star < n_c^\star$. This maximum is intimately related to

the maximum in $\sigma_{xx}(B)$. The line of maxima, $n^{\star}_{\max}(B)$, is the geometric mean of the two critical densities. The change of the transport for $R_{cy} \lesssim R_{int}$ along the line $n^{\star}_{\max}(B)$ is due to a change of the motion of the tracer particles (electrons) from a diffuse scattering by the obstacles to a directed motion along the contour of the obstacle arrangement. In the limit $B \to \infty$, this directed motion completely dominates the transport and suppresses the critical slowing down at $n^{\star}_{ld,c}$ and $n^{\star}_c$. At finite but high B fields, it leads to strong corrections to the scaling behavior in the vicinity of the critical points.

A GaAs/Al$_{0.3}$Ga$_{0.7}$As heterostructure with a 2DEG located 150 nm below the surface is used. The electron density and mobility are $n_e = 2.5 \times 10^{15}$ m^{-2} and 340 m^2/V s, respectively, corresponding to a mean free path of 31 μm at temperatures below 1 K. The repulsive Lorentz obstacles are formed by circular holes in the 2DEG. They are patterned by electron beam lithography and subsequent reactive ion etching. Within each array, the obstacles are of identical size, while their positions are Poisson distributed, with mutual overlaps allowed. All disks have a lithographic radius of 425 nm; see Fig. 1(a). From Aharonov-Bohm measurements in large magnetic fields [26], we estimate [27] the lateral depletion length to ≈ 75 nm, such that the effective electronic disk radius is $R_{int} \approx 500$ nm. The chip contains

four Lorentz arrays with disk densities $n^{\star} = 0.065$, 0.13, 0.195, and 0.26. The arrays have an area of 200 μm by 100 μm. The mean free path due to the scattering at the disks is 4.0, 2.0, 1.3, and 1.0 μm, respectively.

The samples were measured in a dilution refrigerator with a base temperature of 8 mK. The electron temperature is estimated to ≈ 80 mK. A ^{4}He gas flow cryostat with a variable temperature insert and a base temperature of 1.4 K is used for measurements at temperatures above 1 K. An ac current (500 nA, 17.7 Hz) is injected. The longitudinal and Hall voltages are measured using lock-in amplifiers.

The longitudinal magnetoresistivity $\rho_{xx}(B)$ [see Fig. 1(a)] shows a strong peak around $B = 0$ which in some arrays extends well into the range where Shubnikov–de Haas oscillations [28] are observed. As $n^{\star}$ is increased from 0.065 to 0.26, $\rho_{xx}(0)$ increases by approximately a factor of 50. In addition, a small, narrow peak on top at $B = 0$ is observed which will be discussed elsewhere.

The longitudinal magnetoconductivity is obtained from the measured resistivity components via $\sigma_{xx}(B) = \rho_{xx}(B)/[\rho^2_{xx}(B) + \rho^2_{xy}(B)]$, where $\rho_{xy}(B)$ denotes the Hall resistivity (see Supplemental Material [29]). In Fig. 1(b), the obtained $\sigma_{xx}(B)$ is shown for the array with $n^{\star} = 0.195$ for various temperatures. A pronounced maximum at $B \approx 140$ mT is observed. It shows a weak temperature dependence and evolves at higher temperatures into a shoulder that is still visible at 32 K. This weak temperature dependence indicates a classical origin. We have observed the same phenomenology in a set of scaled samples with identical number densities but with $R_{int} = 1 \mu$m [29]. This behavior is in qualitative contradiction to both the Boltzmann model as well as to the Bobylev model valid for Lorentz gases with small $n^{\star}$ [30]. Rather, it is associated with the above-mentioned conductivity maximum as predicted by numerical simulations for high-density Lorentz gases [24,25]. A magnetoconductivity maximum in 2D arrays of randomly placed obstacles is actually visible in the data reported by Lütjering [20]. It has, however, a different phenomenology than the data discussed here and is probably related to the anomalous weak localization present in these samples [23]. We note that, in arrays of periodic obstacles, magneto-conductivity peaks are well known; see, e.g., Refs. [31,32]. They have their origin in electron trajectories commensurate with the lattice [33] and are thus of a distinctly different character.

MD simulations of a system of noninteracting fluid particles in a 2D matrix of randomly placed obstacle particles are performed using LAMMPS [34]. Matrix (index M) and fluid particles (F) interact via a shifted, purely repulsive Weeks-Chandler-Andersen potential, $u_{FM}(r) = 4\varepsilon[(R_{int}/r)^{12} - (R_{int}/r)^6 + 1/4]$ for $r < 2^{1/6}R_{int}$ and $u_{FM}(r) = 0$ otherwise. Here, we have set the energy parameter to $\varepsilon = 0.1\varepsilon_M$ and the interaction range to $R_{int} = 0.5\sigma_M$, where $\varepsilon_M = 1.0$ and $\sigma_M = 1.0$ correspond to the energy parameter and the diameter of the obstacle
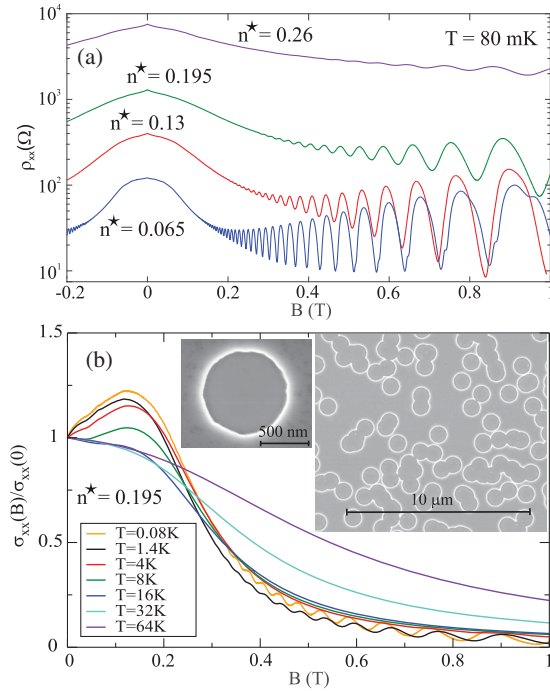

FIG. 1. (a) Longitudinal magnetoresistivities ρ_{xx} for various obstacle densities $n^{\star}$, measured at a temperature of ≈ 80 mK. (b) The magnetoconductivity $\sigma_{xx}(B)$ and its temperature dependence for $n^{\star} = 0.195$. Insets: Scanning electron microscope picture of a Lorentz array section with $n^{\star} = 0.195$ and magnified view of a single disk.

particles, respectively. For the comparison between the simulation and experiment, exactly the same configurations of obstacles as in the experiment are implemented. Otherwise, we use 100 statistically independent matrix structures at each density $n^\star = (N/L^2)R_{int}^2$, with N the number of matrix particles and L the linear dimension of the simulation square.

Newton's equations of motion are integrated using the velocity-Verlet algorithm [35] with a time step of $10^{-3}t_0$ with $t_0 := [m(\sigma_M)^2/\varepsilon_M]^{1/2}$ and $m = 1.0$ the mass of a fluid particle. The particles carry a charge $e = 1$ and a mass $m = 1$ and are subjected to a uniform magnetic field B that acts perpendicular to the plane of motion. The velocity of the fluid particles is fixed to a constant magnitude $v_F = \sqrt{2}$, which corresponds to the Fermi velocity of the 2DEG in the experiment, i.e., $v_F = \hbar\sqrt{2\pi n_e}/m = 2.17 \times 10^5$ m/s, where m denotes the effective electron mass in GaAs. It is associated with a cyclotron radius of $R_{cy} = mv_F/(eB)$ or $R_{cy} = R_{int}/\tilde{B}$, with $\tilde{B}$ being the dimensionless magnetic field $\tilde{B} = B/B_0$ (with $B_0 = (mv_F/eR_{int})$). Between 100 and 2400 fluid particles per host structure are used for runs of up to $10^6 t_0$. For the calculation of time averages, ten time origins per run are used, spaced equidistantly over the whole simulation time.

The conversion of units between the simulation and experiment is as follows: $\sigma_M = 10^{-6}$ m (obstacle diameter), $m = 6.097 \times 10^{-32}$ kg, $t_0 = 9.226 \times 10^{-12}$ s, $e = 1.6 \times 10^{-19}$ C (electron charge), and $B_0 = 0.168$ T.

For a system of noninteracting charged particles, the conductivity σ_{xx} is directly related to the self-diffusion constant D via $\sigma_{xx} = (n_e e^2/m)D$. Hence, we can directly compare the experimentally obtained conductivity, normalized to its value at $\tilde{B} = 0$, $\sigma_{xx}(\tilde{B})/\sigma_{xx}(0)$, to the corresponding ratio of diffusion constants from the MD simulation, $D(\tilde{B})/D(0)$. In the simulation, the self-diffusion constant can be obtained from the long-time limit of the mean-squared displacement (MSD) of a tagged particle, $\delta r^2(t)$, using the Einstein relation $D = \lim_{t\to\infty} \delta r^2(t)/4t$. Here, the MSD is defined as $\delta r^2(t) = \langle[\vec{r}(t) - \vec{r}(0)]^2\rangle$, with $\vec{r}(t)$ the position of the particle at time t and $\langle\ldots\rangle$ an ensemble average.

The comparison of $\sigma_{xx}(\tilde{B})/\sigma_{xx}(0)$ from the experiment with $D(\tilde{B})/D(0)$ from the simulation is shown in Fig. 2(a) for different number densities. Close to the σ_{xx} maximum, the simulation and experiment are in good agreement except for the highest $n^\star$. Thus, both weak localization corrections [37] and interaction effects [38] can be excluded as possible origins. The experimental values are significantly larger than the ones from the simulation at high $\tilde{B}$ fields. We tentatively attribute these deviations to a combination of quantum effects like the onset of Shubnikov–de Haas oscillations and depinning of electrons from the obstacle clusters by the residual random disorder
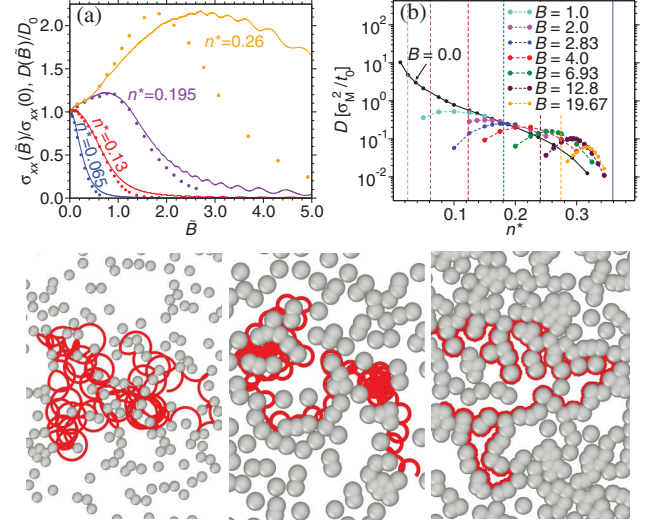

FIG. 2. (a) $\sigma_{xx}(\tilde{B})/\sigma_{xx}(0)$ from the experiment (full lines) in comparison to $D(\tilde{B})/D(0)$ from the simulation (full circles) for different values of $n^\star$. (b) $D(n^\star/n_c^\star)$ from the simulation for different values of $\tilde{B}$. The vertical lines correspond to the locations of $n_c^\star$ (solid line) and $n_{ld,c}^\star(\tilde{B})$ (dashed lines). The snapshots correspond to the location of the maxima in $D(n^\star)$ for $\tilde{B} = 0.35$, 1.0, and 6.95 (from left to right). The trajectories are illustrated using OVITO [36].

[13]. However, different from the monotonic decay of $\sigma_{xx}(\tilde{B})/\sigma_{xx}(0)$ and $D(\tilde{B})/D(0)$ at low densities, a maximum occurs at large densities (see, e.g., the results for $n^\star = 0.195$, where the simulation and experiment are in very good agreement around the maximum).

To get further insight into the nature of this change, we plot in Fig. 2(b) the diffusion constant from the simulation as a function of the number density, $D(n^\star)$, for different values of $\tilde{B}$, including $\tilde{B} = 0$. At a given finite value of $\tilde{B}$, the diffusion coefficients vanish at the critical densities $n_c^\star$ and $n_{ld,c}^\star(\tilde{B}) < n_c^\star$. Therefore, at a given value of $\tilde{B}$, the function $D(n^\star)$ exhibits a maximum in the interval $[n_{ld,c}^\star(B), n_c^\star]$. The snapshots in Fig. 2 show typical trajectories for different densities corresponding to the maxima in $D(n^\star)$ at $\tilde{B} = 0.35$, 1.0, and 6.95 from left to right (cf. corresponding movies in Supplemental Material [29]). These snapshots indicate a qualitative change of the motion around $\tilde{B} = 1$, from a diffuse scatter of the tracer particle by the obstacle for $\tilde{B} \ll 1$ to a directed motion along the contour of the obstacle network for $\tilde{B} \gg 1$. The trajectory at $\tilde{B} = 1.41$ indicates a mixture of diffuse scattering and directed motion.

The phase diagram in Fig. 3 shows $\tilde{B}$ vs $n^\star/n_c^\star$, with the two lines of critical points at low and high density. While the critical points at high density are independent of $\tilde{B}$ at $n^\star/n_c^\star = 1$, the low-density critical points are located at $\tilde{B}_{ld,c} = (\sqrt{n_c^\star/n^\star} - 1)^{-1}$ [24]. The dashed red line in
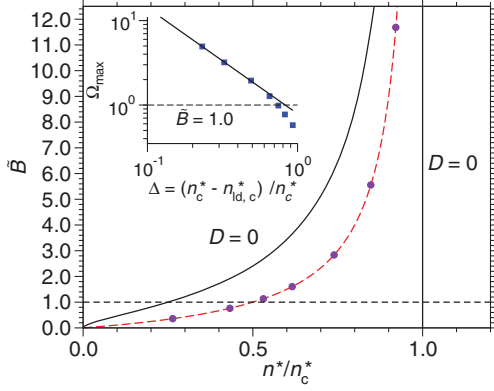
FIG. 3. Phase diagram in terms of $\tilde{B}$ vs $n^{\star}/n_c^{\star}$. The red dashed line is obtained from Eq. (1), and filled blue circles show $\tilde{B}_{\max}$, as determined from the simulation [cf. Fig. 2(b)]. The inset shows $\Omega_{\max}$ as a function of Δ, with the solid line being a fit with $\Omega_{\max} \propto \Delta^{-1.25}$ (see the text).

FIG. 4. (a) MSDs, $\delta r^2(t)$, for the densities $n^{\star} = 0.078, 0.195$, and 0.33. The dashed lines are for $\tilde{B} = 0$, while the solid lines correspond to the location of maximal diffusion at $\tilde{B} = 0.36$, 1.02, and 7.09, respectively. Panels (b)–(d) show the local exponents $\gamma(t)$, corresponding to the MSDs in (a).

between the two critical lines in Fig. 3 corresponds to the points of maximal diffusion. Its form can be understood as follows: The density $n_{\max}(\tilde{B})$ at which the diffusion coefficient is maximal is associated with two limiting cases. The maximum vanishes towards $\tilde{B} \to 0$, i.e., $n_{\max}(\tilde{B} \to 0) = 0$, and it should coincide with $n_c^{\star}$ in the limit $\tilde{B} \to \infty$ (then $R_{\mathrm{cy}} = 0$ and $n_c^{\star} = n_{\mathrm{ld},c}^{\star}$). A function that interpolates between these two limiting cases is $n_{\max}^{\star} = n_c^{\star} R_{\mathrm{int}} (R_{\mathrm{int}} + R_{\mathrm{cy}})^{-1}$. When this expression is solved for $\tilde{B}$, one obtains the following law for the density dependence of the reduced magnetic field at maximal diffusion:

$$\tilde{B}_{\max} = (n_c^{\star}/n^{\star} - 1)^{-1}. \tag{1}$$

The points that are on the maximal diffusion curve in Fig. 3 are directly obtained from the data in Fig. 2(b), confirming that Eq. (1) indeed holds. Thus, remarkably, $n^{\star}(\tilde{B}_{\max}) = \sqrt{n_{\mathrm{ld},c}^{\star} n_c^{\star}}$. Along this line of maxima, the transport of the tracer particle changes around $\tilde{B} = 1$. This can be inferred from the inset in Fig. 3, where the ratio of the diffusion constant at the maximum to that at $\tilde{B} = 0$ at the corresponding density, $\Omega_{\max} = D_{\max}(B)/D(n_{\max}^{\star}, \tilde{B} = 0)$, is plotted as a function of the distance between the two critical lines at a given value of $\tilde{B}$, $\Delta = (n_c^{\star} - n_{\mathrm{ld},c}^{\star})/n_c^{\star}$. For $\Delta \lesssim 0.7$, the ratio $\Omega_{\max}$ is larger than 1.0 (corresponding also to $\tilde{B} > 1.0$), and the data can be fitted with a power law, $\Omega_{\max} \propto \Delta^{-1.25}$, indicating a divergence of this ratio towards $\tilde{B} \to \infty$. As a consequence, one expects at least strong corrections to the asymptotic critical behavior for large $\tilde{B}$ fields, and, in the limit $\tilde{B} \to \infty$, where the two critical points meet, the diffusion constant does not vanish but becomes infinite.

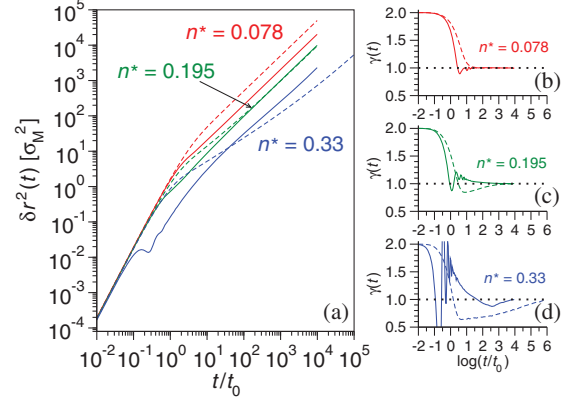On a microscopic scale, the qualitative change of the tracer particle motion around $\tilde{B} = 1$ can be analyzed in terms of MSDs. Figure 4(a) displays MSDs at three different states of maximal diffusion, $(n_{\max}^{\star}, \tilde{B})$ (cf. the snapshots in Fig. 2 at the same states). Also included are MSDs for $\tilde{B} = 0$ (dashed lines) at the corresponding densities. The onset of a directed motion along the contour of the obstacles is associated with a superlinear regime in the MSD at intermediate times for $t \gtrsim 3t_0$. This is especially evident from the behavior of the local exponent of the MSD, $\gamma(t) = d \log[\delta r^2(t)]/d \log(t)$, which is shown in Figs. 2(b)–2(d) for the three different densities. At $n^{\star} = 0.078$ the diffusive regime is already reached around $t = 10t_0$, and the diffusion for $\tilde{B} = 0.36$ is slightly slower than for $\tilde{B} = 0$ due to the existence of the low-density critical point in the former case. At $n^{\star} = 0.195$, there is a superlinear regime for $1.0t_0 \lesssim t \lesssim 100t_0$ at $\tilde{B} = 1.02$, while in the case of $\tilde{B} = 0$, a sublinear regime is seen in the same time range. A similar effect, albeit much more pronounced, is present for $n^{\star} = 0.33$. Here, the $\tilde{B} = 0$ curve shows an extended sublinear regime over about 2–3 orders of magnitude due to the vicinity of the critical density $n_c^{\star}$. This regime is almost suppressed for $\tilde{B} = 7.09$; instead, a pronounced superlinear regime and a faster transition towards normal diffusion are observed. This indicates that particularly in a dense matrix the application of a magnetic field $\tilde{B} \gg 1.0$ leads to a very efficient exploration of the matrix due to the directed motion along the contour of the obstacle matrix.

In summary, we have studied the magnetotransport through 2D disordered Lorentz gases in the classical regime. Our focus was on the nonmonotonic behavior of the conductivity and diffusion which is seen for magnetic fields $\tilde{B} \gtrsim 1.0$. We emphasize that the system under study is

also related to the active motion of microswimmers [7–10] and thus has a more general relevance. The threshold $\tilde{B} \approx 1.0$ marks the point where the cyclotron radius becomes smaller than the obstacle radius. This leads to the change in the motion of the tracer particle from a diffuse scatter by the obstacles to a directed motion along the obstacle contour. The latter directed motion is associated with an intermediate superlinear regime in the MSD that becomes more pronounced with increasing $\tilde{B}$.

We have shown that one can draw a line of maximal diffusion into the phase diagram that follows the law given by Eq. (1). Along this line, the diffusion constant ratio Ω_{max} (see above) diverges in the limit $\tilde{B} \to \infty$. Thus, in this limit the directed motion dominates the transport and leads to a divergence instead of a vanishing of the diffusion coefficient. For finite $\tilde{B}$, at least strong scaling corrections are expected in the vicinity of the two critical points.

The findings presented in this Letter open the door to further experimental studies in combination with quantitative comparisons to the theory and simulation, considering different nonspherical obstacle shapes, quantum corrections, or the role of additional Gaussian disorder [13].

[*]horbach@thphy.uni-duesseldorf.de
[†]Thomas.Heinzel@hhu.de
[‡]Present address: Laboratory for Micro- and Nanotechnology, Paul Scherrer Institute, 5232 Villigen-PSI, Switzerland.

[1] H. Lorentz, Proc. Acad. Sci. Amsterdam **7**, 438 (1905).
[2] F. Höfling, T. Franosch, and E. Frey, Phys. Rev. Lett. **96**, 165901 (2006).
[3] M. R. Horton, F. Höfling, J. O. Rädler, and T. Franosch, Soft Matter **6**, 2648 (2010).
[4] F. Höfling and T. Franosch, Rep. Prog. Phys. **76**, 046602 (2013).
[5] T. O. E. Skinner, S. K. Schnyder, D. G. A. L. Aarts, J. Horbach, and R. P. A. Dullens, Phys. Rev. Lett. **111**, 128301 (2013).
[6] S. K. Schnyder, M. Spanner, F. Höfling, T. Franosch, and J. Horbach, Soft Matter **11**, 701 (2015).
[7] F. Kümmel, B. ten Hagen, R. Wittkowski, I. Buttinoni, R. Eichhorn, G. Volpe, H. Löwen, and C. Bechinger, Phys. Rev. Lett. **110**, 198302 (2013).
[8] E. Lauga, W. R. DiLuzio, G. M. Whitesides, and H. A. Stone, Biophys. J. **90**, 400 (2006).
[9] M. Han, J. Yan, S. Granick, and E. Luijten, Proc. Natl. Acad. Sci. U.S.A. **114**, 7513 (2017).
[10] M. Zeitz, K. Wolff, and H. Stark, Eur. Phys. J. E **40**, 23 (2017).
[11] Y. M. Beltukov and M. I. Dyakonov, Phys. Rev. Lett. **116**, 176801 (2016).
[12] B. L. Altshuler, D. E. Khmelnitskii, A. I. Larkin, and P. A. Lee, Phys. Rev. B **22**, 5142 (1980).
[13] A. D. Mirlin, D. G. Polyakov, F. Evers, and P. Wölfle, Phys. Rev. Lett. **87**, 126805 (2001).
[14] D. G. Polyakov, F. Evers, A. D. Mirlin, and P. Wölfle, Phys. Rev. B **64**, 205306 (2001).
[15] A. Dmitriev, M. Dyakonov, and R. Jullien, Phys. Rev. Lett. **89**, 266804 (2002).
[16] A. Dmitriev, A. D. Mirlin, D. G. Polyakov, and M. A. Zudov, Rev. Mod. Phys. **84**, 1709 (2012).
[17] L. Bockhorn, I. V. Gornyi, D. Schuh, C. Reichl, W. Wegscheider, and R. J. Haug, Phys. Rev. B **90**, 165434 (2014).
[18] G. M. Gusev, P. Basmaji, Z. D. Kvon, L. V. Litvin, Y. Nastaushev, and A. I. Toropov, J. Phys. Condens. Matter **6**, 73 (1994).
[19] K. Tsukagoshi, S. Wakayama, K. Oto, S. Takaoka, K. Murase, and K. Gamo, Phys. Rev. B **52**, 8344 (1995).
[20] G. Lütjering, Ph.D. thesis, University of Stuttgart, 1996.
[21] G. Nachtwei, G. Lütjering, D. Weiss, Z. H. Liu, K. von Klitzing, and C. T. Foxon, Phys. Rev. B **55**, 6731 (1997).
[22] G. Nachtwei, Z. H. Liu, G. Lütjering, R. R. Gerhardts, D. Weiss, K. von Klitzing, and K. Eberl, Phys. Rev. B **57**, 9937 (1998).
[23] O. Yevtuchenko, G. Lütjering, D. Weiss, and K. Richter, Phys. Rev. Lett. **84**, 542 (2000).
[24] A. Kuzmany and H. Spohn, Phys. Rev. E **57**, 5544 (1998).
[25] W. Schirmacher, B. Fuchs, F. Höfling, and T. Franosch, Phys. Rev. Lett. **115**, 240602 (2015).
[26] Y. Iye, M. Ueki, A. Endo, and S. Katsumoto, J. Phys. Soc. Jpn. **73**, 3370 (2004).
[27] J. Schluck, S. Fasbender, T. Heinzel, K. Pierz, H. W. Schumacher, D. Kazazis, and U. Gennser, Phys. Rev. B **91**, 195303 (2015).
[28] T. Ando, A. B. Fowler, and F. Stern, Rev. Mod. Phys. **54**, 437 (1982).
[29] See Supplemental Material at http://link.aps.org/supplemental/10.1103/PhysRevLett.120.056601 for additional experimental and simulation data as well as simulation movies.
[30] A. V. Bobylev, F. A. Maaø, A. Hansen, and E. H. Hauge, Phys. Rev. Lett. **75**, 197 (1995).
[31] D. Weiss, M. L. Roukes, A. Menschig, P. Grambow, K. von Klitzing, and G. Weimann, Phys. Rev. Lett. **66**, 2790 (1991).
[32] K. Ensslin and P. M. Petroff, Phys. Rev. B **41**, 12307 (1990).
[33] R. Fleischmann, T. Geisel, and R. Ketzmerick, Phys. Rev. Lett. **68**, 1367 (1992).
[34] S. Plimpton, J. Comput. Phys. **117**, 1 (1995).
[35] K. Binder, J. Horbach, W. Kob, W. Paul, and F. Varnik, J. Phys. Condens. Matter **16**, S429 (2004).
[36] A. Stukowski, Model. Simul. Mater. Sci. Eng. **18**, 015012 (2010).
[37] B. L. Altshuler, A. G. Aronov, and D. E. Khmelnitsky, J. Phys. C **15**, 7367 (1982).
[38] P. S. Alekseev, Phys. Rev. Lett. **117**, 166601 (2016).

Nonmonotonic Classical Magnetoconductivity of a Two-Dimensional Electron Gas in a Disordered Array of Obstacles - Supplement

N. H. Siboni[1], J. Schluck[2], K. Pierz[3], H. W. Schumacher[3], D. Kazazis[4], J. Horbach[1], and T. Heinzel[2]

[1]*Institut für Theoretische Physik II, Heinrich-Heine-Universität,*
Universitätsstraße 1, 40225 Düsseldorf, Germany
[2]*Institut für Experimentelle Physik der kondensierten Materie,*
Heinrich-Heine-Universität, Universitätsstraße 1, 40225 Düsseldorf, Germany
[3]*Physikalisch-Technische Bundesanstalt, Bundesallee 100, 38116 Braunschweig, Germany*
[4]*CNRS-LPN, Route de Nozay, 91960 Marcoussis, France*
(Dated: January 22, 2018)

Here we present the measurement of the Hall resistitivities that enter the calculation of the conductivities as well as the temperature-dependent magnetoconductivies for all samples studied. Furthermore, a plot with a direct comparison between simulation and experiment of the diffusion constant as function of density at $B = 0$ is shown.
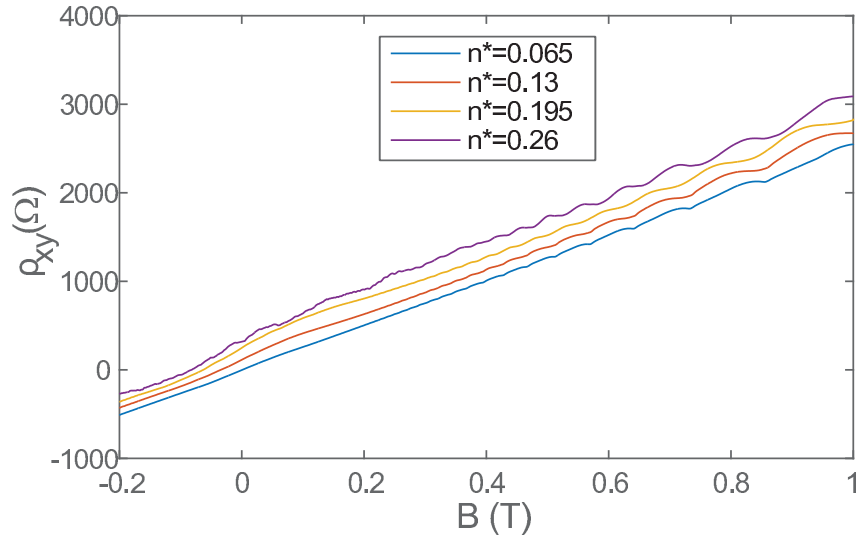
FIG. 1. (color online) Measurement of the Hall resistivites, which were used to calculate the respective conductivities. The traces are offset by $100\,\Omega$ with respect to each other for clarity. For stronger magnetic fields quantum Hall plateaus are formed.
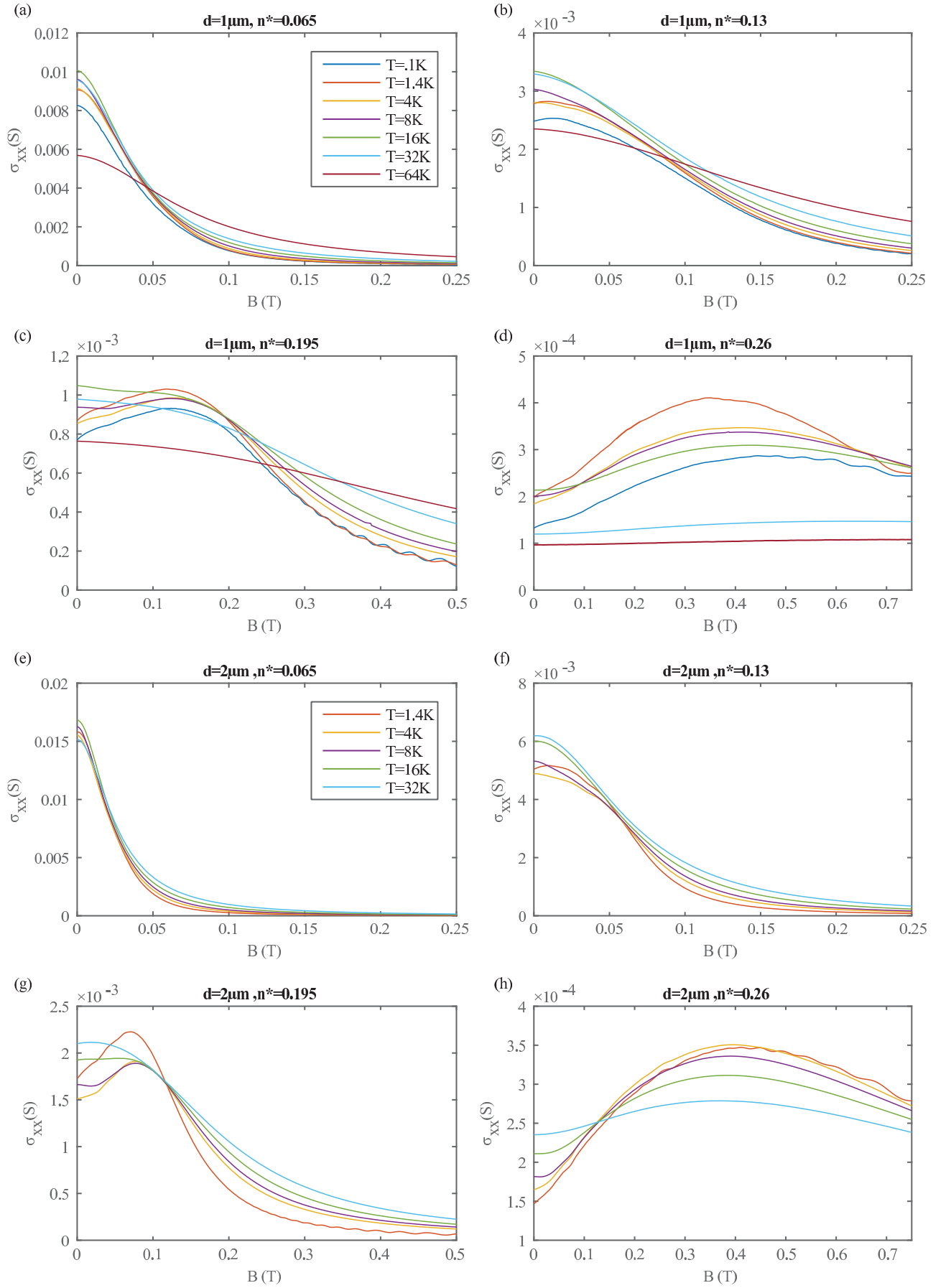
FIG. 2. (color online) Temperature dependence of the magnetoconductivity for all samples. (a)-(d) show the results for obstacles with a diameter of d = 1 μm. Note that the trace for T = 0.1 K was taken in a different cooldown from the others. (e)-(h) show the results for obstacles with a diameter of d = 2 μm.
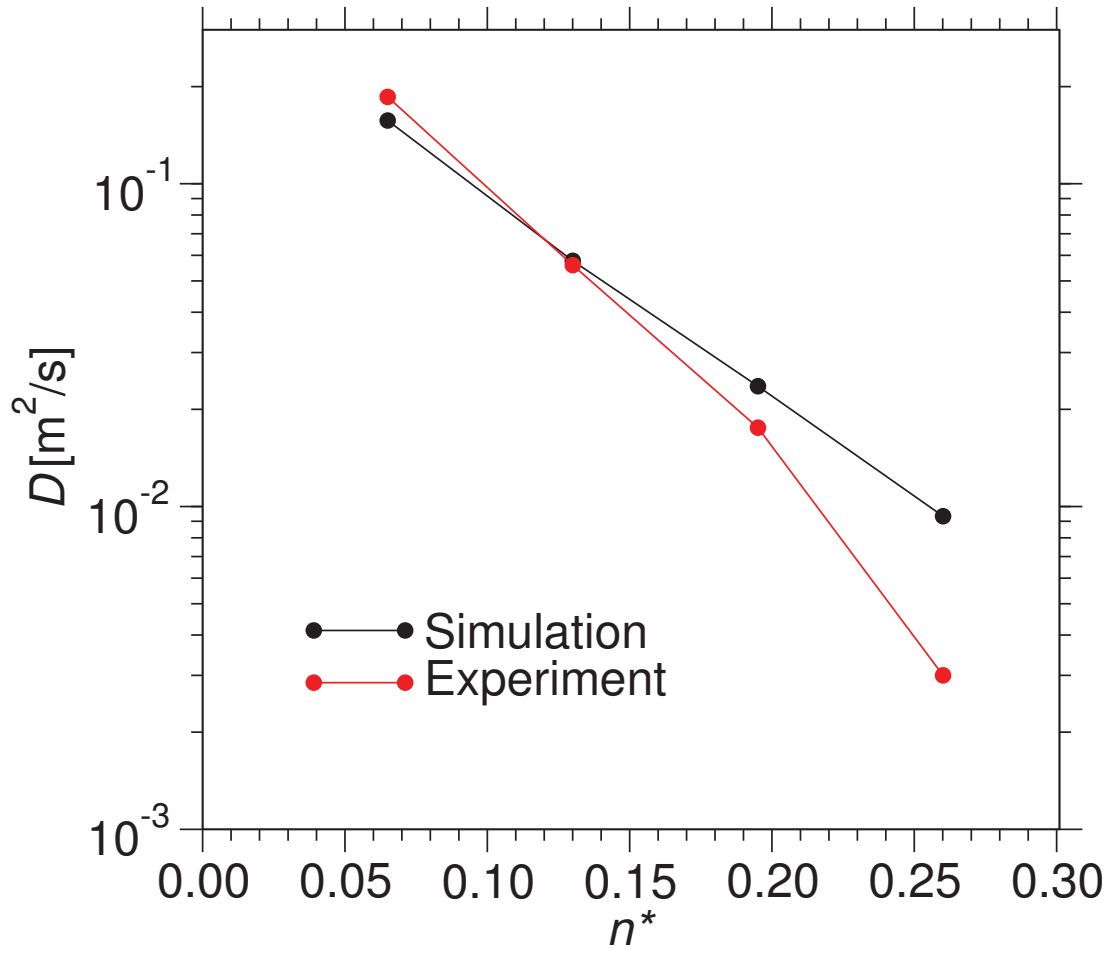
FIG. 3. Direct comparison between simulation and experiment of the diffusion constant as function of density $n^\star$ at zero magnetic field, $B = 0$.

Linear negative magnetoresistance in two-dimensional Lorentz gases

J. Schluck, M. Hund, T. Heckenthaler, and T. Heinzel*

Condensed Matter Physics Laboratory, Heinrich-Heine-Universität, D-40204 Düsseldorf, Germany

N. H. Siboni and J. Horbach

Institut für Theoretische Physik II, Heinrich-Heine-Universität, D-40204 Düsseldorf, Germany

K. Pierz and H. W. Schumacher

Physikalisch-Technische Bundesanstalt, Bundesallee 100, D-38116 Braunschweig, Germany

D. Kazazis† and U. Gennser and D. Mailly

C2N-CNRS and UPSud, Route de Nozay, 91460 Marcoussis, France
(Dated: December 14, 2017)

Two-dimensional Lorentz gases formed by obstacles in the shape of circles, squares and retrore-flectors are reported to show a pronounced negative, linear magnetoresistance at small magnetic fields. For circular obstacles at low number densities, our results agree with the predictions of a model based on classical retroreflection. In extension to the existing theoretical models, we find that the normalized magnetoresistance slope depends on the obstacle shape and increases as the number density of the obstacles is increased. The peaks are furthermore suppressed by in-plane magnetic fields as well as by elevated temperatures. These results suggest that classical retroreflection can form a significant contribution to the magnetoresistivity of two-dimensional Lorentz gases, while other contributions like weak localization cannot be excluded.

PACS numbers: 73.23.-b,73.40.-c

Reference

Copyright statement

Contributions

I designed the sample and contributed to sample preparation. I participated in the conduction of the experiments and the analysis of the experimental data. I contributed to manuscript writing.

Linear negative magnetoresistance in two-dimensional Lorentz gases

J. Schluck, M. Hund, T. Heckenthaler, and T. Heinzel*

Condensed Matter Physics Laboratory, Heinrich-Heine-Universität, D-40204 Düsseldorf, Germany

N. H. Siboni and J. Horbach

Institut für Theoretische Physik II, Heinrich-Heine-Universität, D-40204 Düsseldorf, Germany

K. Pierz and H. W. Schumacher

Physikalisch-Technische Bundesanstalt, Bundesallee 100, D-38116 Braunschweig, Germany

D. Kazazis† and U. Gennser and D. Mailly

C2N-CNRS and UPSud, Route de Nozay, 91460 Marcoussis, France
(Dated: February 21, 2018)

Two-dimensional Lorentz gases formed by obstacles in the shape of circles, squares and retro-reflectors are reported to show a pronounced linear negative magnetoresistance at small magnetic fields. For circular obstacles at low number densities, our results agree with the predictions of a model based on classical retroreflection. In extension to the existing theoretical models, we find that the normalized magnetoresistance slope depends on the obstacle shape and increases as the number density of the obstacles is increased. The peaks are furthermore suppressed by in-plane magnetic fields as well as by elevated temperatures. These results suggest that classical retroreflection can form a significant contribution to the magnetoresistivity of two-dimensional Lorentz gases, while contributions from weak localization cannot be excluded, in particular for large obstacle densities.

PACS numbers: 73.23.-b,73.40.-c

I. INTRODUCTION

The magnetoresistivity of two-dimensional electron gases defined in semiconductor heterostructures can show pronounced deviations from the behavior expected within the Drude-Boltzmann model, i.e. a constant longitudinal and a linear Hall magnetoresistivity. The deviations can be traced back to various origins. For example, the quantization of the cyclotron motion in a perpendicular magnetic field $B_\perp$ lies at the heart of the Quantum Hall effect and of the Shubnikov - de Haas oscillations in the longitudinal resistivity $\rho_{xx}(B_\perp)$,[1] while weak localization increases $\rho_{xx}(B_\perp)$ at $B_\perp = 0$, which decays in a characteristic, nonlinear way as $B_\perp$ is increased.[2] Weak localization also occurs in disordered arrays of classical scatterers as a consequence of an interplay between classical chaos and interference of the electron waves.[3,4] Interaction effects typically generate a relatively broad negative, approximately parabolic correction to $\rho_{xx}(B_\perp)$.[5] Within a hydrodynamic model that includes a B-dependent viscosity of the electron liquid, interactions have been used to explain the giant negative magnetoresistance (GNMR),[6] observed in two-dimensional electron gases with high electron mobilities.[7–11] One further possible origin of a negative magnetoresistance are memory effects. They are caused by time-independent components in the scattering potential which do not randomize the electron momentum in the sense of the relaxation time approximation and thus generate deviations from the Boltzmann expressions for the magnetoresistivities.[12] A suitable model system for studying memory effects, which have a classical character, is an electron gas exposed to a static,

Poisson-distributed array of identical obstacles. It was first proposed by Lorentz[13] and is therefore known as *Lorentz gas*. Two-dimensional Lorentz gases (2DLGs) are of particular interest since a perpendicular magnetic field has profound effects on their transport properties. Several theoretical studies on the magnetotransport properties of 2DLGs have been reported, which has resulted in the identification of various memory effects[14–19]. A prominent example are electrons that do not contribute to the longitudinal transport since they move forever in an undisturbed cyclotron orbit. For circular obstacles acting as scatterers at low number densities n_s, it has been shown that this memory effect causes an exponential decrease of ρ_{xx} as $B_\perp$ increases.[14,15] Such analytic expressions originate from kinematic models which require a dimensionless obstacle number density $n^\star = \frac{1}{4}n_s d_s^2$ to be small compared to 1. Here, d_s denotes the characteristic size of the scatterers. Extensions to larger number densities have been carried out numerically for circular obstacles, using molecular dynamics simulations. They have revealed that the conductivity as a function of $n^\star$ and $B_\perp$ forms a delocalized, conductive phase, which is sandwiched between two localized phases at low and at high obstacle densities.[20–22]

Of particular relevance to the present study are the works of Dmitriev et al.[18] and Cheianov et al.[19] on retroreflection in dilute 2DLGs with circular obstacles. This type of memory effect can be understood in terms of an electron that gets scattered at an obstacle by an angle close to π after having travelled a certain distance L ballistically. This distance is related to a two-dimensional corridor of area $L \times d_s$ which is free of obstacle centers, see Fig. 1

(a) for an illustration. After the electron has undergone backscattering, it probes the same corridor again which is still free of obstacles, due to the static character of the scattering potential. This memory term increases the resistance since any scattering event at time-dependent potentials in this corridor would give the electron a momentum component in forward direction. The overlap between the corridors related to the incoming and the backscattered electron trajectory (see Fig. 1 (a)) equals the area probed twice, and is thus a measure of this memory term. As $B_\perp$ is increased, this overlap decreases due to the Lorentz deflection. Consequently, $B_\perp$ suppresses this memory term and causes the resistance to decrease. Remarkably, this negative magnetoresistivity has been predicted to be *linear*.[18] Experiments by Gusev et al.[23] are in agreement with this prediction. Magnetotransport in 2DLGs formed by arrays of circular obstacles has been studied experimentally by Yevtushenko et al.[3], also at relatively low $n^\star$. The authors observe a negative magnetoresistance which they explain by *ballistic weak localization*. This takes into account correlations in the electronic motion as well as the classical character of the obstacles. Due to their much larger size than the Fermi wavelength, they do not split the wave functions in time-reversed backscattering paths as assumed within the conventional weak localization description. However, it has been argued later on that this phenomenology can also be explained by classical retroreflection.[18] Thus, the relevance of these two mechanisms, namely classical retroreflection and quantum mechanical ballistic weak localization, for the observed negative magnetoresistance of two-dimensional electron gases exposed to random arrays of classical obstacles is still an open question.

Here, we report magnetotransport measurements on 2DLGs composed of classical scatterers. We find an approximately linear negative magnetoresistivity close to $B_\perp = 0$. The dependencies of the peaks on the parameters shape and density of the obstacles, temperature as well as on in-plane magnetic field is reported. Our data suggest, in brief, that classical retroreflection does contribute significantly to the measured peaks while a contribution of ballistic weak localization cannot be excluded.

The paper is organized as follows. In Section II, we describe the sample preparation and the measurement setup. The experimental results are presented and interpreted in Section III. We end with a summary and conclusion in Section IV.

II. SAMPLE PREPARATION AND EXPERIMENTAL SETUP

A GaAs/Al$_{0.3}$Ga$_{0.7}$As heterostructure with a two-dimensional electron gas (2DEG) 150 nm below the surface is used. The pristine 2DEG has a density of $2.5 \times 10^{15}\,\mathrm{m}^{-2}$ and an electron mobility of $340\,\mathrm{m^2/Vs}$,

corresponding to a mean free path of $\ell = 31\,\mu\mathrm{m}$ at liquid helium temperatures. The quantum scattering time as determined from the envelope of the Shubnikov-de Haas oscillations[24] amounts to $\tau_q = 2.4\,\mathrm{ps}$ which gives a quantum scattering length of $\ell_q = 530\,\mathrm{nm}$. The Lorentz array is prepared by generating two sets of random numbers which define the x- and y-coordinates of the obstacle centers. The correct statistical properties of the arrays are checked by a Voronoi tessellation of the array, where each obstacle center defines a cell containing all points closer to this center than to any other, see Fig. 1 (b).
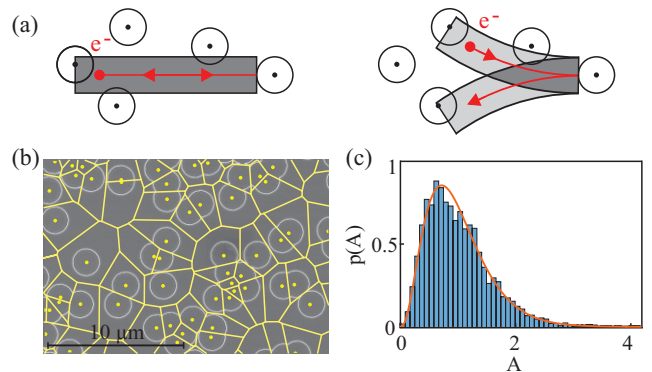

FIG. 1. (color online). (a) Illustration of the memory term caused by retroreflection at $B_\perp = 0$ (left) and $B_\perp > 0$ (right). The electron moves through the obstacles (circles) which define the ballistic corridors before and after backscattering (light gray, right), with their overlap area marked in dark gray. (b) Scanning electron micrograph of the 2DLG with circular obstacles of radius $d_s = 2\,\mu\mathrm{m}$ and $n_s = 1.95 \times 10^{11}\,m^{-2}$ ($n^\star = 0.195$). The obstacle centers and the corresponding Voronoi tessellation are shown as an overlay. (c) Histogram of the normalized Voronoi cell areas A for our arrays with number density $n_s = 1.95 \times 10^{11}\,m^{-2}$, and the fit (red curve) to the probability density function $p(A)$ as described in the text.

The probability density function $p(A)$ of the Voronoi cell areas has no known analytical expression, but can be well approximated by $p(A) = \frac{343}{15}\sqrt{7/2\pi}A^{2.5}e^{-3.5A}$, where A denotes the normalized cell area.[25] This expression provides excellent fits to our arrays for all obstacle densities, and the average value $\langle A \rangle = 1$ as well as the standard deviation $\sigma_A \approx \sqrt{2/7}$ are well reproduced, see Fig. 1 (c). The obstacles in one array have identical shapes (circles, squares and retroreflectors, see the insets in Fig. 2) and sizes characterized by a lateral extension $d_s = 1\,\mu\mathrm{m}$ and $2\,\mu\mathrm{m}$, respectively. Here, d_s is the diameter of the circles or the edge length of the squares and retroreflectors, respectively. For the implementation of an array, one shape is allocated with random orientation to each center coordinate by a pattern generator and then transferred to the samples by electron beam lithography and subsequent reactive ion etching. The etch depth of roughly 150 nm in all samples ensures depletion of the electron gas in the etched regions. An example of such an array is shown in Fig. 1 (b).

From Aharonov-Bohm experiments on comparable structures in large magnetic fields,[26], we estimate the lateral depletion length around the etched structure to $\approx 75\,\text{nm}$. Taking this depletion into account, the corresponding densities of the arrays of circles and retroreflectors are $n^\star = 0.065, 0.13, 0.195$ and 0.26, while for the arrays of squares, the densities are smaller by a factor of $\pi/4$. This choice of parameters ensures that on the one hand, the obstacle size is large compared to the Fermi wavelength of $\approx 50\,\text{nm}$ such that the scattering can be regarded as classical, while on the other hand, the resistivity of the arrays is dominated by the patterned obstacles. The mean free path of the Lorentz gas composed of circular disks in the dilute limit is given by $\ell_s = (n_s d_s)^{-1}$, corresponding to values below $8\,\mu\text{m}$ for all obstacle densities, significantly smaller than ℓ. Only the arrays with the smallest n_s values of $n_s = 6.5 \times 10^{10}\,\text{m}^{-2}$ can be considered as dilute, which defines the range of validity of the models mentioned above, i.e., in Refs. 14–19. Furthermore, the absolute number of obstacles varies between 975 and 20000 which should ensure reasonable ensemble averaging. All arrays are located in Hall bar structures and have a size of $100\,\mu\text{m} \times 200\,\mu\text{m}$. The insets in Fig. 2 illustrate the geometries of the individual obstacles. Measurements are carried out in the mixing chamber of a $^3\text{He}/^4\text{He}$ dilution refrigerator with a base temperature of $25\,\text{mK}$ and in a ^4He gas flow cryostat that can be operated at temperatures between $1.4\,\text{K}$ and $300\,\text{K}$. Both cryostats are equipped with superconducting solenoids and a rotatable sample stage. They are used for applying perpendicular magnetic fields $B_\perp$ as well as for in-plane components $B_\parallel$. An AC current (amplitude $500\,\text{nA}$, $17.7\,\text{Hz}$) is applied, and the magnetoresistance components $R_{xx}(B_\perp)$ and $R_{xy}(B_\perp)$ are measured via voltage probes using lock-in amplifiers.

III. EXPERIMENTAL RESULTS AND DISCUSSION

Figure 2 shows the measured longitudinal magnetoresistivities $\rho_{xx}(B_\perp)$ of the 2DLGs formed by circles ($d_s = 1\,\mu\text{m}$ and $2\,\mu\text{m}$) as well as by squares and retroreflectors with $d_s = 2\,\mu\text{m}$. A pronounced peak centered at $B_\perp = 0$ is observed in all samples which, for larger $n^\star$, extends well into the regime where Shubnikov- de Haas oscillations are visible. For small $B_\perp$, the magnetoresistivity within the peak is approximately linear and develops a nonlinear behavior as $B_\perp$ increases. Note that the resisivity of the arrays of squares with the largest $n^\star$ is significantly larger than that one of the circles at the same obstacle density. We attribute this to the fact that the array of squares is much closer to the percolation threshold of $n_c^\star = 0.246$ for the squares vs. 0.359 for the circles[27] (the percolation threshold for the arrays of retroreflectors has not been determined yet to the best of our knowledge). This may also explain the structures visible in the flanks of the peaks in these samples, since the

proximity to the percolation threshold makes the transport more sensitive to local details of the potential.

At first sight, the magnetoresistance peaks resemble those observed on pristine high-mobility 2DEGs, which are usually referred to as *giant negative magnetoresistance* (GNMR).[7–11] This structure, which is also present in our pristine samples, shows, besides a marked dependence on the width of the Hall bar,[28] the parametric dependencies as reported earlier: a rapid suppression as the temperature is increased to $1\,\text{K}$ as well as by parallel magnetic fields.[9,29] The amplitude of the GNMR structure in our samples is in the range of a few Ω only and thus negligible in the arrays containing artificial obstacles at all our obstacle number densities. Our data even suggest that already at our lowest obstacle density, the GNMR is strongly suppressed.[29] Furthermore, the dominant magnetoresistance peak observed in our samples does not depend significantly on in-plane B fields and is much more robust with respect to thermal smearing.

As $n^\star$ is increased, the linear part of the peak tends to get more pronounced and increases both in amplitude and width. For large obstacle densities, the amplitude of the corresponding conductance dip is in the range of $2e^2/h$, the maximum possible amplitude of weak localization. For low densities, however, the amplitude is significantly larger, reaching values as high as $\approx 50e^2/h$,[29] which excludes weak localization as the dominant origin. Furthermore, the peak is more prominent in the Lorentz gases formed by retroreflectors in comparison to those formed by circles and squares of size $2\,\mu\text{m}$. We have also measured arrays of squares and retroreflectors with $d_s = 1\,\mu\text{m}$ and found no significant differences to the corresponding arrays of circles.[29] We take this as an indication that for the obstacles with the smaller size, the geometric smearing of the obstacle shape by the lateral depletion is already significant and leads to a convergence of the scattering cross sections. In Fig. 3 (a), the temperature dependence of the peak is exemplified using the retroreflector array of density $n^\star = 0.195$. A qualitatively similar behavior is observed for the other arrays. As the sample is warmed from $25\,\text{mK}$ to $800\,\text{mK}$, the peak shape remains nearly unaffected while the Shubnikov-de Haas oscillations show thermal smearing. This can be seen as an indication that weak localization does not dominate the peak shape. As the temperature is increased to $8\,\text{K}$, the linear part of the peak, visible for magnetic fields below $30\,\text{mT}$ in this case, decays to zero amplitude. The background peak has a much weaker temperature dependence and is still clearly visible at $32\,\text{K}$.

The influence of in-plane magnetic fields $B_\parallel$ is shown in Fig. 3 (b), exemplified for the array of circles with with $d_s = 1\,\mu\text{m}$ and $n^\star = 0.195$. These data have been obtained by rotating the samples with respect to the fixed magnetic field by angles up to $\approx 1.4°$ around $\pi/2$, such that a change of the perpendicular component $B_\perp$ by $\pm 0.15\,\text{T}$ was reached under approximately constant $B_\parallel$ (changes of less than $2\,\text{mT}$). The peak is suppressed as $B_\parallel$ is increased and remains barely visible at $B_\parallel = 12\,\text{T}$.
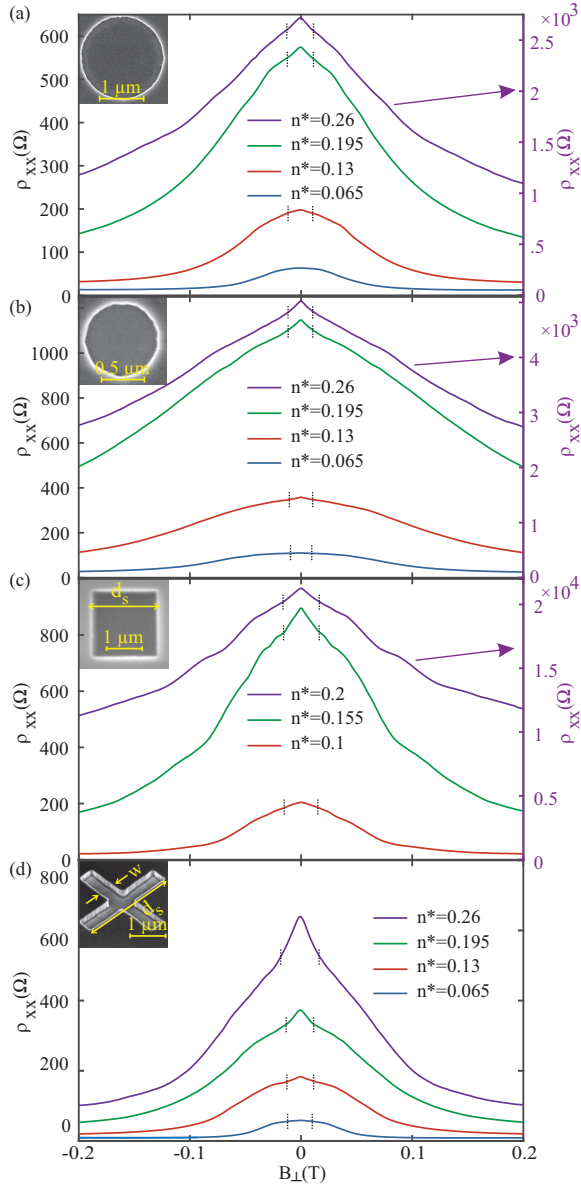
FIG. 2. (color online). Longitudinal magnetoresistance of the 2DLGs with various obstacle densities $n^\star$ for circles with $d_s = 2\,\mu$m (a) and $1\,\mu$m(b), squares with $d_s = 2\,\mu$m (c) and retroreflectors with $d_s = 2\,\mu$m (d). The interval of the linear regime is indicated by the dashed, vertical lines. Scanning electron electron microscope pictures of the corresponding obstacles that form the arrays are shown in the insets. The temperature was $1.4\,$K in all measurements.

FIG. 3. (color online). (a) Temperature dependence of R_{xx} for the array formed by retroreflectors with a density of $n^\star = 0.195$ and $d_s = 2\,\mu$m. (b) Effect of in-plane magnetic fields on the magnetoresistivity, for the array of circles with $d_s = 1\,\mu$m and $n^\star = 0.195$. The traces are offset by $50\,\Omega$ each for clarity.

In order to narrow down the character of this peak further, we have carried out molecular dynamics simulations for an array formed by circles with $d_s = 1\,\mu$m and $n^\star = 0.225$. The electrons and scatterers interact via a standard shifted, purely repulsive Weeks-Chandler-Andersen (WCA) potential, $u(r) = 4\varepsilon \left[(r_s/r)^{12} - (r_s/r)^6 + 1/4 \right]$ for $r < 2^{1/6} r_s$ and $u(r) = 0$ otherwise. Here, we have set the energy parameter to $\varepsilon = 0.1 E_F$. We use 100 statistically independent matrix structures. Newton's equa-
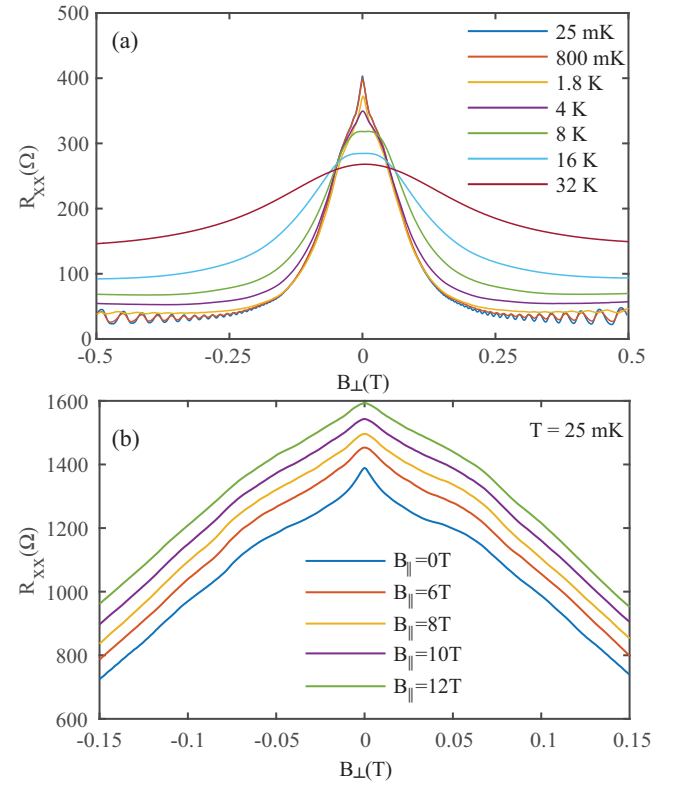
tions of motion are integrated using the velocity-Verlet algorithm[30] with a time step of $10^{-3} t_0$ with t_0 being the time an electron needs to travel ballistically the distance d_s, i.e. $t_0 = 9.23\,$ps for our samples. All electrons move with the Fermi velocity in regions where $u = 0$. At each magnetic field, 2400 electrons are used for runs of $10^6 t_0$ duration. In Fig. 4, the result of such a model calculation is shown. Both features of the magnetoresistance, namely the broad shoulder and the smaller, approximately linear peak close to $B_\perp = 0$, are reproduced. The linear regime extends up to $B_\perp \approx 30$mT, which is of the same order of magnitude as observed experimentally for comparable parameters. A linear negative magnetoresistivity is also obtained in corresponding simulations for lower $n^\star$ (not shown). These model calculations demonstrate that classical effects can generate the measured structure also in the regime of large obstacle densities and justifies its discussion in terms of memory effects.

We attribute the broad background component of the peak predominantly to undisturbed cyclotron motion of electrons in between the obstacles.[15] This structure is of no further interest here. Rather, we focus on the approximately linear peak close to $B_\perp = 0$. As mentioned in the Introduction, theoretical studies were carried out for low obstacle densities,[18] showing that retroreflection causes
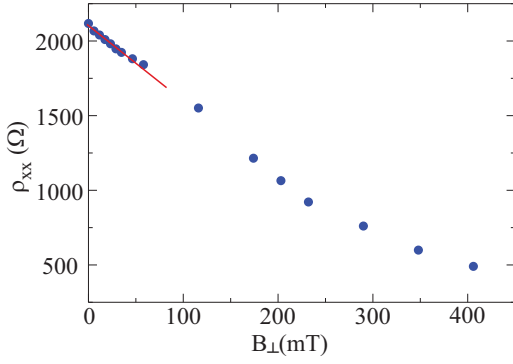
FIG. 4. (color online). Result of a model simulation (blue circles) of $\rho_{xx}(B)$ for a 2DLG formed by an array of circles ($d_s = 1\,\mu$m and $n^\star = 0.225$). The red line shows a linear approximation of the data points at the seven lowest magnetic fields ($B \leq 34\,$mT).

the resistance to decrease linearly as a function of $B_\perp$ in the regime $\omega_c\tau_s \lesssim 0.2$ where ω_c denotes the cyclotron frequency and τ_s the obstacle-generated scattering time, i.e. $\tau_s = (n_s d_s v_F)^{-1}$ with the Fermi velocity v_F. Here, d_s takes the role of the total scattering cross section for circles. These results have been derived for the limit of low obstacle densities, characterized by $d_s \ll \ell_s$ with the obstacle-dominated mean free path of $\ell_s = v_F\tau_s$. Interestingly, the normalized slope α of $\rho_{xx}(\perp)$, defined as

$$\alpha \equiv \frac{1}{\rho_{xx}(0)\tau_s}\frac{d(\delta\rho_{xx}(B_\perp))}{d\omega_c} \tag{1}$$

is independent of the obstacle density in this regime and has a value which is characteristic for the obstacle shape. For circular obstacles, $\alpha_\circ = -0.04$ has been reported,[18] while to the best of our knowledge, other shapes have not yet been considered in this context. The numerical studies have shown that such a linear magnetoresistivity is still to be expected at relatively large obstacle densities of $n^\star \approx 0.05$. These results are in agreement with the experiments of Gusev et al. in Ref. 23. The fact that the obstacle positions were not random but showed Gaussian deviations from a periodic arrangement is of minor relevance in that context, since at low obstacle densities, retroreflection is a single-obstacle process.

In Fig. 5(a), we show the normalized magnetoresistivities for the arrays presented in Fig. 2. Here, we have followed Ref. 18 and determined the scattering times according to $\tau_s = (n_s \sigma_s v_F)^{-1}$, where σ_s is the total scattering cross section of one obstacle, i.e. $\sigma_{s,\circ} = d_s$, $\sigma_{s,\square} = \frac{4d_s}{\pi}$ and $\sigma_{s,\times} = \frac{2}{\pi}\left[(2-\sqrt{2})w + \sqrt{2}d_s\right] \approx 0.98d_s$, where w denotes the width of the retroreflector bars (see also Fig. 2), in our case $w = 0.45\,\mu$m for the samples with $d_s = 2\,\mu$m and $w = 0.3\,\mu$m for the samples with $d_s = 1\,\mu$m, respectively. A linear regime is found for all arrays, with an interval of varying size, extending up to $\omega_c\tau_s \approx 0.4$, 0.5 and 0.9 for the arrays of retroreflectors, squares and circle with $d_s = 2\,\mu$m, respectively. The ar-
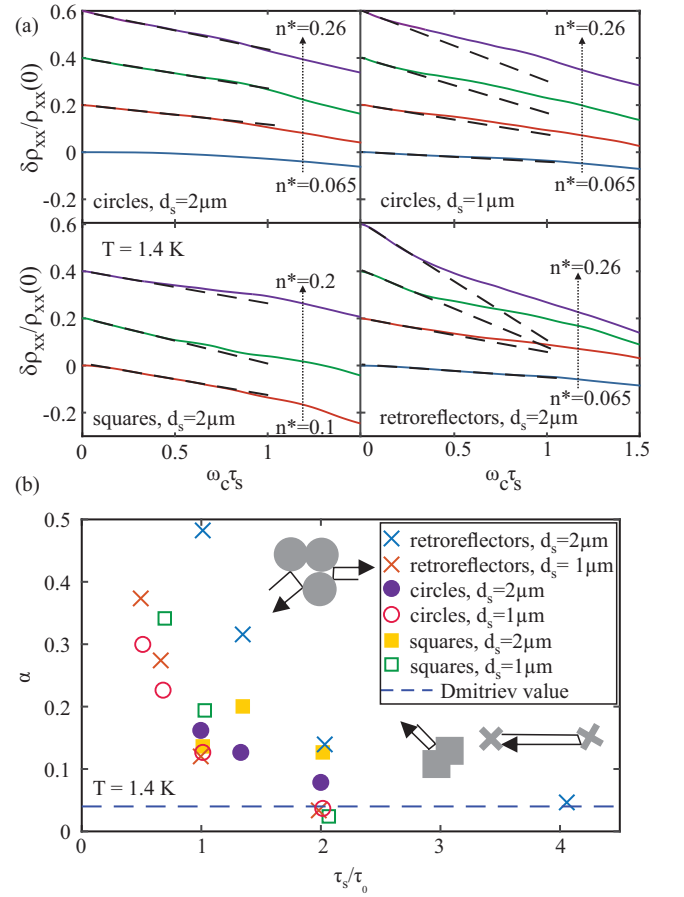

FIG. 5. (color online). (a) Experimentally determined normalized magnetoresistivity of the studied arrays and the corresponding linear fits for the different arrays. The traces at larger $n^\star$ are vertically offset by 0.2 for clarity. (b) Normalized slopes α of the normalized linear negative magnetoresistivities as a function of $n^\star$. The inset shows exemplified retroreflected trajectores at clusters of circles and squares, as well as a bound trajectory in a resonator formed by two retroreflectors. All data have been obtained for $T = 1.4\,$K.

ray formed by circles with $d_s = 1\,\mu$m shows a smaller interval, with an upper limit of $\omega_c\tau_s \approx 0.2$. This is in rough agreement with the interval sizes of $\omega_c\tau_s \approx 0.2$ found in numerical simulations for the dilute case,[18,19] as well as with the results of our molecular dynamics simulations, see Fig. 4. Within the retroreflection picture, it corresponds the the magnetic field where the overlap between the ballistic corridors of injected and retroreflected electrons becomes insignificant.

The values of α are plotted as a function of the scattering times in Fig. 5(b). Here, τ_0 denotes the time the electron needs to move ballistically the distance d_s, i.e. $\tau_0 = 4.3\,$ps for $d_s = 1\,\mu$m and $\tau_0 = 8.6\,$ps for $d_s = 2\,\mu$m. As τ_s/τ_0 reaches values af 2 or above, α is comparable to the value of 0.04 as predicted theoretically for the dilute case.[18] For all obstacle shapes, α increases as τ_s is decreased. This increase is largest for the retroreflectors

with $d_s = 2\,\mu$m, reaching a value as high as $\alpha_\times = 0.48$ for the sample with $n^\star = 0.26$.

These observations are interesting in two respects. First of all, they represent an experimental verification of the suggestion by theory that α is a measure of the retrore-flectivity of the individual obstacle. While our data do not show a clear difference in this respect between circles and squares, α is enhanced for the retroreflectors with $d_s = 2\,\mu$m in comparison to the arrays of circles and squares of the same size. Second, if α is interpreted this way, our data suggest that the retroreflectivity increases with increasing obstacle density. We are not aware of any theoretical work in relation to this issue, but provide a simple geometrical interpretation, illustrated in the inset of Fig. 5(b). As $n^\star$ increases, the probability of finding two obstacles close together or even overlapping increases as well. This leads to additional backscattering (in the sense of Ref. 18) when the corridor of the incoming electron overlaps with that one of an outgoing electron after multiple reflections at more than one obstacle, i.e., for spatial separations of the two trajectories smaller than d_s. The contribution of this effect could be tested by future studies on arrays with increased obstacle density but with a different spatial distribution statistics, for example by excluding overlaps or by periodic arrays with large Gaussian disorder. In addition, in particular for the retroreflector arrays, the formation of random res-onators that localize electrons in between two obstacles will increase as the scatterer density increases. Electrons may scatter into or out of such resonators by random background scattering on phonons or residual impurities. A clarification of how these effects contribute quantita-tively to α requires extensive theoretical studies that are beyond the scope of this work.

In Fig. 6, the dependencies of α on the temperature and on in-plane magnetic fields $B_\parallel$ are shown. We ob-serve that in general, α decays as T is increased and van-ishes at a temperature of about $8\,$K. Among other effects like thermal smearing, this may originate from acoustic phonons that scatter the electrons off the ballistic corri-dors, thereby decreasing their length. This is in tune with our observation that the mean free path ℓ decreases from $31\,\mu$m at $25\,$mK to $20\,\mu$m at $8\,$K, the largest temperature where the peak can still be analyzed. Yevtushenko et al.[3] have reported a much weaker temperature dependence of the corresponding peak in their arrays, which remained visible up to temperatures of $44\,$K. This may be due to the significantly smaller obstacle sizes of $d_s \approx 200\,$nm in those arrays, as well as due to the possible domination of these peaks by ballistic weak localization. Further-more, in Ref. 3, the conductivity amplitude of this peak is studied as a function of temperature, which lead to its interpretation in terms of ballistic weak localization with the Ehrenfest and the dephasing times as character-istic time scales.[31] In our data, such an analysis is ham-pered by the gradual and temperature dependent transi-tion between the linear and the background peak, which impedes a meaningful subtraction of some background
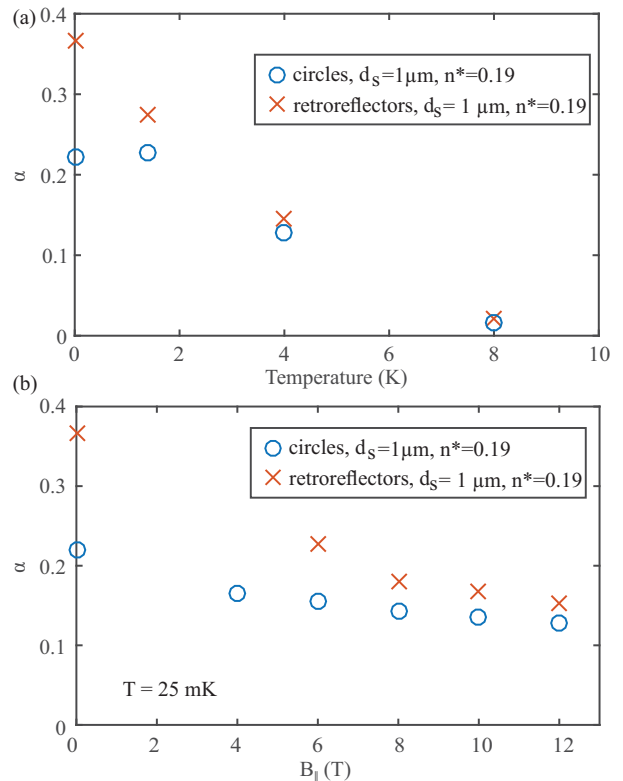

FIG. 6. (color online). Dependence of α on the temperature (a) and on in-plane magnetic fields $B_\parallel$ (b), exemplified by two arrays (see Fig. 3 for examples of the raw data).

conductance.

A decrease of α is also observed as a function of increas-ing $B_\parallel$, see Fig. 6 (b). For the retroreflectors, a rapid suppression of the peak is observed as $B_\parallel$ is increased from zero to $\approx 8\,$T, while at a further increase of $B_\parallel$, the suppression is less pronounced. For the circles, the sup-pression of the peak by $B_\parallel$ is weaker. Also, the α values of different obstacle shapes tend to converge towards sim-ilar values at large in-plane magnetic fields. In relation to the well-known suppression of the conventional weak localization peak[2], it has been established that due to the diamagnetic shift, the increase of the electron density of states and the modification of electron wave functions, the electrons develop a larger sensitivity to the rough-ness of the $GaAs - Al_xGa_{1-x}As$ interface which causes a reduction of the mean free path.[32] Also, $B_\parallel$ is known to deform the cyclotron orbits in a characteristic way.[33] In the pristine 2DEG, we observe a decrease of ℓ from $31\,\mu$m at $B_\parallel = 0$ to $16\,\mu$m at $B_\parallel = 12\,$T, which demon-strates that in fact a process is active which suppresses the mobility in parallel magnetic fields. This effect leads to a modified overlap of the incoming and reflected cor-ridors. A model for the effect of in-plane magnetic fields on retroreflection is presently not available. However, it appears plausible that the additional scattering gen-erated by $B_\parallel$ also reduces the extension of the ballistic

corridors, thereby suppressing the retroreflection. The observed convergence of the α values for different obstacle shapes as $B_\parallel$ is increased is in tune with this picture, considering that $B_\parallel$ effectively shortens the ballistic corridor and thus reduces the relevance of the obstacle-specific reflectivity.

All results presented above are influenced not only by the artificial array of obstacles, but also by the background disorder. Effects of background disorder on memory effects have been discussed so far, to the best of our knowledge, only in relation to the depinning of electrons from single obstacles or obstacle clusters.[34] The small-angle (quantum) scattering time of τ_q implies that the electrons undergo a random scattering event after travelling an average distance of $\ell_q = 530\,\mathrm{nm}$ in our samples. These small deflections can scatter the electrons out of the retroreflection corridor, thereby limiting its length. Thus, small-angle scattering may contribute to our observation that retroreflection is more visible in arrays with larger obstacle density where the ballistic corridors are shorter. A quantitative description of these effects are beyond the scope of the present manuscript and requires extensive numerical simulations. However, since we expect that quite a few small-angle deflections will be necessary to remove the electron from the reflective corridor, the electrons will still probe a significant fraction of the overlap of the corridors for the incoming and the reflected electron, namely over a length scale comparable to the distance between the artificial obstacles.

It should be noted that a parabolic magnetoresistivity has been predicted for very small magnetic fields as a consequence of memory effects.[19] For our samples, the upper magnetic field limit for this interval is of the order of $100\,\mu\mathrm{T}$ and thus not resolvable in the measurements reported here. Furthermore, for $\omega_c\tau_s \ll n_s d_s^2$, a $B_\perp^{-1/2}$ - dependence has been predicted.[19] We do not find such a dependence in any of our samples. This could be due to the relatively large values of $n^\star$ in our samples, or a consequence of distortions by residual background scattering.[34]

We end this Section by returning to the GNMR effect and its relation to our measurements. Typical GNMR data show a broad peak in $\rho_{xx}(B_\perp)$ with the phenomenology as described above, plus a small peak close to $B_\perp = 0$ on top, which has been attributed to sparse oval defects that act as Lorentz array and shows a remarkable robustness with respect to elevated temperatures[8] as well

as to in-plane magnetic fields[8,29]. Within this picture, it would thus correspond to the broad maximum we observe in our 2DLGs. On the other hand, the small peak we interpreted in terms of retroreflection is not resolved in the GNMR measurements.

IV. SUMMARY AND CONCLUSIONS

A linear negative magnetoresistance is observed in two-dimensional Lorentz gases in the classical regime, in qualitative agreement with both the predicted magnetoresistivity due to retroreflection at the obstacles at small scatterer densities and a numerically calculated classical magnetoresistivity at large scatterer densities. It can be concluded that retroreflection, one member of the family of classical memory effects, is the dominant origin of this peak in our samples. A comprehensive phenomenology of this peak has been presented, including its dependence on the density and shape of the obstacles, on the temperature as well as on in-plane magnetic fields. The measurements confirm the existing theory which has focused on circular-shaped obstacles in the low density regime. However, the normalized slope α of the magnetoresistance decreases as the temperature or the in-plane magnetic field is increased and increases with a larger density or retroreflectivity of the obstacles. These results cannot be understood within the presently available models. We have tentatively explained the behavior of α as a function of the obstacle density in terms of additional retroreflection that emerges due to the formation of clusters and/or resonators by the obstacles. Although our molecular dynamics simulations suggest that retroreflection does contribute to the experimentally observed structure, we cannot exclude an additional contribution by ballistic weak localization, which however would be non-negligible only for arrays with large obstacle densities. A further clarification would require theoretical work that extends to larger obstacle densities and includes the effects of the obstacle shape as well as of in-plane magnetic fields.

V. ACKNLOWLDEGEMENTS

* thomas.heinzel@hhu.de
† Present address: Laboratory for Micro- and Nanotechnology, Paul Scherrer Institute, 5232 Villigen-PSI, Switzerland
[1] K. von Klitzing, G. Dorda, and M. Pepper, Phys. Rev. Lett. **45**, 494 (1980).
[2] B. L. Altshuler, A. G. Aronov, and D. E. Khmelnitsky, J. Phys. C **15**, 7367 (1982).

[3] O. Yevtushenko, G. Lütjering, D. Weiss, and K. Richter, Phys. Rev. Lett. **84**, 542 (2000).
[4] I. L. Aleiner and A. I. Larkin, Phys. Rev. B **54**, 14423 (1996).
[5] M. A. Paalanen, D. C. Tsui, and J. C. M. Hwang, Phys. Rev. Lett. **51**, 2226 (1983).
[6] P. S. Alekseev, Phys. Rev. Lett. **117**, 166601 (2016).

[7] V. Umansky, R. de Picciotto, and M. Heiblum, Appl. Phys. Lett. **71**, 683 (1997).

[8] L. Bockhorn, P. Barthold, D. Schuh, W. Wegscheider, and R. J. Haug, Phys. Rev. B **83**, 113301 (2011).

[9] A. T. Hatke, M. A. Zudov, J. L. Reno, L. N. Pfeiffer, and K. W. West, Phys. Rev. B **85**, 081304(R) (2012).

[10] L. Bockhorn, I. V. Gornyi, D. Schuh, C. Reichl, W. Wegscheider, and R. J. Haug, Phys. Rev. B **90**, 165434 (2014).

[11] Q. Shi, P. D. Martin, Q. A. Ebner, M. A. Zudov, L. N. Pfeiffer, and K. W. West, Phys. Rev. B **89**, 201301(R) (2014).

[12] A. D. M. A. Dmitriev, D. G. Polyakov, and M. A. Zudov, Rev. Mod. Phys. **84**, 1709 (2012).

[13] H. Lorentz, Proc. R. Acad. Sci. Amsterdam **7**, 438 (1905).

[14] E. M. Baskin, L. N. Magarill, and M. V. Entin, Sov. Phys. JETP **48**, 365 (1978).

[15] A. V. Bobylev, F. A. Maaø, A. Hansen, and E. H. Hauge, Phys. Rev. Lett. **75**, 197 (1995).

[16] A. D. Mirlin, D. G. Polyakov, F. Evers, and P. Wölfle, Phys. Rev. Lett. **87**, 126805 (2001).

[17] D. G. Polyakov, F. Evers, A. D. Mirlin, and P. Wölfle, Phys. Rev. B **64**, 205306 (2001).

[18] A. Dmitriev, M. Dyakonov, and R. Jullien, Phys. Rev. Lett. **89**, 266804 (2002).

[19] V. V. Cheianov, A. P. Dmitriev, and V. Y. Kachorovskii, Phys. Rev. B **68**, 201304 (R) (2003).

[20] A. Kuzmany and H. Spohn, Phys. Rev. E **57**, 5544 (1998).

[21] W. Schirmacher, B. Fuchs, F. Höfling, and T. Franosch, Phys. Rev. Lett. **115**, 240602 (2015).

[22] N. H. Siboni, J. Schluck, K. Pierz, H. W. Schumacher, D. Kazazis, J. Horbach, and T. Heinzel, Phys. Rev. Lett. **120**, 056601 (2018).

[23] G. M. Gusev, P. Basmaji, Z. D. Kvon, L. V. Litvin, Y. Nastaushev, and A. I. Toropov, J. Phys. Cond. Mat. **6**, 73 (1994).

[24] T. Ando, J. Phys. Soc. Jpn. **37**, 1044 (1974).

[25] J. Ferenc and Z. Neda, Physica A **385**, 518 (2007).

[26] J. Schluck, S. Fasbender, T. Heinzel, K. Pierz, H. W. Schumacher, D. Kazazis, and U. Gennser, Phys. Rev. B **91**, 195303 (2015).

[27] S. Mertens and C. Moore, Phys. Rev. E **86**, 061109 (2012).

[28] R. G. Mani, A. Kriisa, and W. Wegscheider, Scientific Reports **3**, 02747 (2013).

[29] See Supplemental Material at [URL will be inserted by publisher] for details.

[30] K. Binder, J. Horbach, W. Kob, W. Paul, and F. Varnik, J. Phys. Cond. Mat. **16**, S429 (2004).

[31] A. Altland, P. W. Brouwer, and C. Tian, Phys. Rev. Lett. **99**, 036804 (2007).

[32] G. M. Minkov, O. E. Rut, A. V. Germanenko, A. A. Sherstobitov, B. N. Zvonkov, V. I. Shashkin, O. I. Khrykin, and D. O. Filatov, Phys. Rev. B **70**, 035304 (2004).

[33] N. M. Sotomayor-Choque, G. M. Gusev, J. R. Leite, A. A. Bykov, L. V. Litvin, N. T. Moshegov, A. I. Toropov, D. K. Maude, and J. C. Portal, Phys. Rev. B **66**, 035324 (2002).

[34] A. D. Mirlin, E. Tsitsishvili, and P. Wölfle, Phys. Rev. B **63**, 245310 (2001).

Linear negative magnetoresistance in two-dimensional Lorentz gases

J. Schluck, M. Hund, T. Heckenthaler, and T. Heinzel*

Condensed Matter Physics Laboratory, Heinrich-Heine-Universität, D-40204 Düsseldorf, Germany

N. H. Siboni and J. Horbach

Institut für Theoretische Physik II, Heinrich-Heine-Universität, D-40204 Düsseldorf, Germany

K. Pierz and H. W. Schumacher

Physikalisch-Technische Bundesanstalt, Bundesallee 100, D-38116 Braunschweig, Germany

D. Kazazis[†] and U. Gennser and D. Mailly

C2N-CNRS and UPSud, Route de Nozay, 91460 Marcoussis, France

(Dated: February 21, 2018)

This supplement provides additional information in relation to the giant magnetoresistance (GNMR) in the samples under study as well as the raw data of the magnetoresistivities and magnetoconductivities that are not shown in the main text.
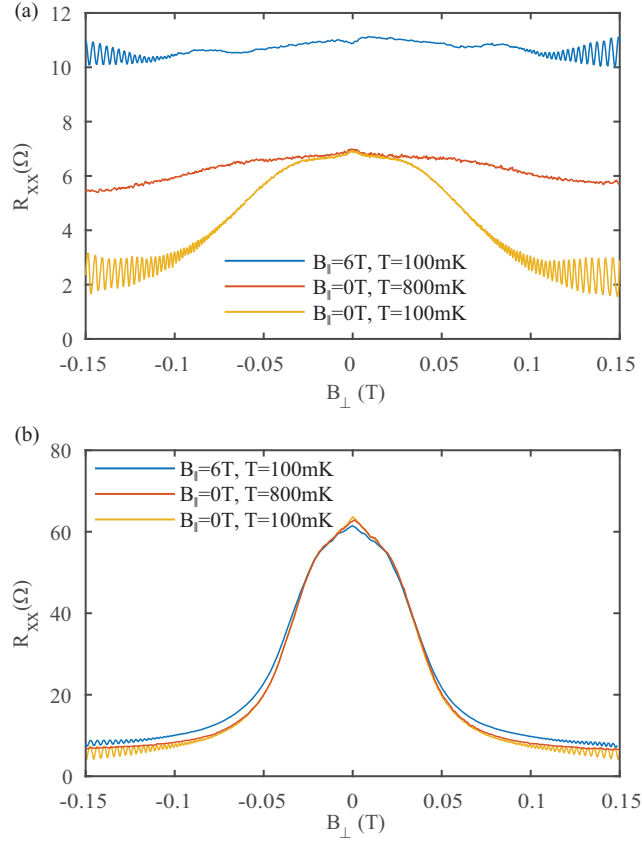
FIG. 1. (color online) Magnetoresistivity of the pristine 2DEG used for all 2DLG experiments. The typical features of the giant negative magnetoresistance are observed, namely a strong and broad peak with a much smaller peak on top, both centered at $B_\perp = 0$. The broad peak decays rapidly as the temperature is increased, while the small peak on top is more robust. Moreover, both peaks are suppressed by moderate in-plane magnetic fields $B_\parallel$. In (b), the corresponding measurements for the 2DLG formed by circles with $d_s = 2\,\mu$m and $n^\star = 0.065$ are shown. Its resistivity is about one order of magnitude larger, and the weak temperature dependence between $100\,$mK and $800\,$mK indicates that the disorder has already suppressed the GNMR contribution. Also, both components of the peak are quite robust with respect to in-plane magnetic fields.

[*] thomas.heinzel@hhu.de
[†] Present address: Laboratory for Micro- and Nanotechnology, Paul Scherrer Institute, 5232 Villigen-PSI, Switzerland
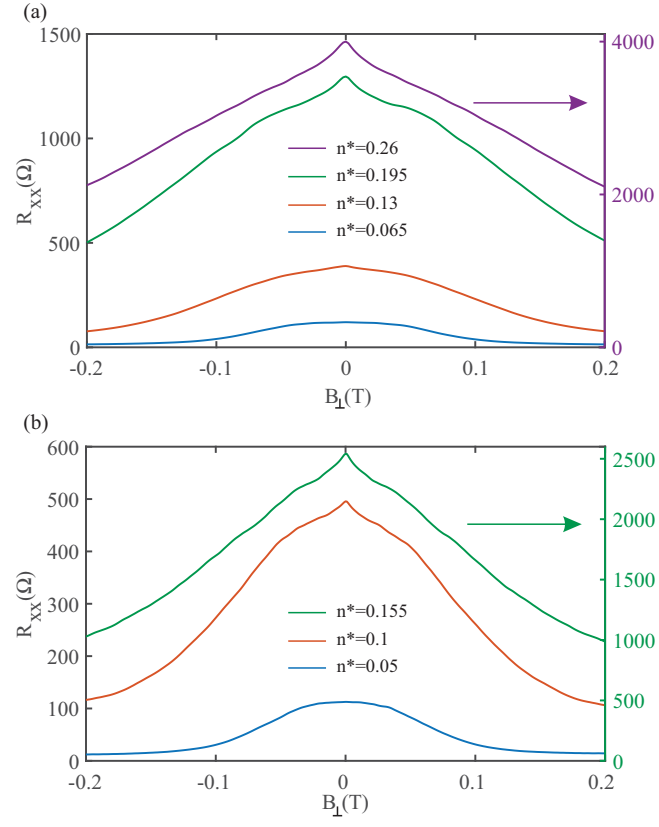
FIG. 2. (color online) Magnetoresistances of the 2DLGs formed by crosses (a) and squares (b), both with $d_s = 1\,\mu$m, measured at a temperature of $1.4\,$K.
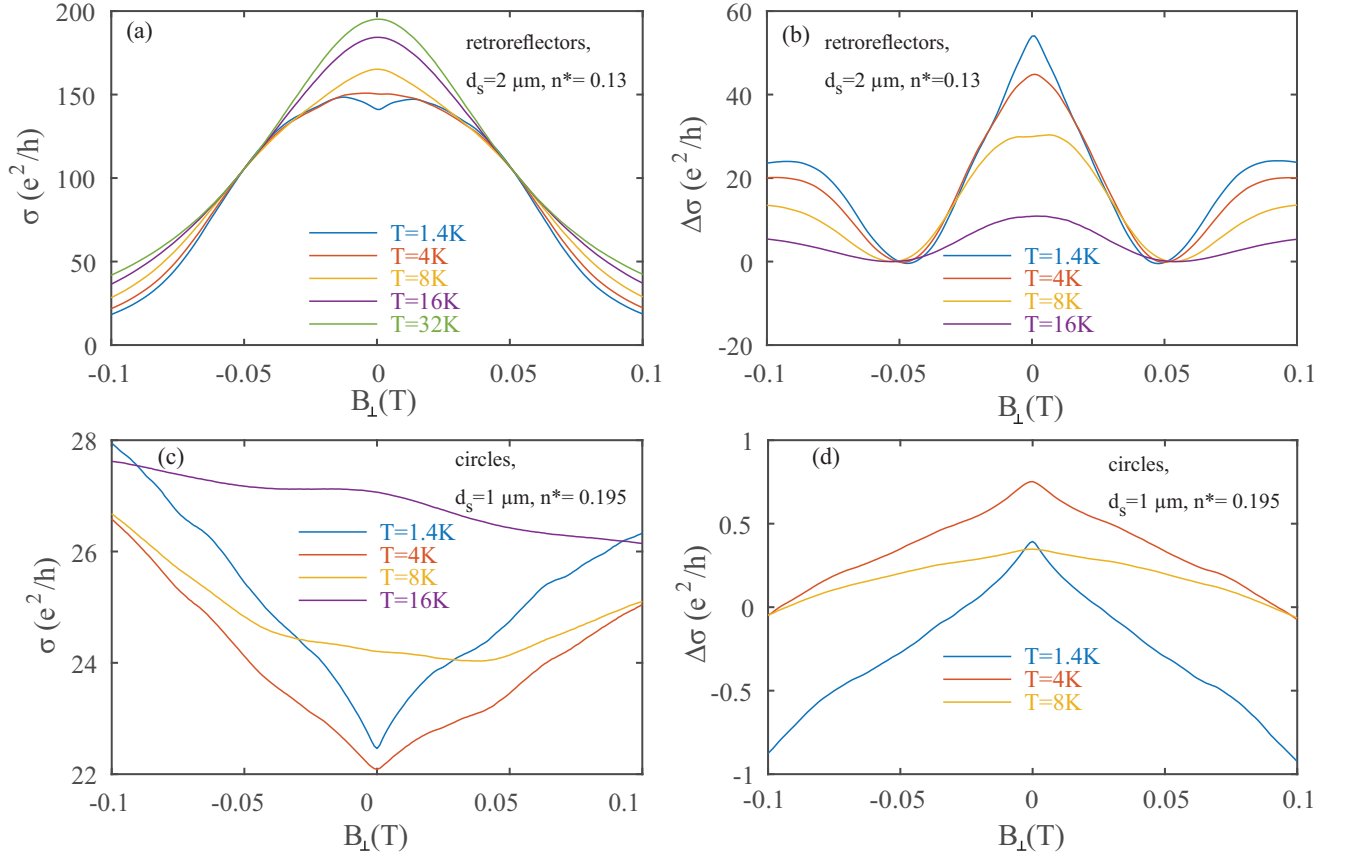
FIG. 3. (color online) Examples of the longitudinal magnetoconductivities $\sigma(B_\perp)$ as calculated from the measured magnetoresistivities for the arrays of retroreflectors with $n^\star = 0.13$, $d_s = 2\,\mu$m (a) and of circles with $n^\star = 0.195$, $d_s = 1\,\mu$m (c). The amplitude of the magnetoconductivity peak is estimated by removing the magnetoconductivity measured at $32\,$K in (a) and at $16\,$K in (c), respectively from all data obtained at lower temperatures. The corresponding conductivity differences are shown in (b) and (d). While the amplitude is of the order of e^2/h in the arrays of circles with lare $n^\star$, it is much larger in the array of retroreflectors with small $n^\star$.

4 Conclusion and outlook

Within this thesis, we discussed several aspects of classical electron transport. The main results are briefly summarized here and potential consecutive research projects are presented.

First we discussed the properties of single magnetic barriers. We could experimentally demonstrate, how a ballistic effect impedes Hall magnetometry in such structures and how this problem can be overcome using classical numerical simulations [103]. Naturally, one could now try to vary the shape of the magnetic profile, but it might be more interesting to instead study the effects of electrostatic potentials. Consider the case of a depletion zone introduced into the center of a Hall cross. Certainly this should also modify the Hall resistance in the ballistic case. This can now be used to generate a better understanding of the precise potential shape of the depletion zone, since it might be possible to distinguish e.g. between soft and hard potentials. Knowledge about this would in turn be very useful in setting up numerical simulations for other transport experiments and interpreting experiments in general.

By superimposing a homogeneous offset magnetic field anti-parallel to the magnetic barrier profile, we observed a series of commensurability oscillations, which we interpreted as snake-orbit resonances with the help of numerical simulations [110]. It would be interesting to include spin effects in these simulations and see if, by choosing appropriate dimensions, spin-filtering can be achieved within these structures.

The second building block of this thesis comprised the study of lateral superlattices. We discovered a regime in antidot lattices, where quantum oscillations coexisted over a wide range with the conventional commensurability oscillations [192]. By tracking their relative phase to the quantum Hall effect and with the help of quantum numerical simulations we could trace back their origin to the coexistence of hopping- and band-transport in these lattices. There is an interesting prediction about the influence of hard-walls on semi-classical electron transport, where it is stated, that the walls can influence the electronic phase, without affecting the electron trajectory [244]. An experimental verification has not been undertaken to date, but it might be possible to observe this effect in transport in antidot lattices or billiard-like systems.

The second superlattice we studied was a novel type of magneto-electric hybrid lattice, combining a two-dimensional square antidot lattice with a one-dimensional ferromagnetic stripe lattice [193]. In the case of zero magnetic mean field, we could show the emergence of pronounced resistance oscillations as a function of the stripe magnetization. We linked their origin to the existence of commensurate snake

trajectories. Preliminary experiments on this system in perpendicular magnetic fields showed a drastic modulation of the commensurability oscillations expected for the cases of the singular lattices. However, no conclusive picture about the nature of the underlying transport phenomena could be obtained and is left for further studies. Similarly, experiments in tilted magnetic fields proved to show interesting transport features, but an understanding could not yet be reached.

Finally, we studied controlled experimental realizations of a two-dimensional Lorentz gas in a magnetic field. We could experimentally verify the existence of a numerically predicted [41] maximum in conductivity for finite magnetic fields [234]. With the help of classical molecular dynamics simulations we could relate this maximum to a qualitative change in the electron transport mechanism. It can be interpreted as a signature of the two metal-insulator transitions present in the phase-diagram of the Lorentz gas. Furthermore, we demonstrated how the low-field magnetoresistance is influenced by the shape of the artificially introduced scattering potentials [235]. We found a strongly enhanced zero-field resistance for the case of retroreflectively shaped obstacles. This is in accordance with a theory based on a classical memory effect [238–240]. There is still much to learn from this implementation of the classical Lorentz model. Naturally, one must ask the question, if the maximum in magnetoconductivity is also influenced by the shape of the obstacles and, if yes, can it be linked to an underlying phase diagram? It would also be of highest fundamental interest to not only introduce artificial hard-wall scatterers, but also control the correlated background disorder. Theoretical predictions exist for some cases [20, 21], but a well defined experimental study has not been conducted to the best of our knowledge. Preliminary experiments on non-linear magnetotransport in Lorentz gases also exhibited interesting features, which were reminiscent of results obtained in Ref. [245], although their setup did not include artificial disorder. The link between these experiments remains unclear to date.

Bibliography

[1] J. Bardeen and W. H. Brattain, Phys. Rev. **74**, 230 (1948).

[2] K. von Klitzing, G. Dorda, and M. Pepper, Phys. Rev. Lett. **45**, 494 (1980).

[3] D. C. Tsui, H. L. Stormer, and A. C. Gossard, Phys. Rev. Lett. **48**, 1559 (1982).

[4] B. J. van Wees, H. van Houten, C. W. J. Beenakker, J. G. Williamson, L. P. Kouwenhoven, D. van der Marel, and C. T. Foxon, Phys. Rev. Lett. **60**, 848 (1988).

[5] D. A. Wharam, T. J. Thornton, R. Newbury, M. Pepper, H. Ahmed, J. E. F. Frost, D. G. Hasko, D. C. Peacock, D. A. Ritchie, and G. A. C. Jones, J. Phys. C **21**, L209 (1988).

[6] J. H. F. Scott-Thomas, S. B. Field, M. A. Kastner, H. I. Smith, and D. A. Antoniadis, Phys. Rev. Lett. **62**, 583 (1989).

[7] U. Meirav, M. A. Kastner, and S. J. Wind, Phys. Rev. Lett. **65**, 771 (1990).

[8] S. Datta, *Electronic Transport in Mesoscopic Systems*, Cambridge University Press, Cambridge, United Kingdom, 1997.

[9] T. Heinzel, Mesoscopic Electronics in Solid State Nanostructures, Wiley-VCH, 2007.

[10] T. Ihn, *Semiconductor Nanostructures - Quantum States and Electronic Transport*, Oxford University Press, New York, 2010.

[11] K. S. Novoselov, A. K. Geim, S. V. Morozov, D. Jiang, Y. Zhang, S. V. Dubonos, I. V. Grigorieva, and A. A. Firsov, Science **306**, 666 (2004).

[12] K. S. Novoselov, A. K. Geim, S. V. Morozov, D. Jiang, M. I. Katsnelson, and I. V. Grigorieva, Nature **438**, 197 (2005).

[13] B. A. Bernevig, T. L. Hughes, and S.-C. Zhang, Science **314**, 1757 (2006).

[14] M. König, S. Wiedmann, C. Brüne, A. Roth, H. Buhmann, L. W. Molenkamp, X.-L. Qi, and S.-C. Zhang, Science **318**, 766 (2007).

[15] M. Z. Hasan and C. L. Kane, Rev. Mod. Phys. **82**, 3045 (2010).

[16] X.-L. Qi and S.-C. Zhang, Rev. Mod. Phys. **83**, 1057 (2011).

[17] V. Umansky, R. de Picciotto, and M. Heiblum, Appl. Phys. Lett. **71**, 683 (1997).

[18] A. V. Bobylev, F. A. Maaø, A. Hansen, and E. H. Hauge, Phys. Rev. Lett. **75**, 197 (1995).

[19] A. D. Mirlin, J. Wilke, F. Evers, D. G. Polyakov, and P. Wölfle, Phys. Rev. Lett. **83**, 2801 (1999).

[20] A. D. Mirlin, D. G. Polyakov, F. Evers, and P. Wölfle, Phys. Rev. Lett. **87**, 126805 (2001).

[21] D. G. Polyakov, F. Evers, A. D. Mirlin, and P. Wölfle, Phys. Rev. B **64**, 205306 (2001).

[22] D. Weiss, K. von Klitzing, K. Ploog, and G. Weimann, Europhys. Lett. **8**, 179 (1989).

[23] R. R. Gerhardts, D. Weiss, and K. von Klitzing, Phys. Rev. Lett. **62**, 1173 (1989).

[24] R. W. Winkler, J. P. Kotthaus, and K. Ploog, Phys. Rev. Lett. **62**, 1177 (1989).

[25] K. Ensslin and P. M. Petroff, Phys. Rev. B **41**, 12307 (1990).

[26] D. Weiss, M. L. Roukes, A. Menschig, P. Grambow, K. von Klitzing, and G. Weimann, Phys. Rev. Lett. **66**, 2790 (1991).

[27] A. Lorke, J. P. Kotthaus, and K. Ploog, Phys. Rev. B **44**, 3447 (1991).

[28] S. Izawa, S. Katsumoto, A. Endo, and Y. Iye, J. Phys. Soc. Jpn. **64**, 706 (1995).

[29] H. A. Carmona, A. K. Geim, A. Nogaret, P. C. Main, T. J. Foster, M. Henini, S. P. Beaumont, and M. G. Blamire, Phys. Rev. Lett. **74**, 3009 (1995).

[30] P. D. Ye, D. Weiss, R. R. Gerhardts, M. Seeger, K. von Klitzing, K. Eberl, and H. Nickel, Phys. Rev. Lett. **74**, 3013 (1995).

[31] P. D. Ye, D. Weiss, K. von Klitzing, K. Eberl, and H. Nickel, Applied Physics Letters **67**, 1441 (1995).

[32] M. L. Leadbeater, C. L. Foden, J. H. Burroughes, M. Pepper, T. M. Burke, L. L. Wang, M. P. Grimshaw, and D. A. Ritchie, Phys. Rev. B **52**, R8629 (1995).

[33] I. S. Ibrahim, V. A. Schweigert, and F. M. Peeters, Phys. Rev. B **56**, 7508 (1997).

[34] F. G. Monzon, M. Johnson, and M. L. Roukes, Appl. Phys. Lett. **71**, 3087 (1997).

[35] V. Kubrak, F. Rahman, B. L. Gallagher, P. C. Main, M. Henini, C. H. Marrows, and M. A. Howson, Appl. Phys. Lett. **74**, 2507 (1999).

[36] T. Vančura, T. Ihn, S. Broderick, K. Ensslin, W. Wegscheider, and M. Bichler, Phys. Rev. B **62**, 5074 (2000).

[37] J. Reijniers, A. Matulis, K. Chang, F. M. Peeters, and P. Vasilopoulos, Europhys. Lett. **59**, 749 (2002).

[38] A. Tarasov, S. Hugger, H. Xu, M. Cerchez, T. Heinzel, I. V. Zozoulenko, U. Gasser-Szerer, D. Reuter, and A. D. Wieck, Phys. Rev. Lett. **104**, 186801 (2010).

[39] H. Xu, T. Heinzel, and I. V. Zozoulenko, Phys. Rev. B **84**, 035319 (2011).

[40] B. Schüler, M. Cerchez, H. Xu, J. Schluck, T. Heinzel, D. Reuter, and A. D. Wieck, Phys. Rev. B **90**, 201111(R) (2014).

[41] A. Kuzmany and H. Spohn, Phys. Rev. E **57**, 5544 (1998).

[42] K. Ploog, Annual Review of Materials Science **11**, 171 (1981).

[43] B. A. Joyce, Reports on Progress in Physics **48**, 1637 (1985).

[44] T. Ando, A. B. Fowler, and F. Stern, Rev. Mod. Phys. **54**, 437 (1982).

[45] V. Umansky and M. Heiblum, in *Molecular Beam Epitaxy*, edited by M. Henini, Elsevier, Oxford, 2013, pp. 121 – 137.

[46] M. J. Manfra, Annual Review of Condensed Matter Physics **5**, 347 (2014).

[47] S. Kasap and P. Capper, *Springer Handbook of Electronic and Photonic Materials*, Springer, Berlin, Heidelberg, 2017.

[48] R. Peierls, Zeitschrift für Physik **80**, 763 (1933).

[49] R. Dingle, H. L. Störmer, A. C. Gossard, and W. Wiegmann, Appl. Phys. Lett. **33**, 665 (1978).

[50] I. A. Dmitriev, A. D. Mirlin, D. G. Polyakov, and M. A. Zudov, Rev. Mod. Phys. **84**, 1709 (2012).

[51] J. P. Eisenstein, K. B. Cooper, L. N. Pfeiffer, and K. W. West, Phys. Rev. Lett. **88**, 076801 (2002).

[52] V. Umansky, M. Heiblum, Y. Levinson, J. Smet, J. N´ubler, and M. Dolev, Journal of Crystal Growth **311**, 1658 (2009), International Conference on Molecular Beam Epitaxy (MBE-XV).

[53] G. C. Gardner, S. Fallahi, J. D. Watson, and M. J. Manfra, Journal of Crystal Growth **441**, 71 (2016).

[54] A. H. C. Neto, F. Guinea, N. M. R. Peres, K. S. Novoselov, and A. K. Geim, Rev. Mod. Phys. **81**, 109 (2009).

[55] K. S. Novoselov, A. Mishchenko, A. Carvalho, and A. H. Castro Neto, Science **353** (2016).

[56] N. Reyren, S. Thiel, A. D. Caviglia, L. F. Kourkoutis, G. Hammerl, C. Richter, C. W. Schneider, T. Kopp, A.-S. Rüetschi, D. Jaccard, M. Gabay, D. A. Muller, J.-M. Triscone, and J. Mannhart, Science **317**, 1196 (2007).

[57] A. Brinkman, M. Huijben, M. van Zalk, J. Huijben, U. Zeitler, J. C. Maan, W. G. van der Wiel, G. Rijnders, D. H. A. Blank, and H. Hilgenkamp, Nature Materials **6**, 493 EP (2007).

[58] H. Y. Hwang, Y. Iwasa, M. Kawasaki, B. Keimer, N. Nagaosa, and Y. Tokura, Nature Materials **11**, 103 EP (2012), Review Article.

[59] K. Pierz, Private communication.

[60] Gregory L. Snider, Available via https://www3.nd.edu/~gsnider/ . (checked: 20.02.2018).

[61] Y. Nishi and R. Doering, *Handbook of Semiconductor Manufacturing Technology, Second Edition*, CRC Press, Boca Raton, Fla, 2007.

[62] S. M. Sze and M.-K. Lee, *Semiconductor Devices - Physics and Technology*, John Wiley & Sons, New York, 2012.

[63] B. El-Kareh, *Fundamentals of Semiconductor Processing Technology*, Springer Science & Business Media, Berlin Heidelberg, 2012.

[64] Bernd Schüler, Transporteigenschaften von Quantendrähten in inhomogenen Magnetfeldern,Dissertation, 2015, Heinrich-Heine Universität Düsseldorf.

[65] P. Drude, Annalen der Physik **306**, 566 (1900).

[66] H. Lorentz, Proc. R. Acad. Sci. Amsterdam **7**, 438 (1905).

[67] A. Sommerfeld and H. Bethe, *Elektronentheorie der Metalle*, pp. 333–622, Springer, Berlin, Heidelberg, 1933.

[68] L. Landau, Zeitschrift für Physik **64**, 629 (1930).

[69] L. Shubnikov and W. J. De Haas, Nature **126**, 500 EP (1930).

[70] G. E. Stillman and C. M. Wolfe, Thin Solid Films **31**, 69 (1976).

[71] K. Hirakawa and H. Sakaki, Phys. Rev. B **33**, 8291 (1986).

[72] J. J. Harris, J. A. Pals, and R. Woltjer, Reports on Progress in Physics **52**, 1217 (1989).

[73] F. Pobell, *Matter and Methods at Low Temperatures*, Springer Science & Business Media, Berlin Heidelberg, 2013.

[74] A. T. A. M. de Waele, Journal of Low Temperature Physics **164**, 179 (2011).

[75] H. London, G. R. Clarke, and E. Mendoza, Phys. Rev. **128**, 1992 (1962).

[76] R. Kubo, J. Phys. Soc. Jpn. **12**, 570 (1957).

[77] S. Meckler, T. Heinzel, A. Cavanna, G. Faini, U. Gennser, and D. Mailly, Phys. Rev. B **72**, 035319 (2005).

[78] S. Klinkhammer, H. Xu, T. Heinzel, U. Gennser, G. Faini, C. Ulysse, and A. Cavanna, Phys. Rev. B **77**, 235311 (2008).

[79] R. Landauer, IBM J. Res. Dev. **1**, 223 (1957).

[80] M. Büttiker, Phys. Rev. Lett. **57**, 1761 (1986).

[81] C. W. J. Beenakker and H. van Houten, Phys. Rev. Lett. **63**, 1857 (1989).

[82] M. Cerchez, S. Hugger, T. Heinzel, and N. Schulz, Phys. Rev. B **75**, 035341 (2007).

[83] S. Hugger, M. Cerchez, H. Xu, and T. Heinzel, Phys. Rev. B **76**, 195308 (2007).

[84] M. Cerchez, T. Heinzel, D. Reuter, and A. Wieck, Superlattices and Microstructures **46**, 723 (2009).

[85] M. Cerchez and T. Heinzel, Appl. Phys. Lett. **98**, 232111 (2011).

[86] B. Schüler, M. Cerchez, H. Xu, T. Heinzel, D. Reuter, and A. Wieck, Superlattices and Microstructures **79**, 54 (2015).

[87] C. W. Groth, M. Wimmer, A. R. Akhmerov, and X. Waintal, New Journal of Physics **16**, 063065 (2014).

[88] H. U. Baranger and A. D. Stone, Phys. Rev. B **40**, 8169 (1989).

[89] T. Kiendl, F. von Oppen, and P. W. Brouwer, Phys. Rev. B **96**, 134501 (2017).

[90] A. Nogaret, J. Phys. Cond. Mat. **22**, 253201 (2010).

[91] F. M. Peeters and A. Matulis, Phys. Rev. B **48**, 15166 (1993).

[92] A. Matulis, F. M. Peeters, and P. Vasilopoulos, Phys. Rev. Lett. **72**, 1518 (1994).

[93] A. Majumdar, Phys. Rev. B **54**, 11911 (1996).

[94] Y. Guo, B. L. Gu, Z. Zheng, J. Z. Yu, and Y. Kawazoe, Phys. Rev. B **62**, 2635 (2000).

[95] G. Papp and F. M. Peeters, Appl. Phys. Lett. **78**, 2184 (2001).

[96] H. Z. Xu and Y. Okada, Appl. Phys. Lett. **79**, 3119 (2001).

[97] F. Zhai and H. Q. Xu, Appl. Phys. Lett. **88**, 032502 (2006).

[98] A. De Martino, L. Dell'Anna, and R. Egger, Phys. Rev. Lett. **98**, 066802 (2007).

[99] X.-Q. Li and F. Peeters, Superlattices and Microstructures **22**, 243 (1997).

[100] I. S. Ibrahim, V. A. Schweigert, and F. M. Peeters, Phys. Rev. B **57**, 15416 (1998).

[101] Y. G. Cornelissens and F. M. Peeters, J. Appl. Phys. **92**, 2006 (2002).

[102] F. M. Peeters and X. Q. Li, Appl. Phys. Lett. **72**, 572 (1998).

[103] S. Fasbender, J. Schluck, M. Cerchez, T. Heinzel, S. Sievers, K. Pierz, and H. W. Schumacher, Journal of Applied Physics **119**, 094302 (2016).

[104] J. Clarke and A. I. Braginski, *The SQUID Handbook - Fundamentals and Technology of SQUIDs and SQUID Systems*, John Wiley & Sons, New York, 2006.

[105] J. E. Müller, Phys. Rev. Lett. **68**, 385 (1992).

[106] A. Nogaret, S. J. Bending, and M. Henini, Phys. Rev. Lett. **84**, 2231 (2000).

[107] J. Reijniers and F. M. Peeters, Phys. Rev. B **63**, 165317 (2001).

[108] D. N. Lawton, A. Nogaret, S. J. Bending, D. K. Maude, J. C. Portal, and M. Henini, Phys. Rev. B **64**, 033312 (2001).

[109] M. Hara, A. Endo, S. Katsumoto, and Y. Iye, Phys. Rev. B **69**, 153304 (2004).

[110] A. Leuschner, J. Schluck, M. Cerchez, T. Heinzel, K. Pierz, and H. W. Schumacher, Phys. Rev. B **95**, 155440 (2017).

[111] T. Ando, S. Uryu, S. Ishizaka, and T. Nakanishi, Chaos, Solitons & Fractals **8**, 1057 (1997).

[112] P. H. Beton, E. S. Alves, P. C. Main, L. Eaves, M. W. Dellow, M. Henini, O. H. Hughes, S. P. Beaumont, and C. D. W. Wilkinson, Phys. Rev. B **42**, 9229 (1990).

[113] P. Vasilopoulos and F. M. Peeters, Phys. Rev. Lett. **63**, 2120 (1989).

[114] C. W. J. Beenakker, Phys. Rev. Lett. **62**, 2020 (1989).

[115] C. Zhang and R. R. Gerhardts, Phys. Rev. B **41**, 12850 (1990).

[116] P. Bøggild, A. Boisen, K. Birkelund, C. B. Sørensen, R. Taboryski, and P. E. Lindelof, Phys. Rev. B **51**, 7333 (1995).

[117] Y. Paltiel, U. Meirav, D. Mahalu, and H. Shtrikman, Phys. Rev. B **56**, 6416 (1997).

[118] A. D. Mirlin and P. Wölfle, Phys. Rev. B **58**, 12986 (1998).

[119] A. Endo, S. Katsumoto, and Y. Iye, Phys. Rev. B **62**, 16761 (2000).

[120] P. H. Beton, P. C. Main, M. Davison, M. Dellow, R. P. Taylor, E. S. Alves, L. Eaves, S. P. Beaumont, and C. D. W. Wilkinson, Phys. Rev. B **42**, 9689 (1990).

[121] F. M. Peeters and P. Vasilopoulos, Phys. Rev. B **46**, 4667 (1992).

[122] J. Wagenhuber, T. Geisel, P. Niebauer, and G. Obermair, Phys. Rev. B **45**, 4372 (1992).

[123] A. Messica, A. Soibel, U. Meirav, A. Stern, H. Shtrikman, V. Umansky, and D. Mahalu, Phys. Rev. Lett. **78**, 705 (1997).

[124] D. Weiss, C. Zhang, R. R. Gerhardts, K. v. Klitzing, and G. Weimann, Phys. Rev. B **39**, 13020 (1989).

[125] A. K. Geim, R. Taboryski, A. Kristensen, S. V. Dubonos, and P. E. Lindelof, Phys. Rev. B **46**, 4324 (1992).

[126] G. Müller, D. Weiss, K. von Klitzing, P. Středa, and G. Weimann, Phys. Rev. B **51**, 10236 (1995).

[127] P. Vasilopoulos and F. Peeters, Superlattices and Microstructures **7**, 393 (1990).

[128] D. P. Xue and G. Xiao, Phys. Rev. B **45**, 5986 (1992).

[129] F. M. Peeters and P. Vasilopoulos, Phys. Rev. B **47**, 1466 (1993).

[130] R. Yagi and Y. Iye, J. Phys. Soc. Jpn. **62**, 1279 (1993).

[131] P. D. Ye, D. Weiss, R. R. Gerhardts, K. von Klitzing, K. Eberl, H. Nickel, and C. T. Foxon, Semiconductor Science and Technology **10**, 715 (1995).

[132] J. H. Davies and I. A. Larkin, Phys. Rev. B **49**, 4800 (1994).

[133] I. A. Larkin, J. H. Davies, A. R. Long, and C. Ramon, Phys. Rev. B **56**, 15242 (1997).

[134] E. Skuras, A. R. Long, I. A. Larkin, J. H. Davies, and M. C. Holland, Applied Physics Letters **70**, 871 (1997).

[135] A. R. Long, E. Skuras, S. Vallis, R. Cuscó, I. A. Larkin, J. H. Davies, and M. C. Holland, Phys. Rev. B **60**, 1964 (1999).

[136] A. Nogaret, S. Carlton, B. L. Gallagher, P. C. Main, M. Henini, R. Wirtz, R. Newbury, M. A. Howson, and S. P. Beaumont, Phys. Rev. B **55**, 16037 (1997).

[137] M. Kato, A. Endo, S. Katsumoto, and Y. Iye, Phys. Rev. B **58**, 4876 (1998).

[138] M. Tornow, D. Weiss, A. Manolescu, R. Menne, K. v. Klitzing, and G. Weimann, Phys. Rev. B **54**, 16397 (1996).

[139] A. Endo and Y. Iye, Journal of the Physical Society of Japan **77**, 054709 (2008).

[140] K. W. Edmonds, B. L. Gallagher, P. C. Main, N. Overend, R. Wirtz, A. Nogaret, M. Henini, C. H. Marrows, B. J. Hickey, and S. Thoms, Phys. Rev. B **64**, 041303 (2001).

[141] J. Shi, F. M. Peeters, K. W. Edmonds, and B. L. Gallagher, Phys. Rev. B **66**, 035328 (2002).

[142] E. Skuras, A. R. Long, S. Chowdhury, M. Rahman, K. J. Kirk, and J. H. Davies, Journal of Applied Physics **90**, 2623 (2001).

[143] W. Breuer, D. Weiss, and V. Umansky, Physica E: Low-dimensional Systems and Nanostructures **12**, 216 (2002).

[144] M. Hara, A. Endo, S. Katsumoto, and Y. Iye, Physica E: Low-dimensional Systems and Nanostructures **22**, 345 (2004).

[145] T. McMullen, J. Davies, and A. Long, Physica E: Low-dimensional Systems and Nanostructures **34**, 564 (2006).

[146] W. V. Roy, J. D. Boeck, and G. Borghs, Applied Physics Letters **61**, 3056 (1992).

[147] J. Yoshida, T. Ohtsuki, and Y. Ono, Journal of the Physical Society of Japan **67**, 3886 (1998).

[148] R. Hennig and M. Suhrke, Phys. Rev. B **60**, 11535 (1999).

[149] E. S. Alves, P. H. Beton, M. Henini, L. Eaves, P. C. Main, O. H. Hughes, G. A. Toombs, S. P. Beaumont, and C. D. W. Wilkinson, Journal of Physics: Condensed Matter **1**, 8257 (1989).

[150] S. Hugger, T. Heinzel, and T. Thurn-Albrecht, Applied Physics Letters **93**, 102110 (2008).

[151] Y. Kato, A. Endo, S. Katsumoto, and Y. Iye, Phys. Rev. B **86**, 235315 (2012).

[152] T. Geisel, J. Wagenhuber, P. Niebauer, and G. Obermair, Phys. Rev. Lett. **64**, 1581 (1990).

[153] R. R. Gerhardts, Phys. Rev. B **45**, 3449 (1992).

[154] D. E. Grant, A. D. Long, and J. H. Davies, Phys. Rev. B **61**, 13127 (2000).

[155] R. Ketzmerick, K. Kruse, D. Springsguth, and T. Geisel, Phys. Rev. Lett. **84**, 2929 (2000).

[156] A. D. Mirlin, E. Tsitsishvili, and P. Wölfle, Phys. Rev. B **63**, 245310 (2001).

[157] D. Hofstadter, Phys. Rev. B **14**, 2239 (1976).

[158] F. H. Claro and G. H. Wannier, Phys. Rev. B **19**, 6068 (1979).

[159] D. Pfannkuche and R. R. Gerhardts, Phys. Rev. B **46**, 12606 (1992).

[160] G. Petschel and T. Geisel, Phys. Rev. Lett. **71**, 239 (1993).

[161] D. Springsguth, R. Ketzmerick, and T. Geisel, Phys. Rev. B **56**, 2036 (1997).

[162] R. R. Gerhardts, D. Weiss, and U. Wulf, Phys. Rev. B **43**, 5192 (1991).

[163] T. Schlösser, K. Ensslin, J. P. Kotthaus, and M. Holland, Europhys. Lett. **33**, 683 (1996).

[164] C. Albrecht, J. H. Smet, K. v. Klitzing, D. Weiss, V. Umansky, and H. Schweizer, Phys. Rev. Lett. **86**, 147 (2001).

[165] M. C. Geisler, J. H. Smet, V. Umansky, K. von Klitzing, B. Naundorf, R. Ketzmerick, and H. Schweizer, Phys. Rev. Lett. **92**, 256801 (2004).

[166] R. Fleischmann, T. Geisel, and R. Ketzmerick, Phys. Rev. Lett. **68**, 1367 (1992).

[167] R. Fleischmann, T. Geisel, and R. Ketzmerick, Europhys. Lett. **25**, 219 (1994).

[168] S. Ishizaka and T. Ando, Phys. Rev. B **55**, 16331 (1997).

[169] D. Weiss, K. Richter, A. Menschig, R. Bergmann, H. Schweizer, K. von Klitzing, and G. Weimann, Phys. Rev. Lett. **70**, 4118 (1993).

[170] R. Schuster, K. Ensslin, D. Wharam, S. Kühn, J. P. Kotthaus, G. Böhm, W. Klein, G. Tränkle, and G. Weimann, Phys. Rev. B **49**, 8510 (1994).

[171] F. Nihey, S. W. Hwang, and K. Nakamura, Phys. Rev. B **51**, 4649 (1995).

[172] G. Hackenbroich and F. van Oppen, Europhys. Lett. **29**, 151 (1995).

[173] K. Richter, Europhys. Lett. **29**, 7 (1995).

[174] M. C. Gutzwiller, J. Math. Phys. **12**, 343 (1971).

[175] H. Silberbauer, Journal of Physics: Condensed Matter **4**, 7355 (1992).

[176] R. B. S. Oakeshott and A. MacKinnon, Journal of Physics: Condensed Matter **6**, 1519 (1994).

[177] H. Silberbauer and U. Rössler, Phys. Rev. B **50**, 11911 (1994).

[178] H. Silberbauer, P. Rotter, M. Suhrke, and U. Rossler, Semiconductor Science and Technology **9**, 1906 (1994).

[179] S. Ishizaka, F. Nihey, K. Nakamura, J. Sone, and T. Ando, Phys. Rev. B **51**, 9881 (1995).

[180] T. Ishizaka and T. Ando, Phys. Rev. B **56**, 15195 (1997).

[181] I. V. Zozoulenko, F. A. Maao, and E. H. Hauge, Phys. Rev. B **53**, 7975 (1996).

[182] I. V. Zozoulenko, F. A. Maao, and E. H. Hauge, Phys. Rev. B **53**, 7987 (1996).

[183] I. V. Zozoulenko, F. A. Maao, and E. H. Hauge, Phys. Rev. B **56**, 4710 (1997).

[184] W. Kang, H. L. Stormer, L. N. Pfeiffer, K. W. Baldwin, and K. W. West, Phys. Rev. Lett. **71**, 3850 (1993).

[185] N. M. S. Choque, G. M. Gusev, J. R. Leite, A. A. Bykov, L. V. Litvin, N. T. Moshegov, A. I. Toropov, D. K. Maude, and J. C. Portal, Phys. Rev. B **66**, 035324 (2002).

[186] A. Dorn, E. Bieri, T. Ihn, K. Ensslin, D. D. Driscoll, and A. C. Gossard, Phys. Rev. B **71**, 035343 (2005).

[187] Z. Q. Yuan, C. L. Yang, R. R. Du, L. N. Pfeiffer, and K. W. West, Phys. Rev. B **74**, 075313 (2006).

[188] R. Schuster, K. Ensslin, D. Wharam, S. Kühn, J. P. Kotthaus, G. Böhm, W. Klein, G. Tränkle, and G. Weimann, Phys. Rev. B **49**, 8510 (R) (1994).

[189] R. Schuster, K. Ensslin, J. P. Kotthaus, G. Böhm, and W. Klein, Phys. Rev. B **55**, 2237 (1997).

[190] S. Lüthi, T. Vancura, K. Ensslin, R. Schuster, G. Böhm, and W. Klein, Phys. Rev. B **55**, 13088 (1997).

[191] R. Neudert, P. Rotter, U. Rössler, and M. Suhrke, Phys. Rev. B **55**, 2242 (1997).

[192] J. Schluck, J. Feilhauer, D. Kazazis, U. Gennser, K. Pierz, H. Schumacher, and T. Heinzel, submitted to Phys. Rev. B. (2018) .

[193] J. Schluck, S. Fasbender, T. Heinzel, K. Pierz, H. W. Schumacher, D. Kazazis, and U. Gennser, Phys. Rev. B **91**, 195303 (2015).

[194] R. R. Gerhardts, Phys. Rev. B **53**, 11064 (1996).

[195] R. R. Gerhardts, D. Pfannkuche, and V. Gudmundsson, Phys. Rev. B **53**, 9591 (1996).

[196] R. Menne and R. R. Gerhardts, Phys. Rev. B **57**, 1707 (1998).

[197] S. D. M. Zwerschke, A. Manolescu, and R. R. Gerhardts, Phys. Rev. B **60**, 5536 (1999).

[198] X. F. Wang, P. Vasilopoulos, and F. M. Peeters, Phys. Rev. B **70**, 155312 (2004).

[199] R. B. S. Oakeshott and A. MacKinnon, Journal of Physics: Condensed Matter **5**, 9355 (1993).

[200] I. S. Ibrahim and F. M. Peeters, Phys. Rev. B **52**, 17321 (1995).

[201] S. Littlejohn, A. Nogaret, S. R. Davies, M. Henini, H. E. Beere, and D. A. Ritchie, Applied Physics Letters **99**, 242107 (2011).

[202] B. J. Sung and A. Yethiraj, Phys. Rev. Lett. **96**, 228103 (2006).

[203] F. Höfling, T. Franosch, and E. Frey, Phys. Rev. Lett. **96**, 165901 (2006).

[204] F. Höfling and T. Franosch, Phys. Rev. Lett. **98**, 140601 (2007).

[205] T. Bauer, F. Höfling, T. Munk, E. Frey, and T. Franosch, The European Physical Journal Special Topics **189**, 103 (2010).

[206] T. O. E. Skinner, S. K. Schnyder, D. G. A. L. Aarts, J. Horbach, and R. P. A. Dullens, Phys. Rev. Lett. **111**, 128301 (2013).

[207] S. K. Schnyder, M. Spanner, F. Hofling, T. Franosch, and J. Horbach, Soft Matter **11**, 701 (2015).

[208] E. H. Hauge, What can one learn from lorentz models?, in *Transport Phenomena*, edited by G. Kirczenow and J. Marro, pp. 337–367, Berlin, Heidelberg, 1974, Springer.

[209] H. Spohn, Rev. Mod. Phys. **52**, 569 (1980).

[210] H. van Beijeren, Rev. Mod. Phys. **54**, 195 (1982).

[211] S. Mertens and C. Moore, Phys. Rev. E **86**, 061109 (2012).

[212] E. M. Baskin, L. N. Magarill, and M. V. Entin, Sov. Phys. JETP **48**, 365 (1978).

[213] A. V. Bobylev, F. A. Maaø, A. Hansen, and E. H. Hauge, Journal of Statistical Physics **87**, 1205 (1997).

[214] E. Baskin and M. Entin, Physica B: Condensed Matter **249-251**, 805 (1998).

[215] A. Dmitriev, M. Dyakonov, and R. Jullien, Phys. Rev. B **64**, 233321 (2001).

[216] M. Ando, A. Endo, S. Katsumoto, and Y. Iye, Physica B: Condensed Matter **284-288**, 1900 (2000).

[217] A. W. Rushforth, B. L. Gallagher, P. C. Main, A. C. Neumann, M. Henini, C. H. Marrows, and B. J. Hickey, Phys. Rev. B **70**, 193313 (2004).

[218] A. V. Goran, A. A. Bykov, A. K. Bakarov, and J. C. Portal, Journal of Experimental and Theoretical Physics Letters **79**, 495 (2004).

[219] S. Wada, N. Okuda, and J. Wakabayashi, Physica E: Low-dimensional Systems and Nanostructures **42**, 1138 (2010).

[220] V. Renard, Z. D. Kvon, G. M. Gusev, and J. C. Portal, Phys. Rev. B **70**, 033303 (2004).

[221] B. L. Altshuler, D. Khmel'nitzkii, A. I. Larkin, and P. A. Lee, Phys. Rev. B **22**, 5142 (1980).

[222] G. M. Gusev, P. Basmaji, Z. D. Kvon, L. V. Litvin, Y. Nastaushev, and A. I. Toropov, J. Phys. Cond. Mat. **6**, 73 (1994).

[223] K. Tsukagoshi, S. Wakayama, K. Oto, S. Takaoka, K. Murase, and K. Gamo, Phys. Rev. B **52**, 8344 (1995).

[224] G. Lütjering, Nanostrukturierte Antidot-Systeme, Stuttgart University, 1996.

[225] G. Nachtwei, G. Lütjering, D. Weiss, Z. H. Liu, K. von Klitzing, and C. T. Foxon, Phys. Rev. B **55**, 6731 (1997).

[226] G. Nachtwei, Z. H. Liu, G. Lütjering, R. R. Gerhardts, D. Weiss, K. von Klitzing, and K. Eberl, Phys. Rev. B **57**, 9937 (1998).

[227] O. Yevtuchenko, G. Lütjering, D. Weiss, and K. Richter, Phys. Rev. Lett. **84**, 542 (2000).

[228] S. Cinà, D. D. Arnone, H. P. Hughes, C. L. Foden, D. M. Whittaker, M. Pepper, and D. A. Ritchie, Phys. Rev. B **60**, 7780 (1999).

[229] L. Bockhorn, I. V. Gornyi, D. Schuh, C. Reichl, W. Wegscheider, and R. J. Haug, Phys. Rev. B **90**, 165434 (2014).

[230] K. Martens, L. Angelani, R. Di Leonardo, and L. Bocquet, The European Physical Journal E **35**, 84 (2012).

[231] K. Erglis, Q. Wen, V. Ose, A. Zeltins, A. Sharipo, P. A. Janmey, and A. Cebers, Biophysical Journal **93**, 1402 (2007).

[232] M. Zeitz, K. Wolff, and H. Stark, The European Physical Journal E **40**, 23 (2017).

[233] W. Schirmacher, B. Fuchs, F. Höfling, and T. Franosch, Phys. Rev. Lett. **115**, 240602 (2015).

[234] N. H. Siboni, J. Schluck, K. Pierz, H. W. Schumacher, D. Kazazis, J. Horbach, and T. Heinzel, Phys. Rev. Lett. **120**, 056601 (2018).

[235] J. Schluck, M. Hund, T. Heckenthaler, D. Kazazis, D. Mailly, U. Gennser, K. Pierz, H. Schumacher, N. Siboni, J. Horbach, and T. Heinzel, accepted for publication in Phys. Rev. B. (2018) .

[236] V. I. Yudson and D. L. Maslov, Phys. Rev. B **75**, 241408 (2007).

[237] S. de Haan, A. Lorke, R. Hennig, M. Suhrke, W. Wegscheider, and M. Bichler, Phys. Rev. B **60**, 8845 (1999).

[238] A. Dmitriev, M. Dyakonov, and R. Jullien, Phys. Rev. Lett. **89**, 266804 (2002).

[239] V. V. Cheianov, A. P. Dmitriev, and V. Y. Kachorovskii, Phys. Rev. B **68**, 201304 (R) (2003).

[240] V. V. Cheianov, A. P. Dmitriev, and V. Y. Kachorovskii, Phys. Rev. B **70**, 245307 (2004).

[241] A. P. Dmitriev and V. Y. Kachorovskii, Phys. Rev. B **77**, 193308 (2008).

[242] N. M. S. Choque, G. M. Gusev, J. R. Leite, A. A. Bykov, A. K. Kalagin, V. M. Kudryashev, and A. I. Toropov, Phys. Rev. B **70**, 235326 (2004).

[243] H.-I. Cho, G. M. Gusev, Z. D. Kvon, V. T. Renard, J.-H. Lee, and J.-C. Portal, Phys. Rev. B **71**, 245323 (2005).

[244] J. Blaschke and M. Brack, Phys. Rev. B **56**, 182 (1997).

[245] Q. Shi, M. A. Zudov, L. N. Pfeiffer, and K. W. West, Phys. Rev. B **90**, 201301(R) (2014).

Kwant-code example

```
1  #import relevant packages
2  import math
3  from cmath import exp
4  from cmath import cos
5  import numpy
6  import kwant
7  import sys
8  import random
9
10 # this is just for numbering the output files
11 nametag=1
12
13 # define parameters
14 e=1.602e-19
15 hb=6.626e-34/2/math.pi
16 h=6.626e-34
17 nm=1e-9
18 ms=0.067*9.109e-31
19
20 a=6*nm # tight-binding constant
21 t=hb*hb/2/a/a/ms #tight-binding energy t
22 # magnetic field range of interest
23 B=numpy.linspace((0.),(.5),1001)
24
25 mfp=90.*nm*1000./a # Mean free path
26 EF=2.1273e-21 # Fermi energy
27 V0=math.sqrt(2*math.pow(t,1.5)*math.sqrt(EF)/mfp)/t # sigma of
      gaussian distribution used to calculate random on-site
      disorder corresponding to given mean free path
28
29 # define Hall bar geometry
30 W=2500.*nm/a # Half width of the Hall bar
31 L=3000.*nm/a  # Half length of the Hall bar
32 WC=1.5*1000.*nm/a # Width of voltage probes
33 DC=2.5*1000.*nm/a #Distance of outer end of voltage probes from
      center of Hall bar
34
35 #this function rho takes care of rotating the magnetic vector
      potential over the course of the Hall bar, thus allowing for
      leads that are perpendicular to each other
36 def rho(x):
37     a1=2./(DC-L)**3
38     b1=3.*(DC+L)/(DC-L)**3
39     c1=6.*DC*L/(DC-L)**3
```

```
40        d1=L**2*(3.*DC-L)/(DC-L)**3
41
42        if x<=-DC:
43            return a1*x**3+b1*x**2+c1*x+d1
44        if -DC<x<DC :
45            return 1
46        if x>=DC :
47            return -a1*x**3+b1*x**2-c1*x+d1
48
49  # On-site disorder within the scattering region. The random part
        takes care of residual disorder, 4 is from tight-binding model
        . Additional potential should be entered here.
50  def osd(site1, site2=0.,phi=0.0):
51        x,y=site1.pos
52        return random.gauss(0,V0)+4.
53  #hoppings in the scattering region. rho mediates between the
        hoppings in the leads.
54  def hopy(site1, site2, phi=0.0):
55        x,y = site1.pos
56        x2,y2=site2.pos
57        return -exp(1j *2.*math.pi*(y2-y)* (x+x2)/2.*phi*rho((x+x2
            )/2.))
58  def hopx(site1, site2,phi=0.0):
59        x,y = site1.pos
60        x2,y2=site2.pos
61        return -exp(1j *2.*math.pi*(y+y2)/2.*((x2*rho(x2)-x*rho(x)
            )-(x2-x))*phi)
62  #hoppings in leads with symmetry in x-direction
63  def hopylx(site1, site2, phi=0.0):
64        return -1
65
66  def hopxlx(site1, site2,phi=0.0):
67        x,y = site1.pos
68        x2,y2=site2.pos
69        return -exp(-1j *2.*math.pi*(y+y2)/2*(x2-x)*phi)
70  #hoppings in leads with symmetry in y-direction
71  def hopyly(site1, site2, phi=0.0):
72        x,y = site1.pos
73        x2,y2=site2.pos
74        return -exp(1j *2.*math.pi*(y2-y)* (x+x2)/2.*phi)
75
76  def hopxly(site1, site2,phi=0.0):
77        return -1
78
79
80  def make_system(a_=1, t_=1):
81
82      lat = kwant.lattice.square(a_)
83      sys = kwant.Builder()
84      #  defide Hall bar dimensions
85      def bar(pos):
86          (x, y) = pos
```

```
 87              if abs(x)>L or abs(y)>W:
 88                  return 0
 89              return 1
 90
 91  #define on site and hopping elements inside Hall bar
 92          sys[lat.shape(bar, (0,0))] = osd
 93          sys[kwant.builder.HoppingKind((1, 0), lat, lat)] = hopx
 94          sys[kwant.builder.HoppingKind((0, 1), lat, lat)] = hopy
 95
 96          #define lead symmetry and geometry
 97          sym_lead = kwant.TranslationalSymmetry(( -a_,0))
 98          sym_lead2 = kwant.TranslationalSymmetry((0,a_))
 99          sym_lead3 = kwant.TranslationalSymmetry((0,a_))
100          lead = kwant.Builder(sym_lead)
101          lead2 = kwant.Builder(sym_lead2)
102          lead3 = kwant.Builder(sym_lead3)
103
104          def lead_shape(pos):
105              (x, y) = pos
106              return (-W   <= y<= W )
107
108          def lead_shape2(pos):
109              (x, y) = pos
110              return (-DC <= x <= -(DC-WC) )
111          def lead_shape3(pos):
112              (x, y) = pos
113              return (DC-WC  <= x <= (DC) )
114
115
116          # define on site and hoppings in the leads
117          lead[lat.shape(lead_shape, (-L, 0))] = 4 * t_
118
119          # current leads
120          lead[kwant.builder.HoppingKind((1, 0), lat, lat)] = hopxlx
121          lead[kwant.builder.HoppingKind((0, 1), lat, lat)] = hopylx
122
123          sys.attach_lead(lead)
124          sys.attach_lead(lead.reversed())
125
126
127          # voltage probes
128          lead2[lat.shape(lead_shape2, (-(DC-WC/2.), W))] = 4 * t_
129          lead2[kwant.builder.HoppingKind((1, 0), lat, lat)] = hopxly
130          lead2[kwant.builder.HoppingKind((0, 1), lat, lat)] = hopyly
131
132          sys.attach_lead(lead2)
133          sys.attach_lead(lead2.reversed())
134
135
136          lead3[lat.shape(lead_shape3, (DC-WC/2., W))] = 4 * t_
137          lead3[kwant.builder.HoppingKind((1, 0), lat, lat)] = hopxly
138          lead3[kwant.builder.HoppingKind((0, 1), lat, lat)] = hopyly
```

```
139
140        sys.attach_lead(lead3)
141        sys.attach_lead(lead3.reversed())
142
143
144        return sys
145
146
147    def main():
148        sys = make_system()
149        #finalize system
150        sys=sys.finalized()
151        #convert magnetic field to magnetic flux
152        phi=B*a*a*e/h
153
154        #enter energy to calculate
155        E=numpy.linspace(EF/t,EF/t,1)
156
157        Resistance1 = []
158        Resistance2 = []
159        Resistance3 = []
160        Resistance4 = []
161        dos=[]
162
163        # iterate over Fermi-energies and magnetic fields
164        for ef in E:
165            for bf in phi:
166                    # construct Landauer Buttiker Matrix with drain
                          contact set to V=0
167                    V=numpy.zeros(shape=(5,5))
168                    smatrix = kwant.smatrix(sys, ef ,args=[bf])
169                    num=numpy.int_([0,2,3,4,5])
170                    for i in numpy.linspace(0,4,5,dtype=int):
171                     for j in numpy.linspace(0,5,6,dtype=int):
172                        if j!=num[i]:
173                          V[i,i]+=smatrix.transmission(num[i],j)*2*e*e/
                              h
174                    for i in numpy.linspace(0,4,5,dtype=int):
175                     for j in numpy.linspace(0,4,5,dtype=int):
176                            if j!=i:
177                              V[i,j]=-smatrix.transmission(num[i],num[j
                                  ])*2*e*e/h
178
179
180        #Calculate potentials
181                K1=numpy.linalg.solve(V,(1,0,0,0,0))
182
183                Resistance1.append(K1[2]-K1[4])
184                Resistance2.append((K1[1]-K1[2]))
185                Resistance3.append(K1[1]-K1[3])
186                Resistance4.append(K1[3]-K1[4])
187
```

```
188                    # save Resistances, Bfields and energy
189                    name="E"+str(nametag)+".txt"
190                    file_E = open(name,'wb')
191                    numpy.savetxt(file_E,E)
192                    file_E.close()
193
194                    name="B"+str(nametag)+".txt"
195                    file_B = open(name, 'wb')
196                    numpy.savetxt(file_B,B)
197                    file_B.close()
198
199                    name="Rxx1"+str(nametag)+".txt"
200                    file_Rxx = open(name, 'wt')
201                    file_Rxx.write(str(Resistance3)[1:-1])
202                    file_Rxx.close()
203                    name="Rxy1"+str(nametag)+".txt"
204                    file_Rxy = open(name,'wt')
205                    file_Rxy.write(str(Resistance2)[1:-1])
206                    file_Rxy.close()
207                    name="Rxx2"+str(nametag)+".txt"
208                    file_Rxx2 = open(name, 'wt')
209                    file_Rxx2.write(str(Resistance1)[1:-1])
210                    file_Rxx2.close()
211                    name="Rxy2"+str(nametag)+".txt"
212                    file_Rxy2 = open(name, 'wt')
213                    file_Rxy2.write(str(Resistance4)[1:-1])
214                    file_Rxy2.close()
215
216                    # calculate ldos, sum to dos and save
217                    ldos=kwant.ldos(sys, ef,args=[bf])
218                    dos.append(numpy.sum(ldos))
219                    name="DOS"+str(nametag)+".txt"
220                    file_dos = open(name,'wt')
221                    file_dos.write(str(dos)[1:-1])
222                    file_dos.close()
223
224  main()
```

Danksagung

Zum Gelingen dieser Arbeit haben viele Personen beigetragen und es ist mir eine Freude, ihnen hier zu danken.

Zunächst sei mein Doktorvater Prof. Thomas Heinzel genannt. Danke, dass du mich bei diesen interessanten und vielfältigen Projekten betreut hast. Du warst stets unterstützend und offen für Diskussionen über das weitere Vorgehen. Auch meinen Wunsch nach einem Forschungsaufenthalt in Japan hast du mitgetragen und mich auf das March Meeting in die USA geschickt, wodurch ich meinen Horizont beträchtlich weiten konnte.

Ich danke Prof Jürgen Horbach für die Übernahme des Korreferats.

Dank sei Jürgen Horbach und Nima Siboni weiterhin ausgesprochen für die erfolgreiche und angenehme Kollaboration im Rahmen des Lorentzgasprojekts.

Klaus Pierz und Hans Werner Schumacher von der PTB Braunschweig haben uns alle in dieser Arbeit verwendeten hochbeweglichen Heterostrukturen zur Verfügung gestellt, wofür ich ihnen danken möchte. Bei Sibylle Sievers bedanke ich mich für die Durchfürhung der SQUID Magnetometrie.

Dimitris Kazazis, Ulf Gennser and Dominique Mailly undertook the electron beam lithography and the reactive ion etching at C2N-CNRS in Marcoussis. Thank you for the efficient and pleasant collaboration.

It was a pleasure to discuss quantum transport in antidot lattices with Juraj Feilhauer.

A special shout-out is given to the Kwant team. Thank you for sharing your work with the community.

I am deeply grateful to Prof. Shingo Katsumoto and his group at the University of Tokyo. It was a truly marvelous experience to receive their hospitality. In particular, I would like to thank Yu Iwasaki, Taketomo Nakamura and Akira Endo, who helped me a lot in the lab, but also integrated me to the group. I am happy to thank Junko Kawamura, who helped me get around the obstacles a non-Japanese speaker like me can experience in everyday life. It was also very kind of her to take me along to the tea ceremony club. I gratefully acknowledge the funding for this research stay by JSPS within the framework of the Summer Program.

Diese Arbeit hat durch viele Verbesserungsvorschläge von Svenja, Laurin und Stefan bezüglich des Inhalts, der Sprache und der Gestaltung profitiert. Danke für eure Mühen.

Die Atmosphäre am Lehrstuhl für Festkörperphysik war von Anfang an von großer Hilfsbereitschaft geprägt. Ich danke allen meinen Kolleginnen und Kollegen, mit denen ich die letzten Jahre zusammen arbeiten durfte. Zunächst sei Bernd Schüler genannt, mit dem ich nicht nur lange Jahre ein Büro geteilt habe, sondern der mich

Eidesstattliche Versicherung

Ich versichere an Eides Statt, dass die Dissertation von mir selbständig und ohne unzulässige fremde Hilfe unter Beachtung der „Grundsätze zur Sicherung guter wissenschaftlicher Praxis an der Heinrich-Heine-Universität Düsseldorf" erstellt worden ist.

_____

Düsseldorf, den 02. März 2018